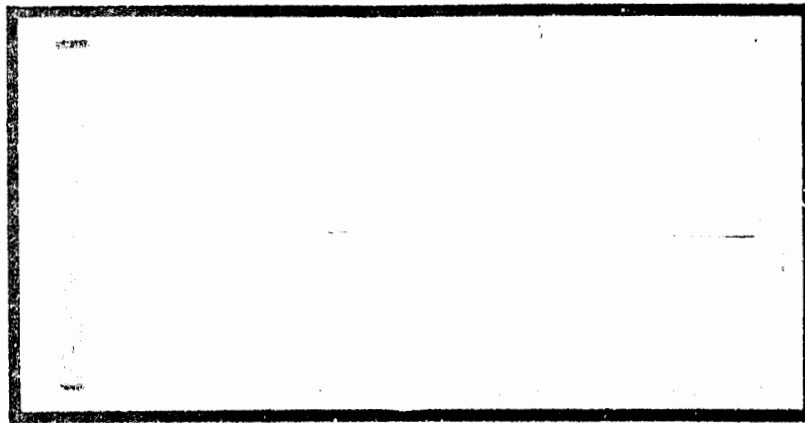


ADA080412



10

10/11/77



DDC  
 RECORDED  
 FEB 1980  
 A

DDG FILE COPY

UNITED STATES AIR FORCE  
 AIR UNIVERSITY  
 AIR FORCE INSTITUTE OF TECHNOLOGY  
 Wright-Patterson Air Force Base, Ohio

PII Redacted

DISTRIBUTION STATEMENT A  
 Approved for public release  
 Distribution Unlimited

80 2 5 50

14

AFIT/GE/EE/79D-25

6

PROPERTIES OF ION-IMPLANTED  
AND DIFFUSED PHOTODETECTORS OF  
GERMANIUM AND GERMANIUM-SILICON ALLOYS.

Master's THESIS

AFIT/GE/EE/79D-25

Irene M. N. Mills  
2d Lt USAF

10

Irene Marie Nadeau Mills

11

Dec 79

12

170

Approved for public release; distribution unlimited

✓ 012 225

AB



## Preface

Wafers of Ge-Si (90%-10%) were expected to have been available at RADC/ESO at Hanscom AFB for the fabrication of photodetectors during the summer of 1979. Since this did not come to pass, the work of this thesis focussed on the fabrication of Ge photodiodes making use of shallow junctions to increase the amount of photogenerated carriers collected by the p-n junction. This thesis describes the fabrication and testing of ion-implanted and diffused Ge photodiodes. It also includes a quantum mechanical analysis of the energy band structure of the proposed Ge-Si alloy to predict the behavior of holes and electrons in the crystal lattice.

Thanks are due to Andrew Yang for permission to do the thesis work at RADC/ESO. Special thanks go to D. Eirug Davies, Joseph P. Lorenzo, and Thomas J. Ryan for their major involvement in the project and the education of the author! Associated personnel were also very helpful during the fabrication, packaging, and testing procedures of each sample. I am very grateful for the assistance and direction provided by John M. Borke in the role of thesis advisor. I am forever indebted to my roommate and friend, Marla K. Doxey, for her typing skills. To my husband, Orrin, I dedicate my thesis in return for his support and faith in me during this experience.

Irene M. Nadeau Mills

## Contents

	Page
Preface . . . . .	ii
List of Figures . . . . .	v
List of Tables. . . . .	viii
Notation. . . . .	ix
Abstract. . . . .	xiii
I. Introduction . . . . .	1
Background . . . . .	1
Status of Germanium Diodes . . . . .	3
Problem and Scope. . . . .	6
General Approach . . . . .	7
Sequence of Presentation . . . . .	9
II. Background . . . . .	10
Introduction . . . . .	10
The Photoelectric Effect . . . . .	10
Shallow Junctions. . . . .	13
Photodetector Losses . . . . .	18
Device Characteristics . . . . .	19
Photoresponse. . . . .	19
Quantum Efficiency . . . . .	22
Diode Characteristics. . . . .	23
Dark Current . . . . .	27
Carrier Lifetimes. . . . .	28
Applied Bias . . . . .	28
Fabrication of Shallow Junctions . . . . .	28
III. Ge-Si Alloy Theory . . . . .	33
The One-Electron Model . . . . .	34
The Free-Electron Approximation. . . . .	41
The Tight-Binding Approximation. . . . .	45
Orthogonalized Plane Waves (OPW) . . . . .	52
The Pseudopotential Method . . . . .	54
The Cellular Method. . . . .	57
Effective Mass Approach. . . . .	57
Augmented Plane Waves. . . . .	58

Ge-Si Alloy Considerations . . . . .	58
The Tight-Binding (LCAO) Approach to the Ge-Si Alloy . . .	59
General Approach of the LCAO Method for Solids . . . . .	59
Applying the LCAO Method to the Diamond Structure. . . . .	68
Suggestions for Applying the LCAO Method to the Ge-Si Alloy	70
IV. Device Fabrication and Testing . . . . .	75
V. Experimental Procedure and Equipment . . . . .	83
Photometric System . . . . .	83
Weak Signals Buried in Noise . . . . .	83
Equipment. . . . .	83
VI. Results. . . . .	92
VII. Analysis of Results. . . . .	95
VIII. Conclusions and Recommendations. . . . .	113
Bibliography. . . . .	115
Appendix A: Synchronous Detection. . . . .	120
Appendix B: Experimental Procedure . . . . .	122
Appendix C: I-V Points Used to Plot the Diode Characteristics of Each Sample . . . . .	129
Appendix D: Output Voltages Recorded Across the 100K Resistor for Each Test Run. . . . .	134
Appendix E: Photocurrent, Incident Optical Power, Responsivity, and Quantum Efficiency of Each Sample Per Test Run . .	139

List of Figures

<u>Figures</u>	<u>Page</u>
1 Spectral attenuation curve of optical fiber. . . . .	2
2 The spectral response curves of Si and Ge photodiodes. . .	4
3 The Ge-Si system . . . . .	5
4 Absorption coefficient versus wavelength for Ge and Si . .	14
5 Exponential decay of light as it is absorbed into a material . . . . .	15
6 Depletion-layer width as a function of substrate doping and applied reverse bias. . . . .	17
7 The p-n junction under reverse bias showing depletion layer widening and losses incurred by incident radiation .	20
8 The energy band diagram of a p-n junction under reverse bias . . . . .	21
9 Ideal current-voltage characteristics of a diode . . . . .	23
10 Making contact to the photodiode . . . . .	31
11 A representation of the potential in a perfectly periodic crystal lattice . . . . .	37
12 The ideal periodic square-well potential used by Kronig and Penney to show the general characteristics of the quantum behavior of electrons in periodic lattices . . . .	37
13 The energy $\epsilon$ plotted as a function of $k$ . . . . .	38
14 The reduced-zone representation of the $\epsilon$ - $k$ plot . . . . .	40
15 Schematic representation of the $\epsilon$ versus $k$ relation for the free electron approximation. . . . .	44
16 The $\vec{r}$ and $\vec{r}_n$ vectors used in the calculation of the tight-binding approximation. . . . .	47
17 The potential function used in the tight-binding approximation. . . . .	49

18	The discrete levels of atomic energy split into bands as the isolated atoms are assembled into a crystal lattice. . . . .	49
19	The energy band structures of Si and Ge. . . . .	55
20	The energy band structures for Ge and Si using the method of pseudopotentials . . . . .	57
21	The diamond lattice. . . . .	69
22	a) The energy bands of a diamond crystal in the 100 and 111 directions b) the energy band structure of a Ge crystal c) the energy bands of Ge along the 100 and 111 axes. . .	71
23	The energy bands of Si along the 100 and 111 directions. .	72
24	Implant holder and mask used for processing four chips of four diodes each. . . . .	78
25	The 3-mil lift-off process . . . . .	78
26	Mesa etching using dots of black wax over the diode area .	79
27	The diodes are tested using probes which lead to a conventional curve tracer. . . . .	80
28	Diagram showing pin connections for a 4-diode chip . . . .	80
29	Typical diode structure showing center contact, bonding wire, and perimeter of the diode with measuring scale. . . . .	82
30	The block diagram of a photometric system. . . . .	84
31	Schematic optical path of a monochromator. . . . .	86
32	The experimental set-up for the photometric system . . . .	87
33	Laboratory set-up for mounting a sample for testing. . . .	88
34	Panel of instruments used in processing and recording the output of the photodetector. . . . .	89
35	I-V characteristics of G-7-1 #9. . . . .	98
36	I-V characteristics of G-7-4 #23 . . . . .	99
37	I-V characteristics of G-8-1 #23 . . . . .	100
38	I-V characteristics of D-6-1 #6. . . . .	101

39	I-V characteristics of D-6-3 #6 . . . . .	102
40	Photoresponse and quantum efficiency curves of G-7-1 #9 .	103+
41	Photoresponse and quantum efficiency curves of G-7-4 #9 .	105+
42	Photoresponse and quantum efficiency curves of G-8-1 #23.	107+
43	Photoresponse and quantum efficiency curves of D-6-1 #6 .	109+
44	Photoresponse and quantum efficiency curves of D-6-3 #6 .	111+
45	Application and operation of the lock-in-amplifier in a synchronous detection scheme . . . . .	121
46	Mounting the sample on the vacuum header. . . . .	123
47	Pulling the leads through the back of the vacuum chamber.	123
48	Photo showing the leads from the diode being inserted into a 5-pin socket of the connector with coaxial output pins.	124
49	Adjusting trim to obtain display of full-rectified wave .	127
50	The rotating drum and remote switch used to scan the spectral output of the globar and trigger the data recorder. . . . .	127

List of Tables

<u>Table</u>		<u>Page</u>
I	Summary of Recent Ge Photodiodes . . . . .	8
II	Energy Integrals for a Crystal in Terms of Two-Center Integrals . . . . .	67
III	Device Fabrication. . . . .	76
IV	Calibration Data . . . . .	85
V	List of Equipment Used in the Photometric System . . . . .	91
VI	Diameters of Diodes and Contacts Used to Determine Active Area. . . . .	93

### Notation

- a = lattice constant
- B = noise equivalent bandwidth, Hz
- c = velocity of light,  $3 \times 10^8$  m/s
- $C_n$  = Fourier expansion coefficients of  $f(x)$
- $C_s$  = impurity concentration at the surface,  $\text{cm}^{-3}$
- $C(x,t)$  = impurity concentration as a function of time and distance from the surface,  $\text{cm}^{-3}$
- $D_{n,p}$  = diffusion coefficient for electrons and holes respectively,  $\text{cm}^2/\text{sec}$
- E = energy, eV
- $E_g$  = energy gap, eV
- $f(x)$  = periodic function of the lattice
- h = Planck's constant,  $6.625 \times 10^{-34}$  joule-sec
- $\hbar$  =  $h/2\pi$
- H = optical power, W
- $H'$  = incident optical power after reflection, W
- H = Hamiltonian operator
- $H_L$  = optical power incident on the surface, W
- I = current, A
- I = light intensity
- $I_o$  = total incident light intensity
- $I_d$  = noise current, A
- $I_{\text{noise}}$  = noise current, A
- $J_{\text{diff}}$  = diffusion current density

$J_{dr}$  = drift current density,  $A/cm^2$   
 $J_s$  = saturation current density,  $A/cm^2$   
 $J_{tot}$  = total current density through a depletion region under reverse bias,  $A/cm^2$   
 $k$  = propagation constant  
 $\vec{k}$  = propagation vector  
 $k_o$  = constant related to  $\epsilon$   
 $L_{p,n}$  = diffusion length of holes and electrons, respectively,  $\mu m$   
 $m$  = free mass of an electron  
 $m^*$  = effective mass of an electron  
 $n$  = density of electrons  $cm^{-3}$   
 $\bar{n}$  = index of refraction  
 $N$  = number of atoms in the crystal  
 $n_i$  = intrinsic carrier concentration,  $cm^{-3}$   
 $n_p$  = minority carrier density (electrons),  $cm^{-3}$   
 $n_{po}$  = density of electrons at equilibrium,  $cm^{-3}$   
 $N_A$  = concentration of acceptors,  $cm^{-3}$   
 $N_B$  = background concentration,  $cm^{-3}$   
 $p$  = density of holes,  $cm^{-3}$   
 $q$  = charge of a carrier,  $1.602 \times 10^{-19}$  coul  
 $\vec{r}$  = vector position of an atom  
 $R$  = responsivity,  $A/W$   
 $\mathcal{R}$  = reflection coefficient  
 $R_s$  = sheet resistance,  $\Omega/\square$   
 $t$  = time, sec  
 $T$  = temperature,  $^{\circ}K$

$u(x)$  = Bloch function  
 $U(x)$  = potential energy of the crystal lattice, eV  
 $v$  = volume  
 $V_B$  = breakdown voltage  
 $V_{bi}$  = built-in potential, volts  
 $V_{bias}$  = applied bias voltage, volts  
 $V_n$  = Fourier expansion coefficients of  $V(x)$   
 $V(x)$  = potential function, eV  
 $W$  = depletion width,  $\mu\text{m}$   
 $x$  = distance, cm  
 $\alpha$  = absorption coefficient,  $\alpha(\lambda)\text{cm}^{-1}$   
 $\gamma$  = scalar  
 $\epsilon$  = energy, eV  
 $\Delta\epsilon$  = width of forbidden energy region, eV  
 $\epsilon_n$  = energy of a free particle at the band edge, eV  
 $\epsilon_0$  = ground state of an electron, eV  
 $\epsilon_s$  = semiconductor permittivity, farad/cm  
 $\eta$  = quantum efficiency, electrons per photon  
 $\lambda$  = wavelength,  $\mu\text{m}$   
 $\mu_{n,p}$  = mobility of electrons or holes,  $\text{cm}^2/\text{V-sec}$   
 $\sigma$  = conductivity,  $1/\Omega$   
 $\tau_n$  = lifetime of excess carriers, sec  
 $\tau_p$  = lifetime of holes, sec  
 $\phi$  = phase difference between neighboring atoms  
 $\phi(\bar{r})$  = atomic orbital  
 $\nu$  = frequency, Hz

$\psi$  = wavefunction independent of time

$\psi_0$  = wavefunction associated with  $\epsilon_0$

$\Psi$  = wavefunction as a function of position and time

Abstract

MICRO

The response of planar shallow-junction Ge photodiodes displayed peak performance at the expected 1.46  $\mu\text{m}$  wavelength. Responsivity and quantum efficiency were measured at  $\sim 0.9 \mu\text{A}/\mu\text{W}$  and  $\sim 80\%$ , respectively, with leakage currents of  $\sim 6 \mu\text{A}$ , typical for Ge photodiodes. Leakage currents were notably decreased in diffused diodes. The high values for responsivity and quantum efficiency could be attributed to the shallow junction ( $\sim 1 \mu\text{m}$ ) designed to increase the amount of photogenerated current which could be collected by the p-n junction. The reason for the interest in photodetectors lies in fiber-optic applications. Minimum fiber attenuation and dispersion occurs near 1.27  $\mu\text{m}$ . Photodetectors at this wavelength require tailoring of the bandgap energy of Ge by adding about 10% Si. A quantum mechanical analysis of the energy band structure of the Ge-Si alloy is included with suggestions to obtain energy gap and effective mass values experimentally. Ge-Si photodetectors fabricated as shallow-junction photodiodes should exhibit high photoresponse and quantum efficiency near 1.27  $\mu\text{m}$ .

PROPERTIES OF ION-IMPLANTED  
AND DIFFUSED PHOTODETECTORS OF  
GERMANIUM AND GERMANIUM-SILICON ALLOYS

THESIS

I Introduction

Background

Within the last decade, communication using light signals transmitted over optical fibers has become a feasible alternative to the transmission of electrical signals over wire. Optical fiber systems are attractive for Air Force applications because of their advantages over present systems: elimination of crosstalk, reduced size and weight, lower cost, low losses and high bandwidths, plus freedom from ground loop pickups and electromagnetic interference (EMI) (Ref 38:5-6,10). The development of light sources, particularly for use in fiber communication systems, has spurred the development of photodetectors. The light sources employing III-V semiconductor materials include ternary and quaternary alloys whose variable composition makes it possible to fabricate sources for a wide span of wavelengths (Ref 12:110). Light sources, such as lasers and light-emitting diodes, convert electrical signals into optical radiation in wavelengths that range from the far infrared (1-100  $\mu\text{m}$ ) region through the visible (0.45-0.70  $\mu\text{m}$ ) and the ultraviolet (0.01-0.1  $\mu\text{m}$ ) regions. The optical radiation transmitted through an optical fiber is converted back to electrical signals for signal processing in the receiver by a photodetector.

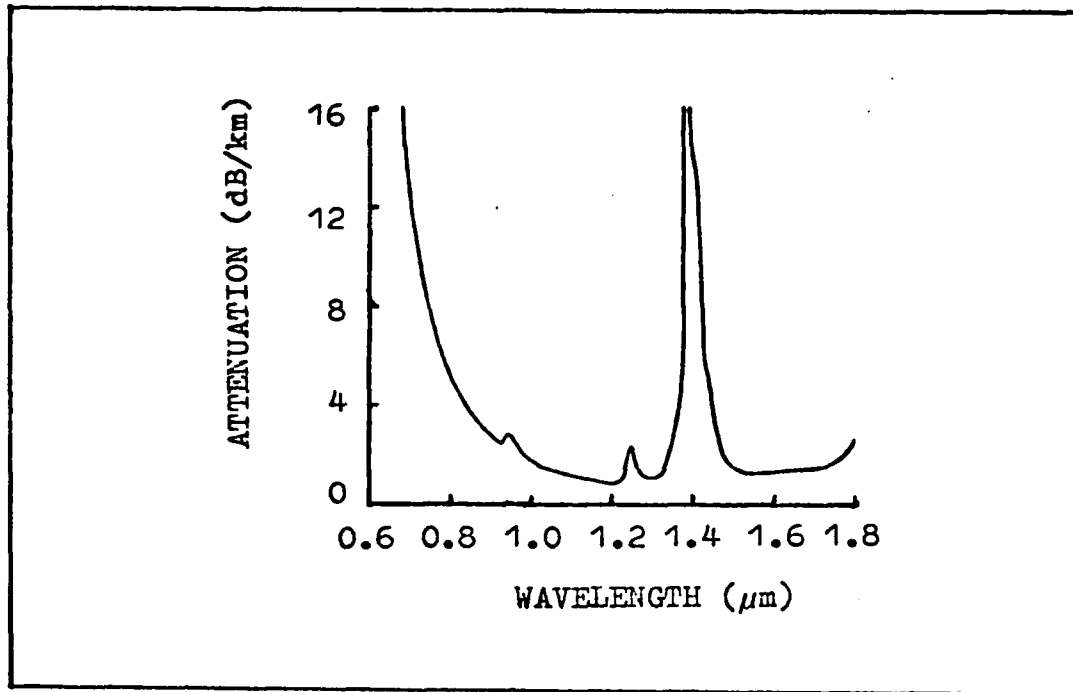


Fig 1. Spectral attenuation curve of optical fiber with 8%  $\text{GeO}_2$  - 0.7%  $\text{P}_2\text{O}_5$  doped  $\text{SiO}_2$  core(Ref 58).

In looking at desirable optimization of the source-channel-detector system (Ref 3; 28; 56), certain fiber characteristics dictate preferred wavelengths of operation, that is, the wavelengths at which transmission through the fiber channel will result in minimum losses. Refer to the spectral attenuation curve of a typical fiber in Figure 1. In considering three wavelengths of operation:  $\sim 0.85 \mu\text{m}$ ,  $\sim 1.0 \mu\text{m}$ , and  $\sim 1.27 \mu\text{m}$ , some interesting points have been observed (Ref 12). At approximately  $0.85 \mu\text{m}$ , the popular wavelength at present, GaAlAs sources are well matched to Si detectors. At  $\sim 1.0 \mu\text{m}$ , silicon detectors experience a drop in quantum efficiency when matched to GaInAsP LED's, injection lasers, and Nd:YAG crystals; they also require a large applied bias sufficient to obtain the needed 100-200  $\mu\text{m}$  depletion layer width, increasing the leakage

current, and hence noise. The interest in the 1.0  $\mu\text{m}$  wavelength is due to reduced fiber attenuation and dispersion, that is, improved fiber characteristics that help compensate for the shortcomings of the Si detector at 1.0  $\mu\text{m}$ . Absorptionless transmission is possible and material dispersion in the fiber is minimized for wavelengths near 1.27  $\mu\text{m}$  (Ref 12; 58). However, because silicon detectors are not sufficiently sensitive at 1.2-1.3  $\mu\text{m}$ , interest has shifted to other III-V compounds to fabricate detectors which have greater quantum efficiency. In the near 1.3  $\mu\text{m}$  range, III-V compound sources are presently available. Good detectors for operation at 1.27  $\mu\text{m}$  are the next hurdle. It is well known that the wavelength at which a semiconductor material will detect is a function of its energy gap. This implies that a semiconductor crystal must be grown whose energy gap brings about photosensitivity at a wavelength of  $\sim 1.27 \mu\text{m}$ .

#### Status of Germanium Diodes

Germanium has the ideal bandgap (0.67 eV) for detecting wavelengths in the range of 1.4-1.6  $\mu\text{m}$  as shown in the spectral response curves of Si and Ge in Figure 2 (Ref 34). It does detect wavelengths between 1.2-1.3  $\mu\text{m}$  but an energy gap of about 0.95 eV would be ideal here. One possible approach is the use of III-V compound alloys to "tailor" the energy gap. The Ge-Si system shown in Figure 3 suggests that the energy gap of Ge can be tailored by combination with Si to meet the requirements of detection at  $\sim 1.27 \mu\text{m}$ . It is proposed that a Ge-Si alloy would produce the correct bandgap for detecting wavelengths which the fiber transmits best. Energy bandgap is drawn as a function of the percentage of Si in

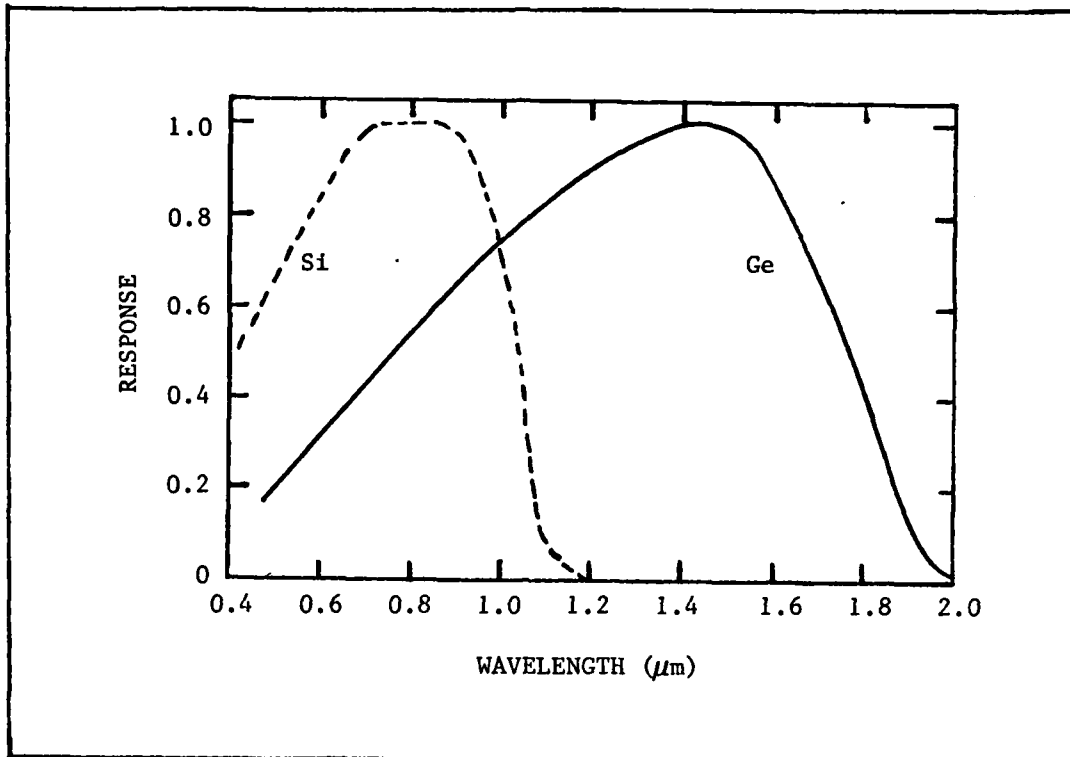


Fig 2. The spectral response Curves of Si and Ge photodiodes (Ref 34).

Ge and is scaled on the left; the lattice constant scale is on the right. The graph shows that the bandgap does not increase linearly as the percentage of Si in Ge increases. In fact, the function has a break in it showing a steep slope when 0-15% Si is added to Ge and a less steep slope elsewhere. The steeper slope implies that a larger variation in bandgap is possible with a small amount of Si in Ge. However, it should be stated that the mismatch in the lattice constants of Ge and ~10% Si begins to cause a breakdown in the crystal lattice. But according to the curve, a 10% Si - 90% Ge alloy suggests a bandgap of ~0.85 eV, based on the relationship between energy gap and wavelength of detection, which approaches the desired bandgap for detection at a wavelength near 1.27 μm.

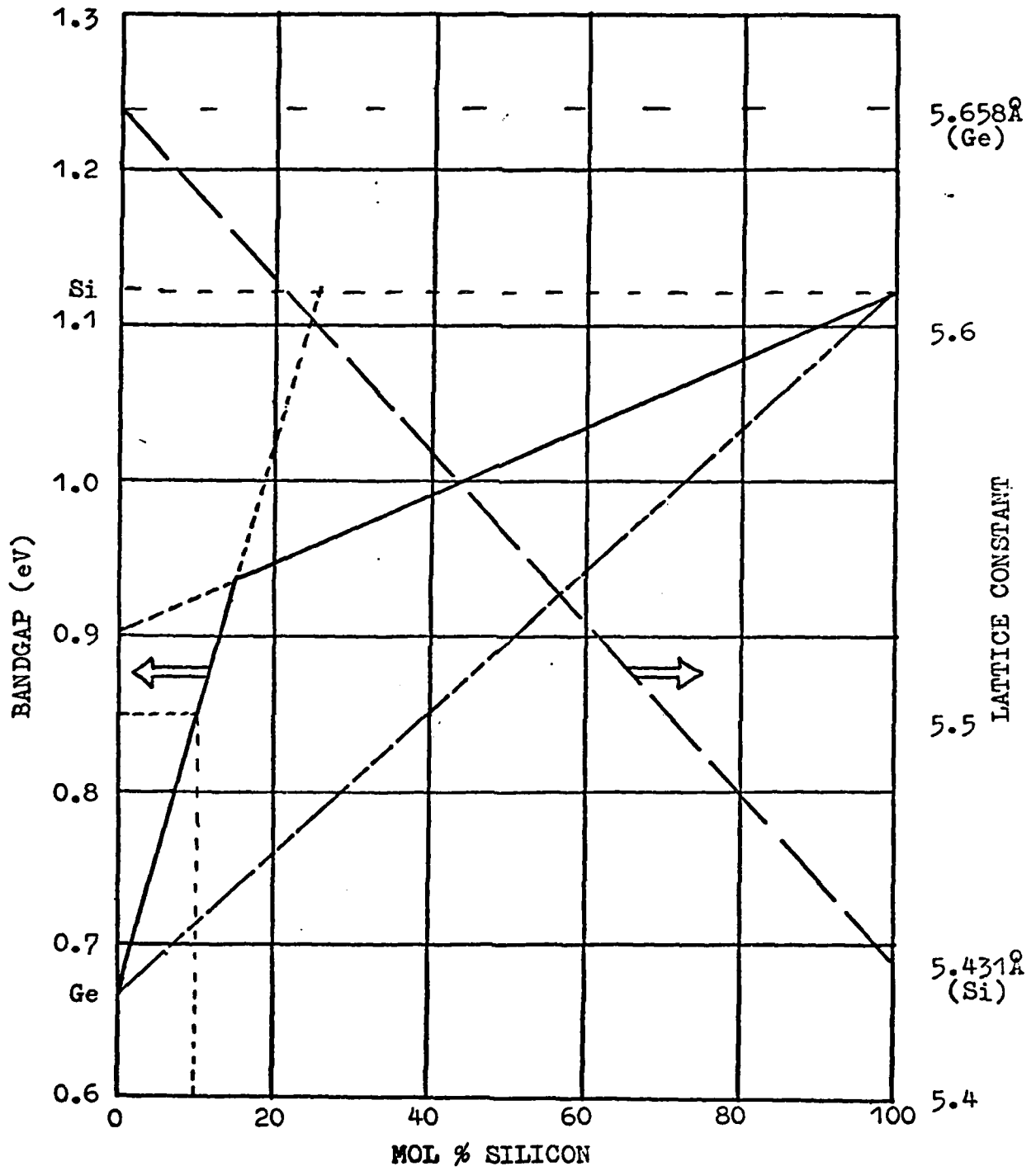


Fig 3. The Ge-Si system (Ref 5; 27).

## Problem and Scope

One of the major problems in the proposal to fabricate semiconductor photodetectors from a Ge-Si crystal alloy is the growth of the crystal alloy itself. The change in interest from Ge to Si in the early days of semiconductor technology has almost made Ge a forgotten material. Much of the research and study of Ge and Ge-Si alloys was dropped when the convenience and versatility of the Si-SiO<sub>2</sub> system was realized. It is necessary to study the early literature on Ge, especially Ge-Si alloys, and attempt to grow the alloy using the modern and well defined techniques for growing crystals. In the meantime, while progress is being made by crystallographers, the problem of fabricating devices from Ge-Si can be addressed.

The first step toward fabricating devices from the alloy is to work with the basic substrate material, ie. Ge. That is the main subject of this thesis. In other words, since the crystal alloy of interest is primarily Ge, an indication of the behavior of devices made in Ge-Si can be obtained from those made in pure Ge. The work involved in this thesis is limited to Ge photodiodes with very shallow junctions. The goal is to make very shallow junction Ge photodiodes by well known fabrication techniques such as diffusion and ion implantation which are comparable in performance to Si photodiodes, each in its own preferred wavelength range of operation. A more immediate goal is to verify the performance of the Ge photodiodes with known results such as peak photoresponse at  $\sim 1.46 \mu\text{m}$  expected of Ge and responsivities comparable to other Ge photodiode structures. Once techniques are developed for making Ge photodiodes which work reasonably well, the next step will be to tailor the bandgap of the Ge substrate material with Si, thereby changing the wavelength of operation.

## General Approach

In the interest of obtaining photodetector performance at  $1.27 \mu\text{m}$ , the approach of concern in this thesis begins with Ge photodiodes whose peak response occurs at  $\sim 1.46 \mu\text{m}$ . The Ge diodes which are fabricated must have increased quantum efficiency and decreased leakage currents from the large values which have been characteristic of Ge devices. The distinguishing feature between other Ge photodiodes and those pursued in this work is the shallow junction,  $\sim 0.25\text{--}0.75 \mu\text{m}$  deep, discussed further in Section II. The goal of diffused diodes is uniform doping across the active area of the diode. The diffused diodes are mesa etched to reduce the surface leakage currents and define the active area of the diode. The ion implanted diodes promise better control for obtaining shallow junction depths and doping concentrations. Implanted diodes discussed in this thesis have been thermally annealed, although there is interest in laser and electron beam annealing.

Each completed sample photodiode was tested in two areas of performance. First, each sample was tested as a diode to verify expected diode action and for low leakage currents. Second, each diode is tested for its optical properties. The photoresponse characteristics determine the wavelength of peak response and the quantum efficiency of the photodiodes which can be compared to previously reported Ge photodiode photoresponse characteristics as listed in Table I.

Work done in parallel with the fabrication of Ge photodiodes includes the crystal growth of the Ge-Si alloy that will supply the material needed for devices optimized for a wavelength of operation of  $1.27 \mu\text{m}$ . The first step is to be able to grow an epitaxial layer of Ge on top of a

TABLE I  
Summary of Recent Ge Photodiodes

Reference	p-Ge	Guard Ring	Diffusion	Passivation /AR Coating	Active Diameter	Leakage Current	Bias Voltage	Quantum Efficiency
Ando, <u>et al.</u> (1978) Planar APD (Ref 2)	Ga-doped 0.3-0.5 $\Omega$ -cm	n-Sb diffusion x=7.5 $\mu$ m	n <sup>+</sup> -As x=0.4 $\mu$ m 1.0 $\mu$ m 1.6 $\mu$ m	SiO <sub>2</sub>	0.1mm	0.1-0.3 $\mu$ A at 0.9 V <sub>B</sub> V <sub>B</sub> =23-33V T <sub>p</sub> =9x10 <sup>-10</sup> sec	1V	For 0.4 $\mu$ m: 42% at 0.81 $\mu$ m 73% at 1.15 $\mu$ m 74% at 1/32 $\mu$ m
Conradi (1975) Planar P-I-N (Ref 11)	high purity <sup>11</sup> / 1-2x10 <sup>12</sup> /cc after processing due to Cu, Au	present but not specified	n-P doped oxide source x=5-10 m AR film R <sub>s</sub> =10-15 $\Omega$ /□	oxide/ Si <sub>3</sub> N <sub>4</sub> double layer	1-5mm	2.5mA/cm <sup>2</sup>	5-10V	70% at peak
Math Assoc. (1977) (Ref 34)					1mm	6 $\mu$ A at 10 V	up to 15 V	at -10 V 74% at 1.15 $\mu$ m R=0.7 $\mu$ A/ $\mu$ W at 1.15 $\mu$ m =0.81 $\mu$ A/ $\mu$ W at 1.4 $\mu$ m
Shibata, <u>et al.</u> (1970) Planar APD (Ref 51)	0.3 $\Omega$ -cm	n-Sb diffusion x=5-10 $\mu$ m	n <sup>+</sup> -As x<1 $\mu$ m	SiO <sub>2</sub> by CVD	2.4 mil	0.2 $\mu$ A V <sub>B</sub> =25V		23/5% at 6328 Å 40% at 1.06 $\mu$ m
Takanashi, <u>et al.</u> (1970) Planar APD (Ref 54)	Ga-doped 1x10 <sup>16</sup> /cc	n-Sb diffusion x=0.7 $\mu$ m	n-As 10 <sup>20-3</sup> cm <sup>-3</sup>	SiO <sub>2</sub> by CVD	2x10 <sup>-5</sup> cm <sup>2</sup> area			40% at 1.06 $\mu$ m 15% at 6328 Å

known Ge sample. The ratio of Si to Ge is then increased slowly to encourage formation of single crystal Ge-Si alloy. Once such an alloy exists, fabrication of the alloy photodiodes using the techniques developed for pure Ge substrate photodiodes can be attempted.

#### Sequence of Presentation

With the forgoing discussion as an explanation of the interest in Ge and Ge-Si photodiodes, Chapter II provides a background to the general area of photodiodes and how they operate. The discussion includes simple photodetector theory to provide motivation for shallow junctions. This is followed by a discussion of the diode characteristics that result from the fabrication techniques used to form these shallow junctions. Chapter III gives the theoretical background for tailoring the bandgap of semiconductor materials and the effects of this tailoring on wavelength of response, specifically of the Ge-Si system to obtain peak response at  $1.27 \mu\text{m}$ . Chapter IV provides a history of the fabrication of each sample tested and Chapter V outlines the experimental procedure and equipment used.

The data reduction procedure and results are given in Chapter VI. Limits of the validity of the data are also discussed here. An analysis of the results is given in Chapter VII. It covers photoresponse and diode characteristics of the implanted and diffused diodes. Conclusions and recommendations are presented in Chapter VIII.

## II Background

### Introduction

Coherent and incoherent light sources such as lasers and LED's produce wavelengths of optical radiation that extend from the far infrared region through the visible to the ultraviolet region. For this reason, photodetectors are being developed with high sensitivity to weak light signals and response to light intensity modulation at frequencies extending into the microwave region (Ref 36; 37). The development of various light sources has subsequently spurred the development of photodetectors. It is possible to design optical detectors and optical receivers for performance at various wavelengths of light and combinations of speed of response.

An understanding of the photoelectric effect provides insight into how photodetectors operate at certain wavelengths. The speed of response of photodetectors, i.e. the bandwidth of modulating signals which can be processed, depends on other processes associated with semiconductor devices.

### The Photoelectric Effect

The generation of carriers in a semiconductor by incident light is based on the photoelectric effect (Ref 15:31-38). According to this phenomenon, a photon with energy

$$E = h\nu \quad (1)$$

where

$E$  = energy, eV

$h$  = Planck's constant  $6.625 \times 10^{-34}$  joule-sec

$\nu$  = frequency, Hz

which is inherent in the light incident on the photodetector is absorbed by the semiconductor material and forces the transition of a carrier from a quantum state of low mobility to a quantum state of high mobility. The conductivity of a material is a function of carrier mobility and the number of carriers as expressed by

$$\sigma = q (\mu_n n + \mu_p p) \quad (2)$$

where

$\sigma$  = conductivity,  $1/\Omega$ .

$q$  = charge of the carrier,  $1.602 \times 10^{-19}$  coul

$\mu_n$  = mobility of electrons,  $\text{cm}^2/\text{V-sec}$

$n$  = density of electrons,  $\text{cm}^{-3}$

$\mu_p$  = mobility of holes,  $\text{cm}^2/\text{V-sec}$

$p$  = density of holes,  $\text{cm}^{-3}$ .

When incident light falls on the surface of the photodetector, carriers are generated either by intrinsic or extrinsic transitions (Ref 53:628-629). In the case of intrinsic transitions, the increase in conductivity under illumination is due to the increase in the number of carriers.

The wavelength at which detection occurs is derived from the photon energy and the energy bandgap of the semiconductor material. When the amount of photon energy is just sufficient to cause the transition of a carrier from its bound state in the lattice to a free state, that photon energy is equal to the energy bandgap of the material.

Wavelength is related to frequency through the velocity of light,  
 $c = \lambda \nu$  . Substituting for  $\nu$  into Equation (1):

$$E_g = h\nu = \frac{hc}{\lambda} \quad (3)$$

or

$$\lambda = \frac{hc}{E_g} = \frac{1.24}{E_g \text{ (eV)}} \mu\text{m} \quad (4)$$

where

$\lambda$  = wavelength,  $\mu\text{m}$

$h$  = Planck's constant

$c$  = velocity of light,  $3 \times 10^8$  m/s

$E_g$  = energy bandgap, eV.

The important result of this simple substitution is that the wavelength which a semiconductor material detects is related to the energy gap,  $E_g$ , of that semiconductor material. Therefore, to detect optical radiation at a particular wavelength or range of wavelengths, one must consider the material the photodetector is made of.

It is also possible to have energy states within the forbidden energy gap and for transitions to occur between these states and the higher mobility conduction states. This process is known as extrinsic photoexcitation. By means of doping with impurities whose allowed energy states fall in the forbidden energy gap of the parent material, the device can be made to detect optical wavelengths longer than those predicted by Equation (4). Conductivity, as a result of photoexcitation, takes place through the absorption of photons of energy greater than or equal to the energy separation of the conduction and valence band levels.

### Shallow Junctions

The current that can be generated in a photodiode is dependent on the amount of light absorbed by the material. The absorption coefficient,  $\alpha$  ( $\text{cm}^{-1}$ ), is also a strong function of wavelength and semiconductor material as shown in Figure 4 for Si and Ge at  $300^\circ\text{K}$  (Ref 14:1151; 53:661). Germanium can absorb light in a range of wavelengths between 0.65 and  $1.62 \mu\text{m}$ . The absorption coefficient and wavelength are factors that determine the intensity of light as it penetrates the semiconductor, according to the relationship

$$I = I_0 \exp(-\alpha x) \quad (5)$$

where

$I$  = light intensity at a depth,  $x$ , into the semiconductor from the surface

$I_0$  = total incident intensity

$\alpha$  = absorption coefficient,  $\alpha(\lambda) \text{ cm}^{-1}$

$x$  = distance, cm.

The intensity falls off exponentially with distance into the material. A plot of intensity versus distance is shown in Figure 5 for wavelengths 0.65, 1.0, 1.27, and  $1.5 \mu\text{m}$ , at each of which there exists some interest for optical fiber systems. The absorption coefficients for these wavelengths are  $10^5$ ,  $6.6 \times 10^4$ ,  $8.0 \times 10^3$ , and  $5.0 \times 10^3 \text{ cm}^{-1}$ , respectively, as obtained from Figure 4. Certain deductions can be made by observing the curves in Figure 5. A discussion of this follows.

It is possible to determine the depth and width of the depletion region needed for absorption of specific wavelengths. Only carriers generated within the depletion region and within one diffusion length

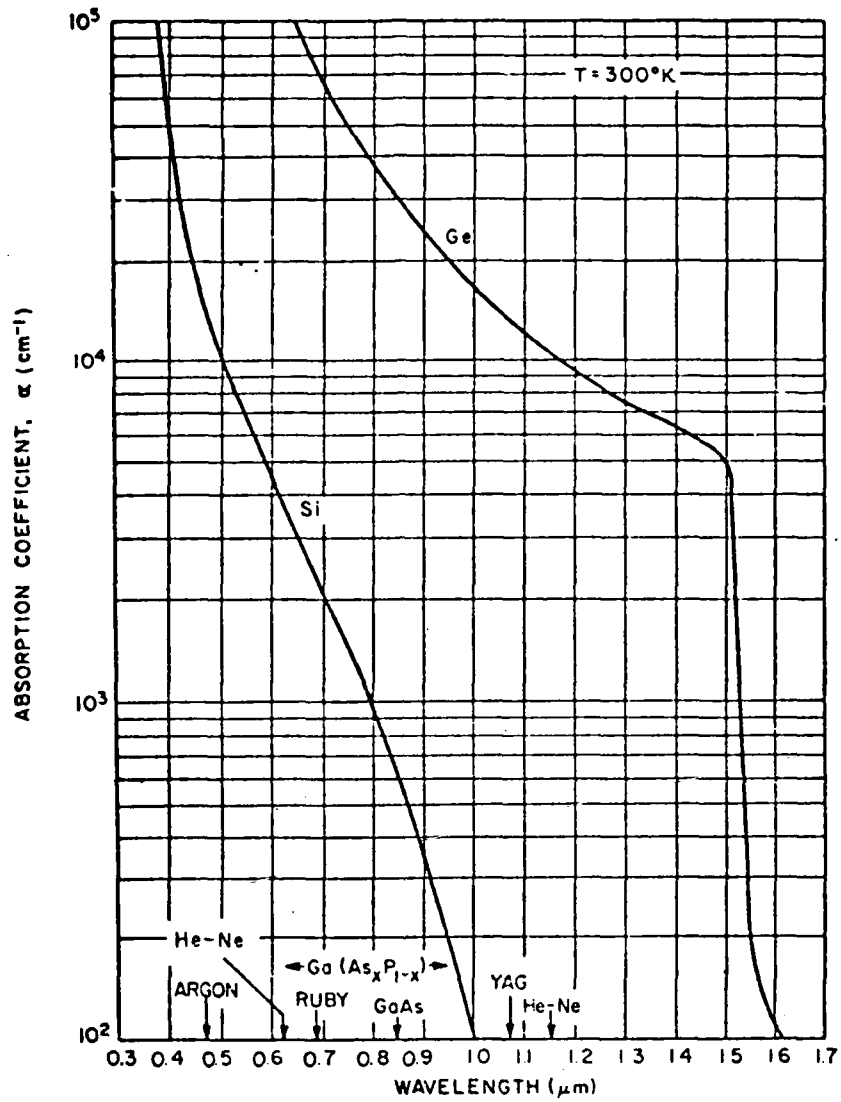


Fig 4. Absorption coefficient versus wavelength for Ge and Si at  $300^\circ\text{K}$  (Ref 14; 53).

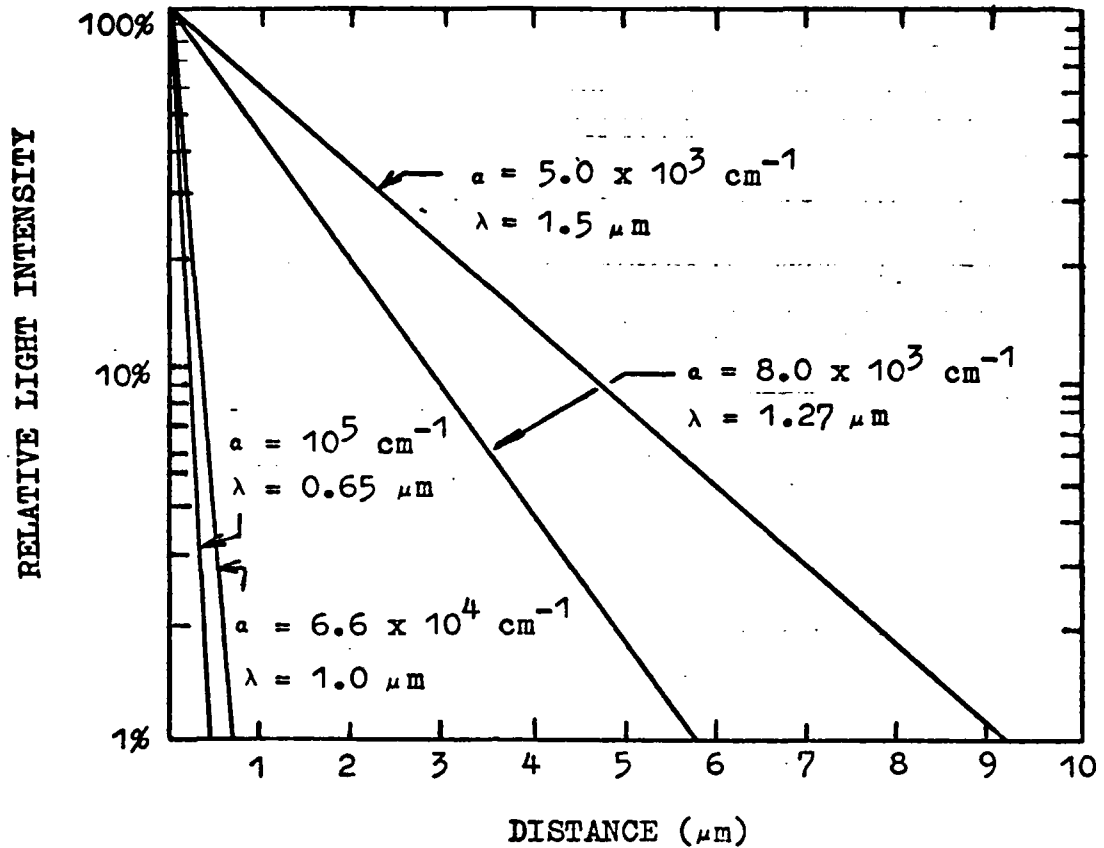


Fig 5. Exponential decay of light as it is absorbed into a material.

of the depletion region can be swept out by the field in a p-n junction and be collected, thus contributing to the detected signal current. For example, very shallow junctions are essential for collecting light at short wavelengths and little applied bias is needed to sufficiently widen the depletion region.

It is obvious why Si is chosen over Ge as the photodetector substrate for devices operating at  $0.65 \mu\text{m}$ . Si has an absorption coefficient about two orders of magnitude lower than Ge at this wavelength ( $3 \times 10^3 \text{ cm}^{-1}$  for Si versus  $10^5 \text{ cm}^{-1}$  for Ge). The majority of the light which managed to penetrate the Ge substrate would be consumed by window losses

which will be explained later. The absorption coefficient at  $1.0 \mu\text{m}$  was chosen for comparison because silicon "cuts off" at that point. The  $1.27 \mu\text{m}$  value of absorption coefficient was chosen for consideration because of the significance it has in fiber characteristics as a region of minimum dispersion and a fiber attenuation.

Figure 6 shows a plot of the depletion-layer width,  $W(\mu\text{m})$  as a function of substrate doping,  $N_B (\text{cm}^{-3})$  and applied reverse bias. It is obtained by assuming the profile of a shallow junction approximates a one-sided abrupt junction (Ref 53:89) and using the equation

$$\begin{aligned}
 W &= \sqrt{\frac{2 \epsilon_s (V_{bi} + V_{bias})}{q N_B}} \\
 &= 4.2 \times 10^3 \sqrt{\frac{V_{bi} + V_{bias}}{N_B}} \quad (6)
 \end{aligned}$$

where

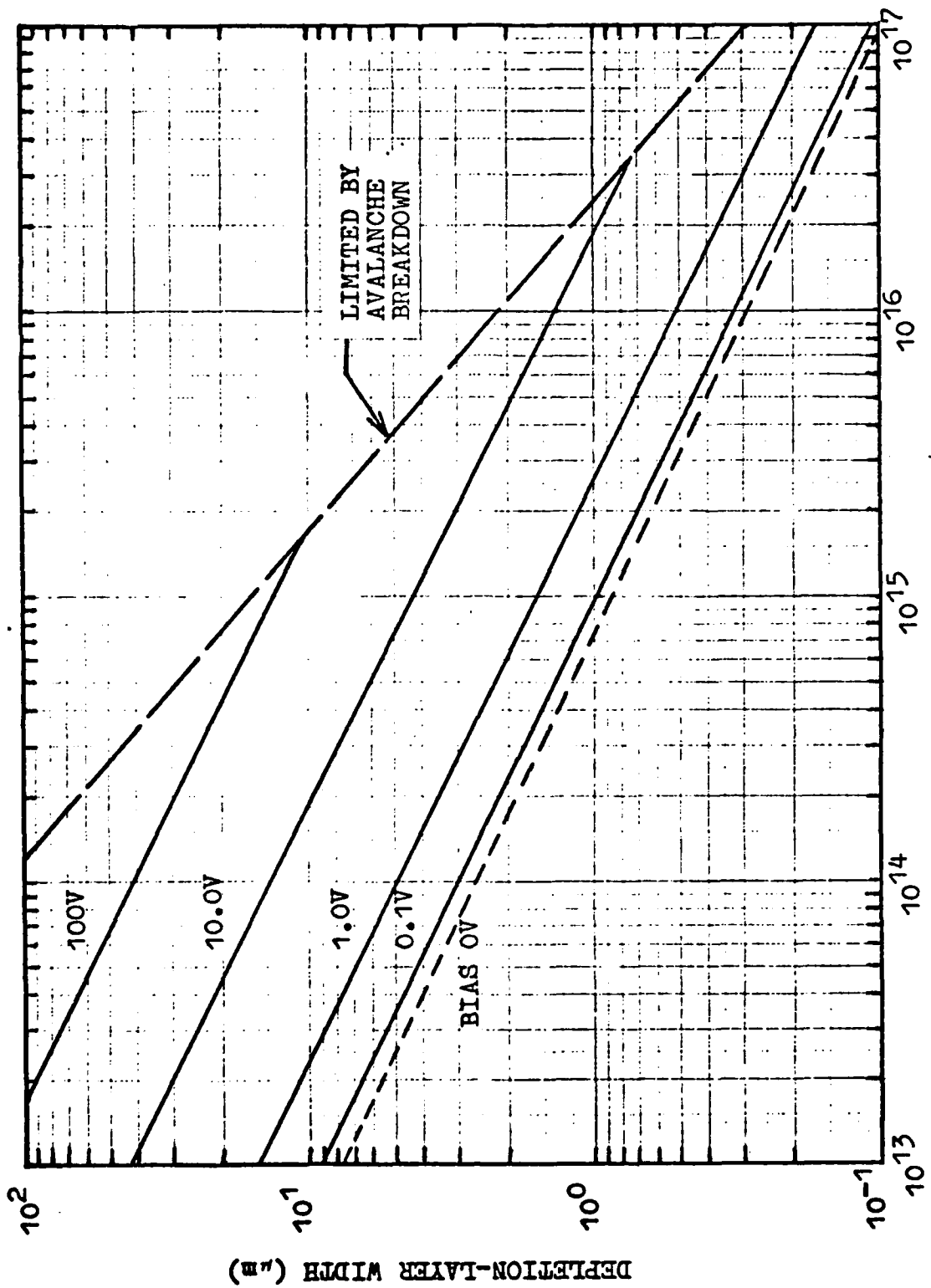
$W$  = total depletion width,  $\mu\text{m}$

$\epsilon_s$  = semiconductor permittivity, farad/cm (16 for Ge)

$V_{bi}$  = built-in potential, volts

$V_{bias}$  = applied bias voltage, volts.

The wafers used to make the devices studied in this thesis were  $3 \Omega\text{-cm}$  p-type Ge wafers, for which  $N_B \sim 10^{15} \text{cm}^{-3}$ . Using Figure 6 in conjunction with Figure 5, with the assumptions of a  $\sim 0.75 \mu\text{m}$  junction depth and at least a  $3 \mu\text{m}$  one-sided depletion-layer width, shows that the device could capture about 50% of the incident light. At  $1.5 \mu\text{m}$ , the absorption



BACKGROUND CONCENTRATION,  $N_B$  ( $\text{cm}^{-3}$ )

Fig 6. Depletion-layer width as a function of substrate doping and applied reverse bias.

coefficient for Ge drops off rapidly. Peak response has been observed to occur near  $1.5 \mu\text{m}$ . The corresponding line of Figure 5 shows that  $1.5 \mu\text{m}$  radiation will penetrate deep into the device, far beyond a single diffusion length from the depletion-layer width. The optically-generated carriers would be recombined in the bulk and never have a chance to be collected at the p-n junction. To reemphasize the focus of this thesis, at  $1.27 \mu\text{m}$ , the efficient absorption of radiation would require a shallow junction depth in the range  $0.25\text{-}0.75 \mu\text{m}$  and a depletion-layer width of  $\sim 5.5 \mu\text{m}$ .

#### Photodetector Losses

Under reverse bias, the depletion region of a p-n photodiode widens into the lightly doped side because of the one-sided abrupt junction assumption as shown in Figure 7. Also shown, are the various losses that are incurred by the viewpoint of a photodetector. The window loss is denoted by light wave (1). The n-type As doping is the window through which the radiation must penetrate. Absorption in the oxide or oxide equivalent is denoted by (2). To minimize absorption and reflection losses an antireflection (AR) coating which exhibits the quarter-wave plate effect may be needed. The third type of loss, (3), shows the path of radiation as it penetrates deep into the p-type Ge. The e-h pairs that result from carrier generation have a greater probability of being recombined before drifting back to the junction where they can be collected. Only carriers generated within a diffusion length of the junction are able to make it to the junction in time before they are recombined.

### Device Characteristics

Photoresponse. A measure of the performance of a photodetector is its responsivity. Responsivity, or photoresponse, is defined as the amount of photocurrent generated per unit of optical power incident on the device, i.e. responsivity is a measure of  $\mu\text{A}$  of photocurrent per  $\mu\text{W}$  of optical power:

$$R = \frac{I}{H} \quad (7)$$

where

R = responsivity,  $\mu\text{A}/\mu\text{W}$

I = photocurrent,  $\mu\text{A}$

H = optical power,  $\mu\text{W}$

Both the current and the power are functions of wavelength. The development of this relatively simple equation can be explained using Figure 8, which shows the energy band diagram of a p-n junction under reverse bias. The photocurrent generated, assuming total collection of the incident light and generated carriers, is

$$I = q\eta \frac{H_L}{h\nu} \quad (8)$$

where

$\eta$  = quantum efficiency, electrons/photon

$H_L$  = optical power incident on the surface,  $\mu\text{W}$

q = charge of an electron, coul

The optical power decays exponentially into the device, similarly to Equation (5):

$$H(x) = H_L \exp(-\alpha x) \quad (9)$$

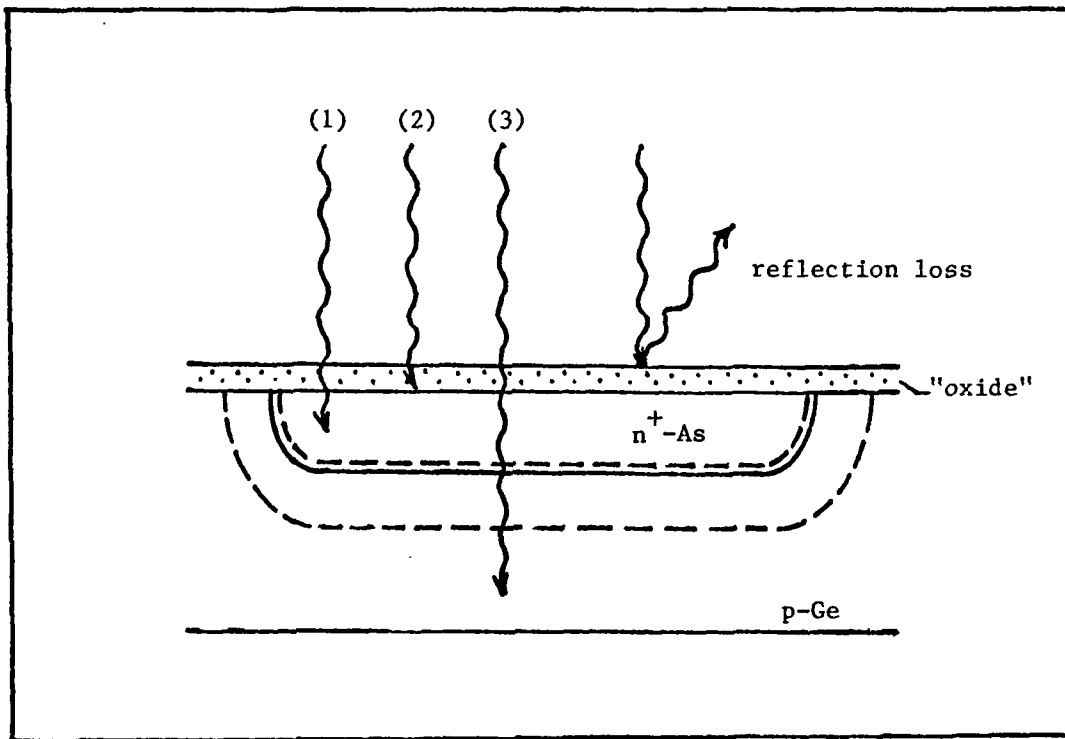


Fig 7. The p-n junction under reverse bias showing depletion layer widening and losses incurred by incident radiation.

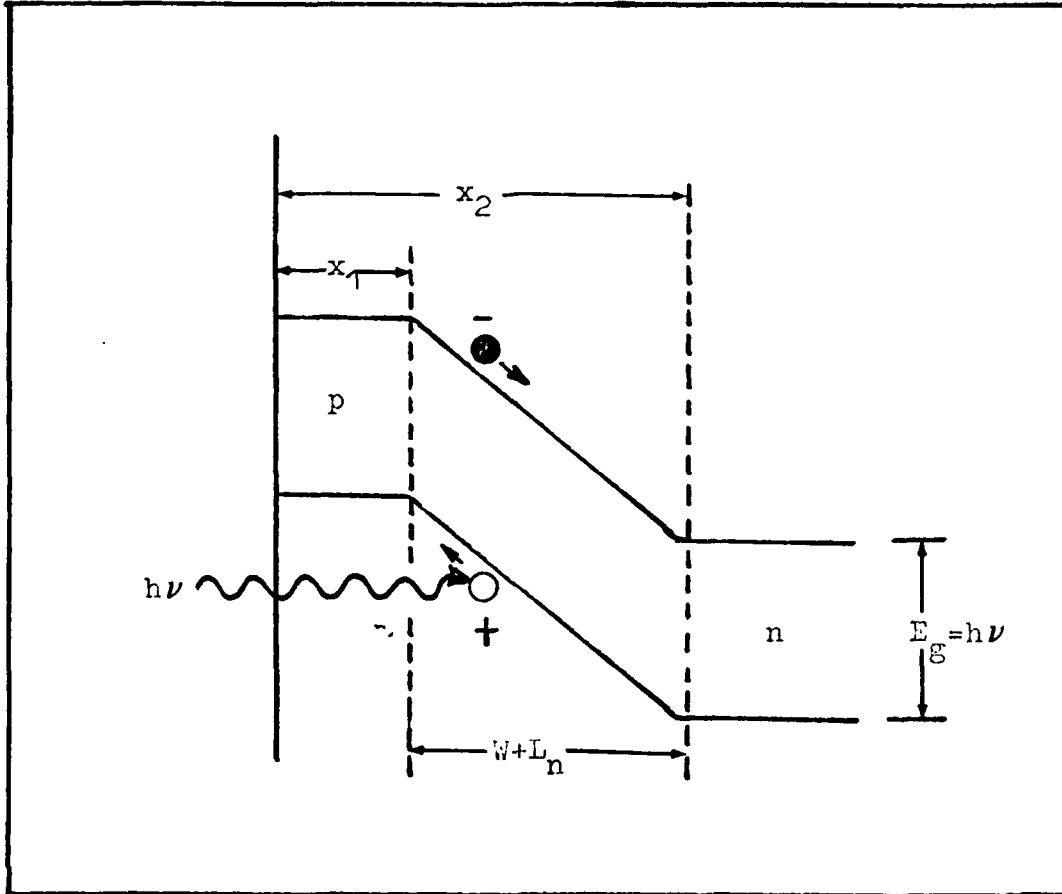


Fig 8. The energy band diagram of a p-n junction under reverse bias.

Recall that there are window losses and recombination losses incurred by the photodetector.

If collection takes place between  $x_1$  and  $x_2$ , then

$$\begin{aligned}
 I &= q\eta \frac{H(x_1) - H(x_2)}{h\nu} \\
 &= q\eta \frac{H_L [\exp(-\alpha x_1) - \exp(-\alpha x_2)]}{h\nu} \quad (10)
 \end{aligned}$$

and by the definition of responsivity:

$$\frac{I}{H} = \frac{q\eta}{hc} \lambda \left[ \exp(-\alpha x_1) - \exp(-\alpha x_2) \right] \quad \mu A / \mu W \quad (11)$$

The above expression reaffirms the notion of losses in a photodetector and that the photoresponse is a measure of the optically generated current in the depletion region of a p-n junction.

A parameter which influences the photoresponse measurement is the reflectivity of the material. In the case of no antireflection coating

$$H' = (1-R)H \quad (12)$$

where

$R$  = reflection coefficient

$H'$  = incident optical power after reflection

The reflection coefficient is determined by (Ref 53:52):

$$R = \frac{(1-\bar{n})^2}{(1+\bar{n})^2} \quad (13)$$

where  $\bar{n}$  is the refractive index (for Ge,  $\bar{n} = 3.46$ ).

Quantum Efficiency. Another measure of how effective the junction is in converting incident photons to electrons is the quantum efficiency, denoted by  $\eta$ , and expressed in units of electrons per photon. Like responsivity, quantum efficiency is affected by depletion layer width. In this case, it will be determined by the expression for responsivity

$$R = \frac{\eta \lambda q}{hc} \quad A/W \quad (14)$$

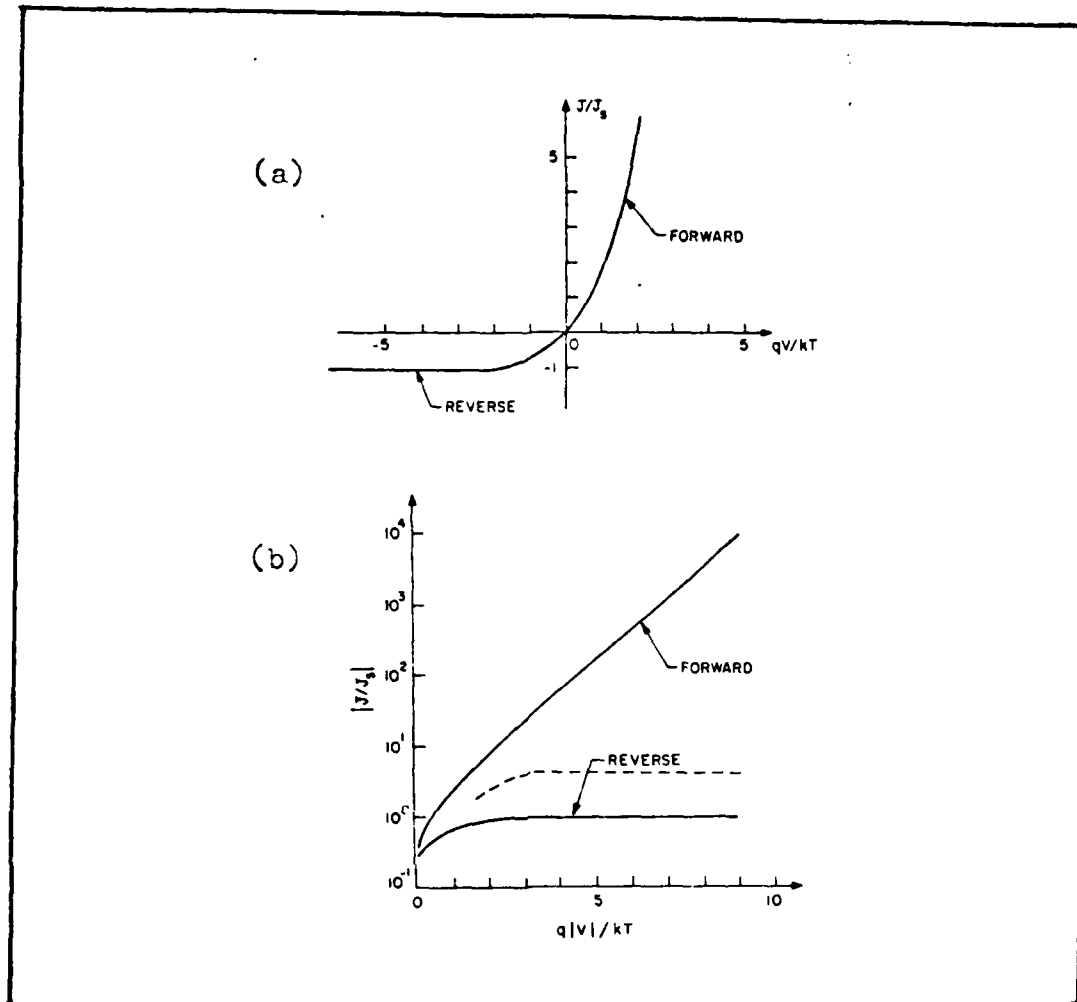


Fig 9. Ideal current-voltage characteristics  
 (a) linear plot  
 (b) semilog plot (Ref 53:101).

Solving for  $\eta$  :

$$\eta = \frac{Rhc}{\lambda q} = \frac{Ihc}{H \lambda q} \quad \text{electrons/photon} \quad (15)$$

### Diode Characteristics

The current-voltage characteristics of a diode are shown in Figure 9 for an ideal diode (Ref 53:101). The dashed line signifies the effect

of light incident on a photodiode. The generation of carriers in the depletion region as a result of photo-illumination increases the reverse leakage current. The number of carriers generated is directly proportional to the varying reverse leakage current. In terms of current density, the total current density through the depletion region under reverse bias, neglecting thermal reverse current at steady state is

$$J_{\text{tot}} = J_{\text{dr}} + J_{\text{diff}} \quad (16)$$

where

$J_{\text{dr}}$  = drift current density

$J_{\text{diff}}$  = diffusion current density

The drift current density is due to the carriers generated inside the depletion region and swept out by the electric field. The diffusion current density is due to the carriers generated outside the depletion layer in the bulk of the semiconductor and diffusing into the reverse biased junction.

The contribution from  $J_{\text{dr}}$  is determined by the rate at which electron-hole pairs are generated by the incident photon flux. The generation of the carriers drops off exponentially as expected because light intensity is absorbed exponentially as a function of distance into the semiconductor.

For distances outside the depletion layer, the minority carrier density (electrons) in the bulk of the semiconductor is obtained from the one-dimensional diffusion equation (Ref 20:126; 53:99):

$$\frac{D_n \partial^2 n_p}{\partial x^2} - \frac{n_p - n_{po}}{\tau_n} = 0 \quad (17)$$

where

- $D_n$  = diffusion coefficient for electrons,  $\text{cm}^2/\text{sec}$   
 $\tau_n$  = lifetime of excess carriers, sec  
 $n_{po}$  = density of electrons at equilibrium,  $\text{cm}^{-3}$   
 $n_p$  = minority carrier density (electrons),  $\text{cm}^{-3}$ .

Equation (17) is subject to the boundary condition

$$\begin{aligned} n_p &= n_{po} & \text{for } x &= \infty \\ n_p &= 0 & \text{for } x &= W \end{aligned} \quad (18)$$

which leads to the following solution for total current:

$$J = J_s [\exp(qV/kT) - 1] \quad (19)$$

Under reverse bias, the current density (Ref 53:100) should saturate at

$$J_s = \frac{qD_p p_{no}}{L_p} + \frac{qD_n n_{po}}{L_n} \quad (20)$$

where

- $D_p$  = diffusion coefficient of holes,  $\text{cm}^2/\text{sec}$   
 $p_{no}$  = density of holes at equilibrium,  $\text{cm}^{-3}$   
 $L_{p,n}$  = diffusion length of holes and electrons, respectively,  $\mu\text{m}$

The diffusion length for holes is defined by

$$L_p = \sqrt{D_p \tau_p} \quad (21)$$

and similarly for electrons. Assuming a one-sided  $p^+n$  abrupt, shallow junction,  $n_{po} \gg p_{no}$  and  $L_p \gg L_n$ , so the first term can be neglected.

This gives:

$$J_s \approx \frac{q D_n n_{po}}{L_n} \quad (22)$$

For

$$n_{po} = \frac{n_i^2}{N_A} \quad (23)$$

and

$$L_n = \sqrt{D_n \tau_n} \quad (24)$$

then

$$J_s = q \sqrt{\frac{D_n}{\tau_n}} \frac{n_i^2}{N_A} \quad (25)$$

For Ge, the intrinsic carrier concentration,  $n_i = 2.4 \times 10^{13} \text{ cm}^{-3}$  and for 3  $\Omega$ -cm substrate wafers,  $N_A = 1.1 \times 10^{15} \text{ cm}^{-3}$ . Using  $\tau_n = 10^{-3}$  seconds (Ref 53:58) as the minority carrier lifetime and  $kT/q = 0.0259 \text{ eV}$ , all values in Equation 25 are known except for the diffusion coefficient,

$D_n$ :

$$D_n = \frac{kT}{q} \mu_n \quad (26)$$

where  $\mu_n$  is the drift mobility of electrons,  $3900 \text{ cm}^2/\text{V-sec}$  for Ge (Ref 53:58). Appropriate substitution into Equation 25 leads to an estimate value for the saturation current density:

$$J_s = 2.67 \times 10^{-5} \text{ A/cm}^2 \quad (27)$$

To get an idea of the reverse leakage current that can be expected from shallow junction photodiodes, the current density must be multiplied by the area of the junction active in photogenerated current.

Dark current. When no light is incident on the photodiode, the current produced by the diode is known as the dark current of the detector, denoted by  $I_d$ . The dark current is a result of bulk and surface effects. The bulk leakage current depends on the active area, the resistivity of the substrate, and the bias voltage. The surface leakage current is a result of defects on the surface of the diode, which depends on cleanliness during the fabrication of the diode. It is also a function of bias voltage and surface area.

The dark current of a photodetector reduces the sensitivity of the device because it produces shot noise as given by

$$I_{\text{noise}} = (2qI_d B)^{1/2} \quad (28)$$

where

$I_{\text{noise}}$  = noise current

B = noise equivalent bandwidth (Hz)

The shot noise produced by the dark current dominates the Johnson (thermal) noise of the diode in this case.

Some methods of reducing the dark current can be used during the design and fabrication process. A deeply diffused guard ring around the active area of the diode helps reduce the dark current by shunting the surface leakage current away from the load resistor. Again cleanliness during device processing is a very important factor in reducing the leakage.

Carrier lifetimes. Note that the Equation (25) expresses the saturation current density as a function of carrier lifetime,  $\tau_n$ . A longer lifetime implies reduced leakage current, and greater sensitivity. The assumption of  $\tau_n \sim 1$  millisecond turns out to be rather high when compared to the measured lifetimes of the devices studied in this thesis as will be seen later. Equation (24) shows the direct relationship between diffusion length and longer lifetime. A longer diffusion length allows detection at longer wavelengths.

Applied Bias. The effect of applied bias was discussed earlier in this section in conjunction with Figures 5 and 6. It can be seen from this figure and Equation (6) that the depletion layer width, and in turn the sensitivity, increases with applied bias voltage. Of course, at a certain point, the increase in response is outweighed by increased noise.

#### Fabrication of Shallow Junctions

The fabrication of shallow junction Ge photodiodes can be done by two well known processes, diffusion and ion implantation. Although diffused diodes promise uniform doping across the surface of the wafer, the depth of the diffusion is difficult to control for shallow junctions. Diffusion of impurities in a Ge wafer by an infinite source is modeled

by the error function complement (Ref 20:46; 53:82):

$$C(x,t) = C_s \operatorname{erfc} \left[ \frac{x}{2\sqrt{Dt}} \right] \text{ cm}^{-3} \quad (29)$$

where

$C(x,t)$  = impurity concentration as a function of time and distance from the surface,  $\text{cm}^{-3}$

$C_s$  = impurity concentration at the surface,  $\text{cm}^{-3}$

$x$  = distance, cm

$D$  = diffusion coefficient,  $\text{cm}^2/\text{sec}$

$t$  = time, sec.

$C_s$  is fixed by the solid solubility of the impurity in Ge. For a phosphorus diffusion at  $750^\circ\text{C}$ , the solid solubility of phosphorus in Ge is  $\sim 2 \times 10^{20}$  atoms/ $\text{cm}^3$  and the corresponding diffusion coefficient is  $\sim 2.8 \times 10^{-12}$   $\text{cm}^2/\text{sec}$  (Ref 53:31,32). It should be noted, however, that in practice diffusion coefficients for most impurities vary significantly from furnace to furnace probably because of temperature variations. The impurity concentration and junction depth of shallow junction diodes can be better controlled by ion implantation. Implanted diodes studied in this thesis were fabricated using As as the impurity species. Details will follow in Chapter IV.

In considering the diode from the perspective of a photodetector application edge breakdown occurs more easily in shallow junctions (Ref 20). There are various methods of reducing edge breakdown effects which involve guard ring structures, diffused pockets of the window material on the outside of the shallow junction active area. Guard rings encourage uniform breakdown over the active area of the diode, assuming

there are no defects in the material called microplasmas, and help reduce the leakage current by shunting it to ground.

The surface leakage currents associated with shallow-junction Ge planar diodes can also be reduced by forming mesa structures. These are formed by etching the surrounding surface area of a diode to a depth below its junction. However, mesa structures, which are an absolute necessity in photodiodes made from diffused wafers, have fabrication problems. Based on practical experience, the etching process is a "dirty" step and is less convenient than planar processing. Consequently, implanted photodiodes suggest easier processing applications because they have no mesa etching requirement.

Passivating films can also be employed to reduce surface leakage currents; however, there is no workable oxide for Ge that is analogous to its  $\text{SiO}_2$  counterpart that has been found to be so useful and versatile in Si technology. The  $\text{GeO}_2$  is water soluble and highly volatile so  $\text{Si}_3\text{N}_4$  is being tried. Various combinations of these three methods: guard rings, mesas, and passivating films, can be employed to reduce the leakage currents which affect the photoresponse of the Ge photodiodes.

There are many possibilities for making contact to the diode. One method is demonstrated in Figure 10(a). A concentric ring of metallization overlaps the active area of the diode and contact is made to a "tab" extending from the ring on the outside. This technique requires an insulating oxide as shown. The simpler technique shown in Figure 10(b) is used for the diodes studied in this thesis. A concentric center contact does not require the use of an oxide but the pressure of the contact lead on the shallow junction can cause problems. It is assumed that no optical radiation penetrates the metallization, therefore the active

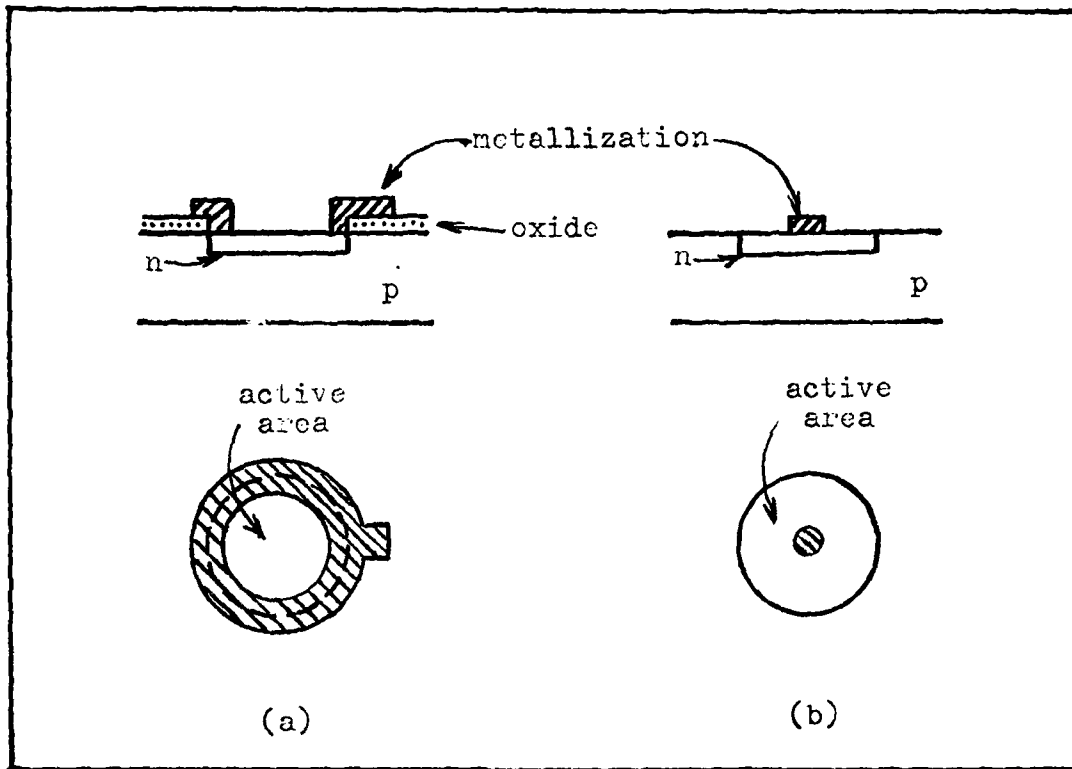


Fig 10. Making contact to the photodiode.

area of the diode is the total area minus the contact area.

In summary, the operation of a photodetector is based on the transition of carriers from the valance band to the conduction band of the semiconductor material. The transition occurs by means of absorption of the photon if optical radiation whose energy must be greater than or equal to the energy gap of the semiconductor. Photoexcited carriers are collected in the depletion region of a  $p^+n$  junction. The photocharacteristics of a photodiode are described in terms of responsivity, quantum efficiency, and dark current along with known diode performance characteristics. The shallow junction structure is intended to increase these performance ratings by collecting a greater percentage of light absorbed

by the material. Specific fabrication steps for five shallow-junction Ge photodiodes are discussed in Chapter 4. Immediately following this chapter is a theoretical discussion of the Ge-Si alloy of the future whose energy band structure resembles that of pure Ge. This explains why fabrication procedures for the photodetectors of interest reflect the material properties of pure Ge.

### III Ge-Si Alloy Theory

Two areas of research are presently in progress at the Deputy for Electronic Technology of the Rome Air Development Center relevant to the goal of photodetection near  $1.27 \mu\text{m}$ . The area in which research is progressing quickly is that of device fabrication and testing of shallow-junction structures, it is possible to obtain higher responsivity and efficiency than those of comparable devices having deeper junctions. The second area of research is the crystal growth of the Ge-Si alloy which is intended to provide the approximate value of the energy bandgap required for optimum photodetection near  $1.27 \mu\text{m}$ , i.e., the region of minimized attenuation and dispersion in an optical fiber. Eventually these two lines of work will join in a single effort to fabricate shallow-junction photodetectors using the Ge-Si alloy as the starting material. Once a working device has been achieved, it will be tested to determine if indeed the Ge-Si photodetector exhibits peak photoresponse near  $1.27 \mu\text{m}$ .

There is a third area of research which should be initiated in parallel with the two mentioned above. The physics involved in the binary alloy must not be neglected. A quantum-mechanical study of the resulting energy band structure of the Ge-Si system would be desirable as an aid in interpreting experimental results. Theoretical calculations of energy bands have significantly predicted the qualitative electrical, optical, and thermal properties of semiconductors, although quantitative properties must generally be obtained experimentally (Ref 8). Theoretically, the band structure of a crystal is described by its energy-momentum ( $\epsilon$ - $k$ ) relationship.

In this section, a brief description of the methods of determining energy band structures will be given. They include the free-electron approximation, the tight-binding approximation, the orthogonalized plane waves (OPW) method, the method of pseudopotentials, and others. The LCAO method of the tight-binding approximation is chosen as a likely approach for obtaining the energy band structure of the Ge-Si alloy. An outline of the LCAO is given and applied to the Ge-Si alloy in terms of desired parameters.

### The One-Electron Model

This section begins with the one-electron model to introduce elementary band theory. The one-electron model has been used to develop the theory of energy levels in crystals. The model leads to a qualitative energy-level structure which is similar to those in real crystals and provides an understanding of the behavior of electrons under the influence of applied electric fields. The wave nature of electrons suggests a quantum-mechanical analysis to obtain a proper description of electron behavior (Ref 8:2-3; 15:492-496; 23:1703-1710; 35:208-224; 44:3-11; 49:196-205).

The equation for an electron of mass,  $m$  moving in a region (the crystal lattice) whose potential energy is  $U(x)$ , is the wave equation known as Schroedinger's equation:

$$\frac{\hbar^2}{2m} \frac{\partial^2 \psi}{\partial x^2} + U(x)\psi = j\hbar \frac{\partial \psi}{\partial t} \quad (30)$$

This is a partial differential equation, for the moment reduced to one dimension. where the two independent variables are position,  $x$ , and time,

The solution is the wave displacement or wavefunction, denoted by  $\Psi$ , which is the dependent variable. If a particle is in a stationary state, its wavefunction is independent of time and dependent on position only. It can be factored into separate position and time factors and is expressed by

$$\Psi(x,t) = \psi(x)e^{-j(\epsilon/\hbar)t} \quad (31)$$

where  $\epsilon$  is the total energy of the electron, potential plus kinetic. Substitution of this proposed solution into the wave equation produces another differential equation for  $\psi(x)$  known as Schroedinger's time independent equation:

$$\frac{-\hbar^2}{2m} \frac{\partial^2 \psi}{\partial x^2} + U(x)\psi = \epsilon \psi. \quad (32)$$

Two factors have been neglected which greatly complicate the quantum mechanical problem. First, each electron is affected by a combination of forces produced by all the other electrons. Second, the thermal vibration of the lattice occurs in many different modes, and the resulting time-dependent forces are also applied to all the electrons thru the potential term,  $U(x)$ . The one-electron model assumes that the motion of an electron is independent of all the other electrons and of the lattice vibrations so that the environment of the electron is that of a strictly periodic potential. Under these assumptions, the solution of the Schroedinger equation for the single electron is a set of states which can be occupied by the single electron or any other electron in the crystal. The solutions are one-electron states, however, limited by the

Pauli exclusion principle which says that only one electron can occupy a given energy state at one time.

A periodic crystal potential in one dimension along one of the (100) directions in a cubic crystal is shown in Figure 11 where  $a$  is the lattice constant. The high surface potential of a crystal is neglected in favor of extending the periodicity of the crystal infinitely in all directions, or forming a closed ring with the periodic potential. The solutions to the one-electron model are wavefunctions called Bloch functions

$$\psi(x) = e^{ikx} u(x) \quad (33)$$

The properties of these wavefunctions are closely related to the periodicity of the lattice, and the allowed energy states of the electrons form continuous bands of allowed states which are separated by forbidden energy regions.

The Kronig-Penney model of an infinite one-dimensional crystal assumes the infinite one-dimensional square-well potential shown in Figure 12. Although it is a crude approximation compared to an actual crystal, it is useful in demonstrating some of the important characteristics of the quantum behavior of electrons in a periodic lattice. To solve the one-electron model using the square-well potential, Schroedinger's equation takes the form

$$\frac{\partial^2 \psi}{\partial x^2} + \frac{2m}{\hbar^2} [\epsilon - V(x)] \psi(x) = 0. \quad (34)$$

The wavefunctions must have the Bloch form in each interval of the periodic potential, i.e. where the potential is high and where it is low.

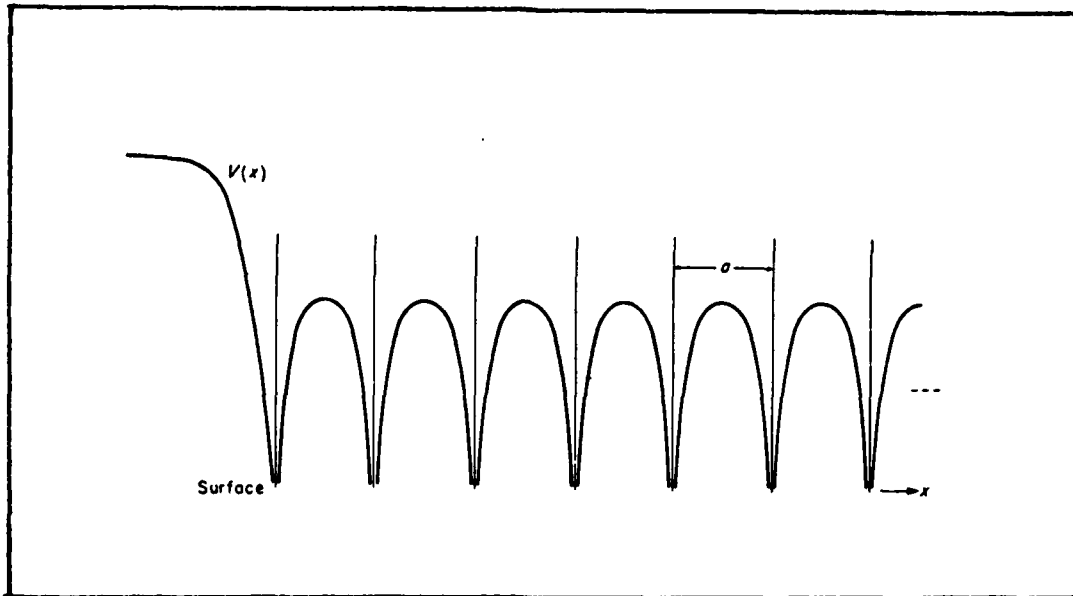


Fig 11. A representation of the potential in a perfectly periodic crystal lattice. The surface potential barrier is at the left (Ref 35:209).

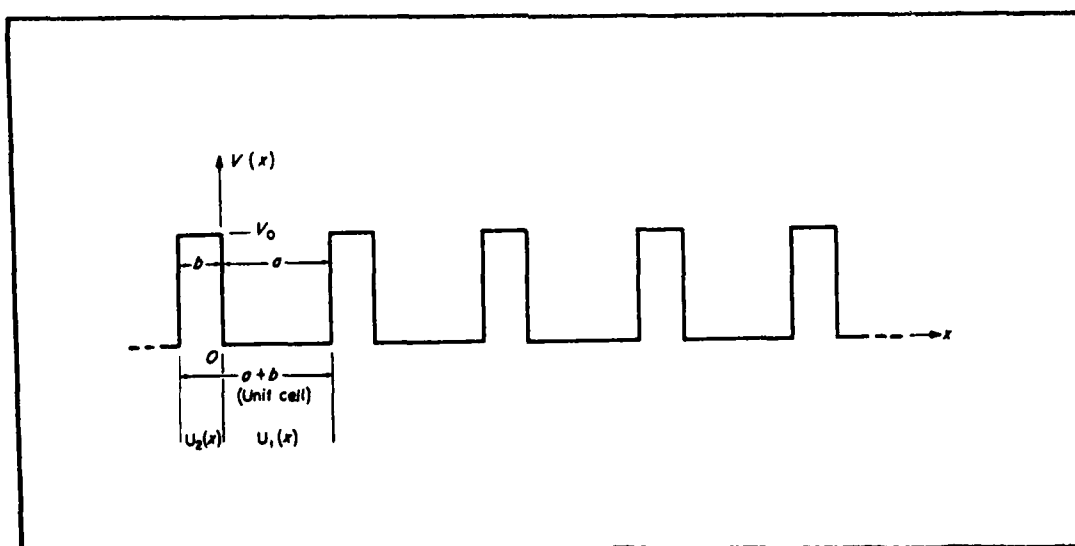


Fig 12. The ideal periodic square-well potential used by Kronig and Penny to show the general characteristics of the quantum behavior of electrons in periodic lattices (Ref 35:213).

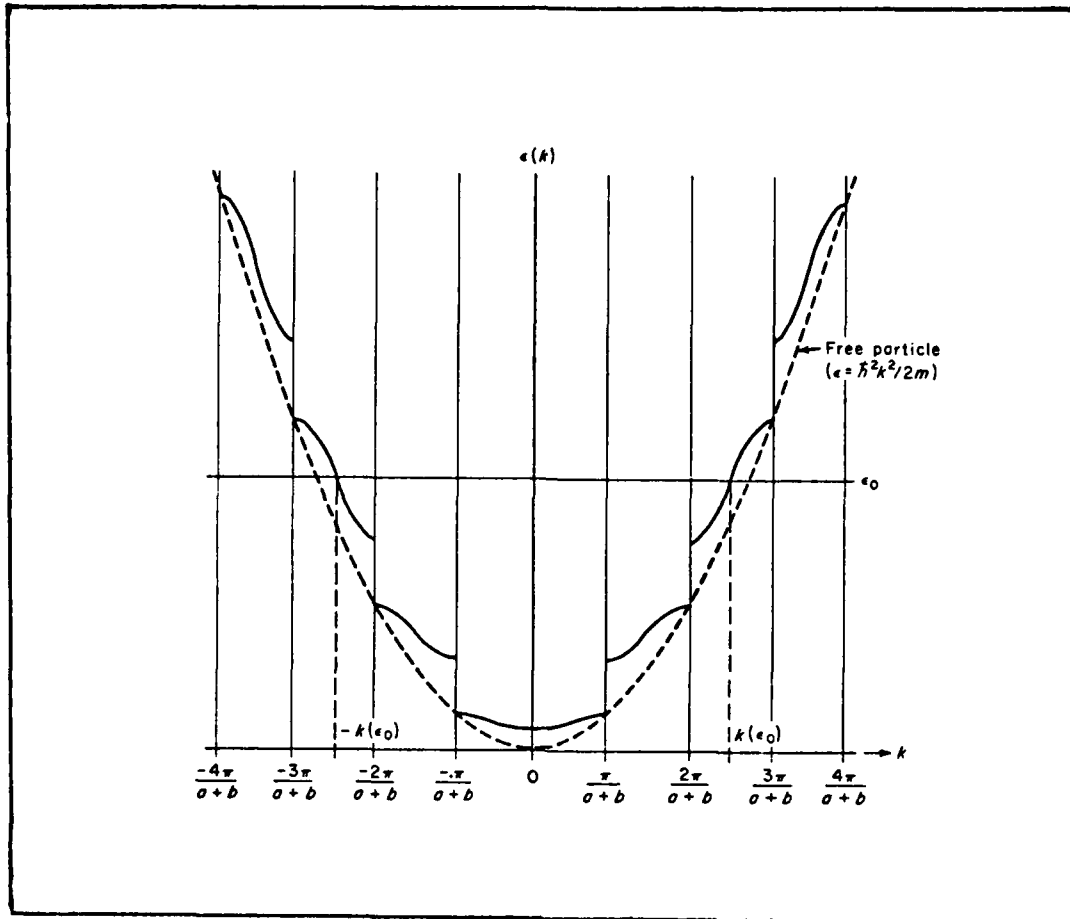


Fig 13. The energy  $\epsilon$  plotted as a function of  $k$  (Ref 35:217).

The resulting differential equations obtained by substituting the proposed solutions into the Schrodinger equation are solved by standard procedures and appropriate boundary conditions are applied. Legitimate solutions are those which produce well-behaved wavefunctions which are physically realizable. They are those which satisfy the physical requirements of the system.

A plot of energy  $\epsilon$  as a function of  $k$  as shown in Figure 13 reveals alternating regions of allowed and forbidden energy bands characteristic of the behavior of electrons in periodic lattices. For large energies,

$\epsilon(k)$  approaches the free electron relation (Ref 35:79-80)

$$\epsilon = \frac{\hbar^2 k^2}{2m} \quad (35)$$

shown by the dotted line within the allowed bands. Here, the allowed bands become very broad compared to the narrower forbidden bands.

When an electric field is applied to the crystal, the momentum of the electron in the periodic lattice changes. The effect of the periodic crystal potential is to replace the mass of a free electron with an effective mass described by

$$m^* = \frac{\hbar^2}{\frac{\partial^2 \epsilon}{\partial k^2}} \quad (36)$$

which plays the role of the mass in Newton's force equation. When the  $\epsilon-k$  curve is parabolic, which the curve in Figure 13 approximates, the effective mass becomes a constant. This is a good first approximation of the effect of the periodic crystal potential on a free electron. The consequence is that in equations involving the mass of an electron, the free-electron mass must be replaced by an appropriate effective mass which is related to the form of the  $\epsilon-k$  curve as in Equation (36). For example, the mobility  $\mu$  of a carrier is a function of the effective mass (Ref 22:165) by

$$\mu = \frac{q\tau}{m^*} \quad (37)$$

and is thus related to the energy band structure through the slope  $\partial \epsilon / \partial k$ . It should be made clear that the wavefunctions found as

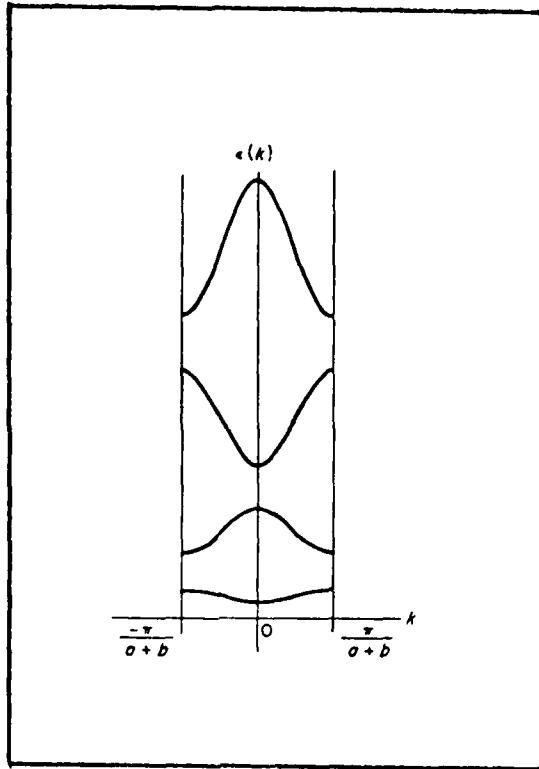


Fig 14. The reduced-zone representation of the  $\epsilon$ - $k$  plot of Figure 13 (Ref 35:220).

solutions to the wave equation actually apply to a wavepacket of many electrons rather than one electron. Therefore the effective mass applies to a wavepacket rather than one electron. Fig 13 can be conveniently condensed as in Fig 14 by translating all segments of the  $\epsilon$  versus  $k$  curve into the first Brillouin zone,  $-\frac{2\pi}{a+b} \leq k \leq \frac{2\pi}{a+b}$  where  $a$  and  $b$  are defined by Figure 12.

The one-electron model with a periodic potential has so far been used to obtain the energy band structure of a crystal ( $\epsilon$ - $k$ ), demonstrating its similarity to the free-electron model in terms of allowed and forbidden energy states. It also leads to the modification of the free-electron model by the replacement of the free electron mass by its

effective mass, a function of the slope of the  $\epsilon-k$  curve in the allowed energy bands. The model was based on the assumption that the motion of an electron was independent of all the other electrons and of the lattice vibrations, dependent only on the periodic potential of the crystal. In actual crystals, the potential function which influences the motion of an electron must be related to the ion cores and the other electrons of the crystal. An exact solution to this problem is impossible; therefore, the problem must be approached using an appropriate approximation.

#### The Free-Electron Approximation

The free-electron approximation is based on the assumption that the total energy of the electron is always large compared to the energy of the periodic potential. The resulting allowed bands will be broad and the forbidden energy regions will be very narrow (Ref 35:224-231; 44:10-15; 49:205-208). In actual crystals, the periodic potential goes to  $-\infty$  at the ion cores, but this approximation holds fairly well for the outermost electrons in metals and alkali metals.

The first step is to represent the periodic potential  $V(x)$  in a simplified one-dimensional model as (Ref 35:225):

$$\frac{-2mV(x)}{\hbar^2} = \gamma f(x) \quad (38)$$

where

$m$  = free mass of an electron

$\hbar$  = Planck's constant divided by  $2\pi$ ,  $h/2\pi$

$\gamma$  = scalar

and  $f(x)$  has the periodicity of the lattice. The Schroedinger equation

takes the form

$$\frac{d^2 \psi}{dx^2} + \left[ k_0 + \gamma f(x) \right] \psi(x) = 0 \quad (39)$$

where  $k_0$  is related to the total energy as follows

$$\epsilon = \frac{\hbar^2 k_0^2}{2m} \quad (40)$$

In solving the Schroedinger equation, the periodicity of  $f(x)$  allows it to be expressed as a Fourier series whose coefficients,  $c_n$  of  $f(x)$ , are also related to the Fourier expansion coefficients  $V_n$  of the periodic potential  $V(x)$ . The wavefunctions take the Bloch form and are in part, through  $u_k(x)$ , a periodic function of period  $a$ , and can thus also be written as a Fourier series.

In the case of a free electron,  $\gamma = 0$  and the solutions are the wavefunctions of a free particle (Ref 35:226):

$$\psi(x) = b_0 e^{ik_0 x} \quad (41)$$

where  $k_0$  is defined in Equation (39) and  $b_0$  is a constant. This solution can also be written as a Fourier series such as (Ref 35:226):

$$\psi(x) = b_0 e^{ikx} + \gamma \left[ e^{ikx} \sum_{n \neq 0} b_n e^{-2\pi i n x/a} \right] \quad (42)$$

where  $n = 1, 2, 3, \dots$

$k$  = propagation constant

$a$  = lattice constant

and whose coefficients approach zero except for  $b_0$ . For small values

of  $\gamma$  specified by the free-electron approximation the solution is valid. The solution is recognized to have the Bloch form where

$$u_k(x) = b_0 + \gamma \sum_{n \neq 0} b_n e^{2\pi i n x/a} \quad (43)$$

is obtained by dividing  $\psi(x)$  by  $e^{ikx}$ . The solution is substituted into the Schrodinger equation producing a quadratic equation in  $\gamma$  set equal to zero. After lengthy manipulation (Ref 35:226-229), the  $\epsilon$ - $k$  relationship becomes (Ref 35:229):

$$\epsilon(k) = \frac{\hbar^2}{4m} \left[ k^2 + \left( k - \frac{2\pi n}{a} \right)^2 \pm \sqrt{\left( k^2 - \left( k - \frac{2\pi n}{a} \right)^2 \right)^2 + \left( \frac{4m|V_n|}{\hbar^2} \right)^2} \right] \quad (44)$$

At the band edges  $k = k_n = n\pi/a$ ,  $\epsilon(k)$  becomes

$$\epsilon = \epsilon_n \pm |V_n| \quad (45)$$

where

$$\epsilon_n = \frac{\hbar^2}{2m} \left( \frac{n\pi}{a} \right)^2 \quad (46)$$

represents the energy of a free particle associated with the band edge points and

$$V_n = \frac{\hbar^2 \gamma}{2m} c_n \quad (47)$$

where  $V_n$  is the  $n$ th Fourier coefficient in the expansion of the periodic potential as a Fourier series (Ref 35:229).

At the band edges, the discontinuity is due to internal Bragg reflection. The  $\epsilon$ - $k$  curves shown in Figure 15 show that the curves are nearly

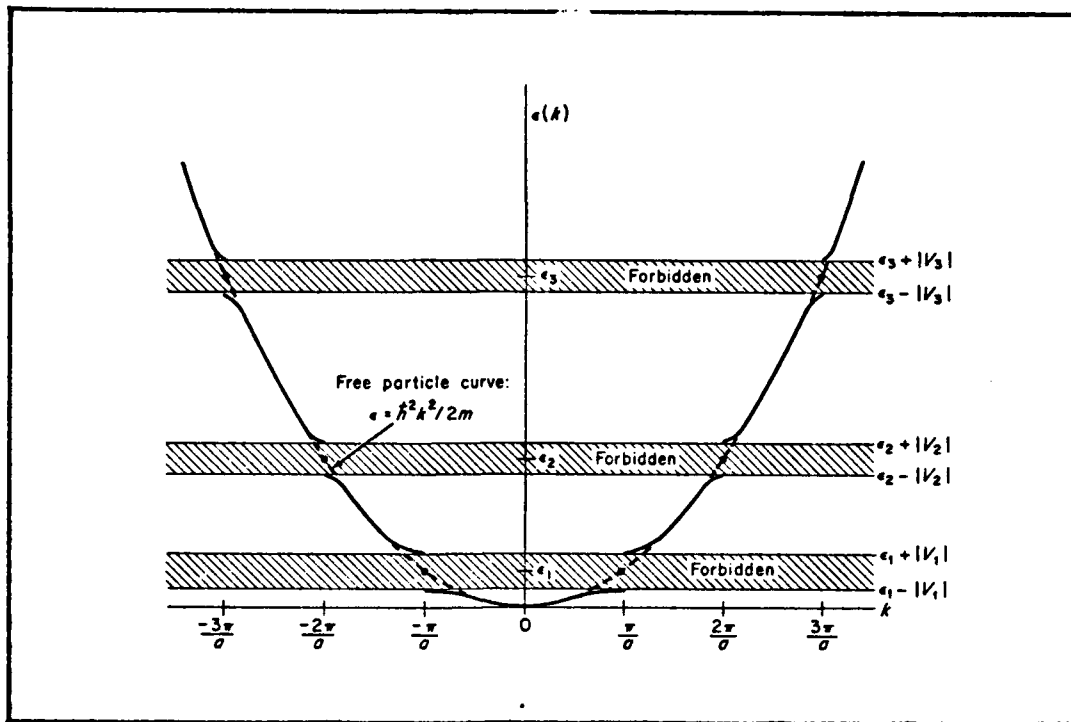


Fig 15. Schematic representation of the  $\epsilon$  versus  $k$  relation for the free electron approximation (Ref 35:230).

parabolic at the band edge points. This complicates the differentiation necessary to determine the effective mass, so the calculation is simplified by using another approximation

$$k = \frac{n\pi}{a} + k'$$

where  $k' \ll \pi/a$  which is substituted into Equation (44). The width of the forbidden energy region at the band edge  $k = n\pi/a$  is

$$\Delta\epsilon = 2|V_n| \quad (48)$$

and with the aid of the binomial theorem (Ref 35:230-231):

$$\epsilon(k) = \epsilon_n + \frac{1}{2}\Delta\epsilon + \frac{\hbar^2 k'^2}{2m} \quad (49)$$

The effective mass becomes (Ref 35:231):

$$m^* = \frac{m}{\left(1 + \frac{4\epsilon_n}{\Delta\epsilon}\right)} \quad (50)$$

where

$m$  = free mass of an electron

$\epsilon_n$  = energy of a free particle at the band edge

$\Delta\epsilon$  = width of a forbidden energy region

which is the same for holes at the top of the lower band.

The result of the free-electron approximation depicts an  $\epsilon$ - $k$  curve with broad allowed energy states and narrow forbidden regions. Raimes develops the same model by perturbation theory and use of the Fourier expansion and explains the Bragg reflection of electrons at the band edges (Ref 49:205-208). Another way to look at the assumption on which the free-electron approximation is developed is to say that the atoms of the crystal are so close together that the wave functions for electrons of neighboring atoms overlap somewhat. The strong interaction between atoms implies that the wavefunctions representing the allowed energy states in the lattice are not very similar to the wavefunctions describing the individual atoms of the crystal. There is another approximation which takes the opposite point of view, discussed in the following section.

#### The Tight-Binding Approximation

The tight-binding approximation takes the opposite point of view to the free-electron approximation. In this case, the approximation is based on the assumption that atoms of the crystal are far apart so the interaction between atoms is very weak. The resulting wavefunctions and

allowed energy states of the electrons will be closely related to the wavefunctions and allowed energy levels of the individual atoms. The results predict narrow allowed energy bands in comparison with the forbidden bands (Ref 35:231-236; 49:208-214). The particular crystal determines the appropriate approximation but it may also be necessary to find an intermediate solution for crystals which do not fit in either category. In many cases, the tight-binding approximation is best suited for semiconductors and the free-electron approximation is more suitable for metals (Ref 44:16).

The wavefunctions of the crystal in the tight-binding approximation are based on the wavefunctions of the individual isolated atoms. If  $V_0(\bar{r})$  represents the potential function of an isolated atom, the solutions of the Schrodinger equation will represent the wavefunctions of that atom. The wave equation takes the form (Ref 35:232):

$$\frac{-\hbar^2}{2m} \nabla^2 \psi_0 + V_0(\bar{r}) \psi(\bar{r}) = \epsilon_0 \psi_0(\bar{r}) \quad (51)$$

where  $\psi_0$  represents the nondegenerate wavefunction of the ground state corresponding to  $\epsilon_0$ , the energy of the ground state. When the wavefunctions of the nearby lightly bound atoms of the crystal are brought into the picture, the crystal wavefunction becomes a linear superposition of atomic wavefunctions (Ref 35:232):

$$\psi(\bar{r}) = \sum_n a_n \psi_0(\bar{r} - \bar{r}_n). \quad (52)$$

The vectors  $\bar{r}$  and  $\bar{r}_n$  are shown in Figure 16 and the sum is taken over all the atoms of the crystal,  $n$ . Since all the atoms of the crystal are the same, the coefficients  $a_n$  must have the same absolute value and must be

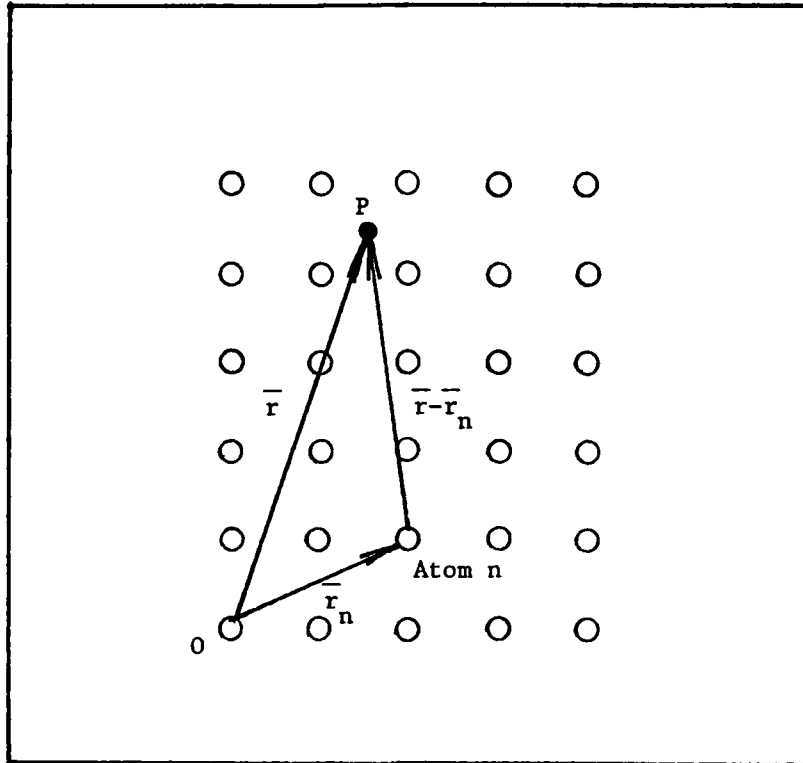


Fig 16. The  $\vec{r}$  and  $\vec{r}_n$  vectors used in the calculation of the tight-binding approximation (Ref 35:232).

able to be expressed in the form  $a e^{i\phi_n}$  where  $a$  and  $\phi_n$  are real values. The phase difference between neighboring atoms, denoted by  $\phi$ , must be the same between all atoms of the crystal along a specified crystal axis. A phase factor

$$\phi_n = \vec{k} \cdot \vec{r}_n \quad (53)$$

is chosen such that  $\vec{k}$  is a constant vector, and  $a$  is set to 1 to preserve the normalization of  $\psi_0$  (Ref 35:232). The wavefunctions take the form

$$\psi_{\vec{k}}(\vec{r}) = \sum_n e^{i\vec{k} \cdot \vec{r}_n} \psi_0(\vec{r}-\vec{r}_n) \quad (54)$$

which are in Bloch form and satisfy the Schrodinger equation for the entire crystal. The periodic potential function of Figure 17 is used in this equation as

$$\frac{-\hbar^2}{2m} \nabla^2 \psi_{\vec{k}} + V(\vec{r}) \psi_{\vec{k}} = \epsilon \psi_{\vec{k}} \quad (55)$$

The Hamiltonian of this equation is

$$H = \frac{-\hbar^2}{2m} \nabla^2 + V_0(\vec{r}) \quad (56)$$

and is broken up into two parts (Ref 35:233):

$$H = H_0 + H' \quad (57)$$

where

$$H_0 = \frac{-\hbar^2}{2m} \nabla^2 + V_0(\vec{r}-\vec{r}_n) \quad (58)$$

and

$$H' = V(\vec{r}) - V_0(\vec{r}-\vec{r}_n). \quad (59)$$

For the ground state wavefunction

$$H_0 \psi_0 = \epsilon_0 \psi_0 \quad (60)$$

and

$$\begin{aligned} H_0 \psi_0 &= \sum_n e^{i\vec{k} \cdot \vec{r}_n} H_0 \psi_0(\vec{r}-\vec{r}_n) \\ &= \epsilon_0 \sum_n e^{i\vec{k} \cdot \vec{r}_n} \psi_0(\vec{r}-\vec{r}_n) \\ &= \epsilon_0 \psi_{\vec{k}} \end{aligned} \quad (61)$$

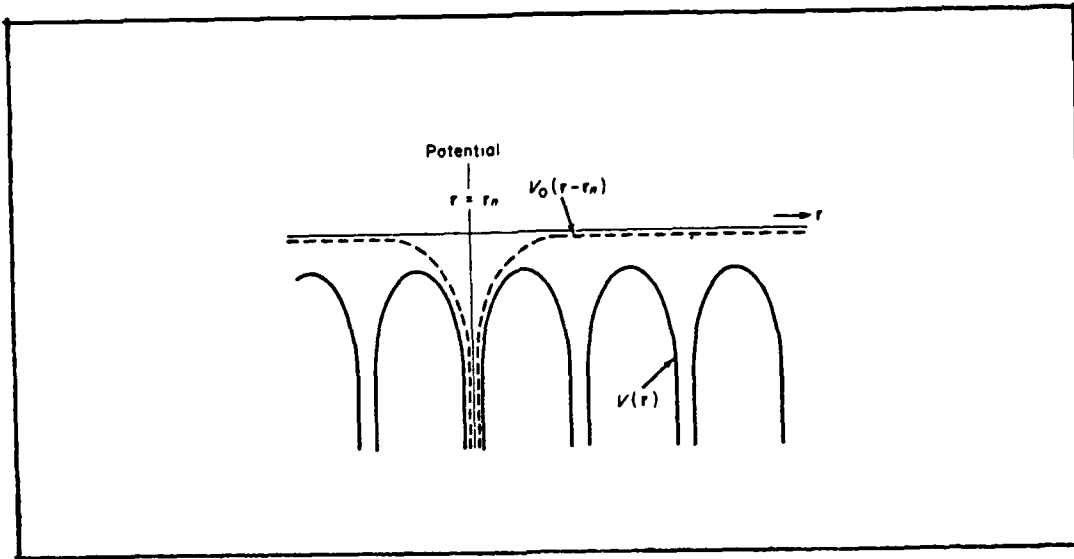


Fig 17. The potential function used in the tight-binding approximation (Ref 35:233).

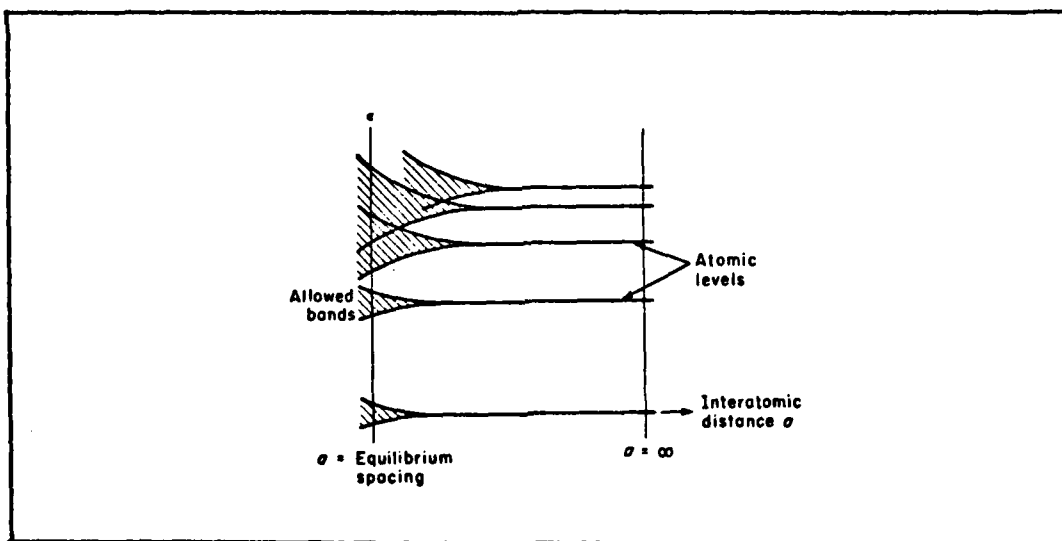


Fig 18. The discrete levels of atomic energy split into bands as the isolated atoms are assembled into a crystal lattice (Ref 35:235).

which is simply the Hamiltonian operator passed through the linear superposition of atomic wavefunctions in the equation for  $\psi_{\bar{k}}(\bar{r})$ . The constant  $\epsilon_0$  is passed through the summation sign leaving the results shown. The energy  $\epsilon$  can be obtained by finding the expectation value of the Hamiltonian operator and requiring the following conditions:

1. Neglect the small overlapping that occurs between atomic wavefunctions.
2. This implies the normalization properties of  $\psi_0$  and

$$\int_V \psi_k^* \psi_k dv = N \quad (62)$$

where N is the number of atoms in the crystal.

The derivation (Ref 35:233-235) involves the volume integral of sums, in which case the property of linearity is taken advantage of. Decreasing contributions of the terms in the final sum allow neglecting the contributions of terms from atoms which are not nearest neighbors of the atom under consideration. The spherical symmetry of the wavefunctions is assumed as a result of this approximation. So far, the case under consideration is restricted to the ground state electronic configuration in an isolated atom, its s-state.

If the vector  $\bar{r}_m$  connects an atom at the origin to its nearest neighboring atom, at the origin (Ref 35:234):

$$-\alpha = \int_V \psi_0^*(\bar{r}) V(\bar{r}) - V_0(\bar{r}) \psi_0(\bar{r}) dv \quad (63)$$

while for the nearest neighbors (Ref:35:234):

$$-\beta = \int_V \psi_0^*(\bar{r}-\bar{r}_m) V(\bar{r}) - V_0(\bar{r}) \psi_0(\bar{r}) dv. \quad (64)$$

The  $\epsilon$ - $k$  relationship obtained by summing over the nearest neighboring atoms is (Ref 35:234):

$$\epsilon(\bar{k}) = \epsilon_0 - \alpha - \beta \sum_m e^{-i\bar{k} \cdot \bar{r}_m} \quad (65)$$

where  $\alpha$  and  $\beta$  are determined from Equations (62) and (63).

The range of allowed energy values corresponds to the vector and forms an energy band in the same way as in the free-electron approximation. The minimum value of the energy occurs where  $\bar{k}$  is the zero vector and the maximum value of energy depends on the lattice constant  $a$  which appears in the components of  $\bar{r}_m$ . In the limit as the atomic spacing becomes large the tight-binding model becomes a very good approximation. The allowed energy bands become narrow and approach a single discrete energy value, the s-state of an isolated atom, as shown in Figure 18.

An electron with low momentum will be found at the bottom of an energy band where  $\epsilon$  versus  $k$  is a parabolic relationship. The electron then behaves like a free electron. The effective mass of the electron in a particular direction is given by the following equation using the slope of the  $\epsilon$ - $k$  curve in one dimension (Ref 35:236):

$$m^* = \frac{\hbar^2}{2\beta a^2} \quad (66)$$

where  $a$  is the lattice constant and  $\beta$  is defined by Equation (64). The effective mass is an isotropic, that is, not the same in all directions of the crystal. In the limit of the tight-binding approximation, the electron becomes heavy and not transferred easily from one atom to another.

The tight-binding approximation is also known as the LCAO (Linear Combinations of Atomic Orbitals) approximation (Ref 52) and is also

described in connection with the hydrogen molecule (Ref 49:Section 5.8).

The LCAO method has many qualitative features:

1. It gives solutions showing the correct symmetry properties of the energy bands.
2. It provides easy access to solutions for energy bands of the Brillouin zone whereas other approximate methods become too difficult at other than certain symmetry points in the Brillouin zone.
3. By retaining only the terms which make the method qualitatively correct, the LCAO method is a convenient interpolation tool.

The Hamiltonian operator can be represented in the form of a matrix whose elements are related to the energy components of the Bloch functions and whose integrals are replaced by simplifying disposable constants. The LCAO method for the crystal lattice having a diamond structure as is found in Ge is outlined by Slater and Koster (Ref 52:1516-1524) and will be discussed in detail later.

#### Orthogonalized Plane Waves (OPW)

In the orthogonalized plane wave method (Ref 44:42-43) the Bloch function is expanded into many plane waves to represent its rapid variations near the ion core. The orthogonalized function is a linear combination of plane waves and atomic wavefunctions of the occupied states of the ion cores. The new states derived from the OPW methods show that the band energies are very close to the free electron energies except for the points in  $k$ -space very near to the boundary of a Brillouin zone (Ref 29: 285).

The ion cores are given by atomic orbital states assumed to be orthonormal and related to the periodicity of the lattice. The core functions are given by (Ref 44:42):

$$\phi_{\bar{k},j}(\bar{r}) = \frac{1}{\sqrt{N}} \sum_{\bar{R}_n} e^{i\bar{k} \cdot \bar{R}_n} u_j(\bar{r} - \bar{R}_n) \quad (67)$$

which are related to the periodicity of the lattice by

$$\phi_{\bar{k},j}(\bar{r} + \bar{R}_1) = \frac{1}{\sqrt{N}} \sum_{\bar{R}_n} e^{i\bar{k} \cdot \bar{R}_n} u_j(\bar{r} + \bar{R}_1 - \bar{R}_n) \quad (68)$$

Linearity under summation allows this to be written as

$$\begin{aligned} \phi_{\bar{k},j}(\bar{r} + \bar{R}_1) &= \frac{e^{i\bar{k} \cdot \bar{R}_1}}{\sqrt{N}} \sum_{\bar{R}_n} e^{i\bar{k} \cdot (\bar{R}_n - \bar{R}_1)} u_j(\bar{r} + \bar{R}_1 - \bar{R}_n) \\ &= e^{i\bar{k} \cdot \bar{R}_1} \phi_{\bar{k},j}(\bar{r}) \end{aligned} \quad (69)$$

for  $\bar{R}_n$  replaced by  $\bar{R}_n - \bar{R}_1$  (Ref 44:42). The resulting Bloch function must have the periodicity of the lattice.

The next step is to expand the wavefunctions into plane waves,  $e^{i\bar{k} \cdot \bar{r}}$ , orthogonal to the corresponding wave vectors of the wavefunction according to (Ref 44:43):

$$\psi_{\bar{k}} = \frac{e^{i\bar{k} \cdot \bar{r}}}{(N \Omega_0)^{1/2}} - \sum_j \mu_{\bar{k},j} \phi_{\bar{k},j}(\bar{r}) \quad (70)$$

where the orthogonality is defined by

$$\int \phi_{\bar{k},1}^*(\bar{r}) \psi_{\bar{k}}(\bar{r}) d^3 r = 0 \quad (71)$$

When the equations for  $\phi_{\bar{k},j}(\bar{r}+\bar{R}_1)$  and  $\psi_{\bar{k}}(\bar{r})$  are substituted into the equation for orthogonality, two sums of integrals are obtained which reduce to

$$\int u_1^*(\bar{r}-\bar{R}'_n) u_j(\bar{r}-\bar{R}_n) d^3 r = \delta_{nn'} \delta_{jl} \quad (72)$$

assuming the atomic wave functions are orthogonal and do not overlap (Ref 44:43). The coefficients of expansion, become (Ref 44:43):

$$\mu_{\bar{k},1} = \frac{1}{\Omega_o^{1/2}} \int_{\text{all space}} e^{i\bar{k}\cdot\bar{r}} u_1^*(\bar{r}) d^3 r \quad (73)$$

The orthogonalized plane waves can be obtained by substituting these coefficients into the equation above. When the electron is far from the ion core, the OPW emulate plane waves. Near the ion core, the OPW behave like atomic orbitals (Ref 44:43). The precision of the OPW method depends upon the accuracy of the assumed potential, the accuracy of the eigenstates assumed for the core, and the number of terms admitted to the Fourier representations of the crystal wave functions. The OPW method was applied to Si and Ge by Herman as shown in Figure 19. The orthogonalization of plane waves to ion cores is difficult so a related method is discussed below.

#### The Pseudopotential Method

The pseudopotential method shows the orthogonal relationship between plane waves and ion core wavefunctions more clearly (Ref 44:44-45) by examining the orthogonality between the wavefunction of an electron in the valence band and the core function. This relationship is expressed by

$$\psi_{\bar{k}i} = v_{\bar{k}i} + \sum_j a_{\bar{k}j}^i \phi_{\bar{k}j} \quad (74)$$

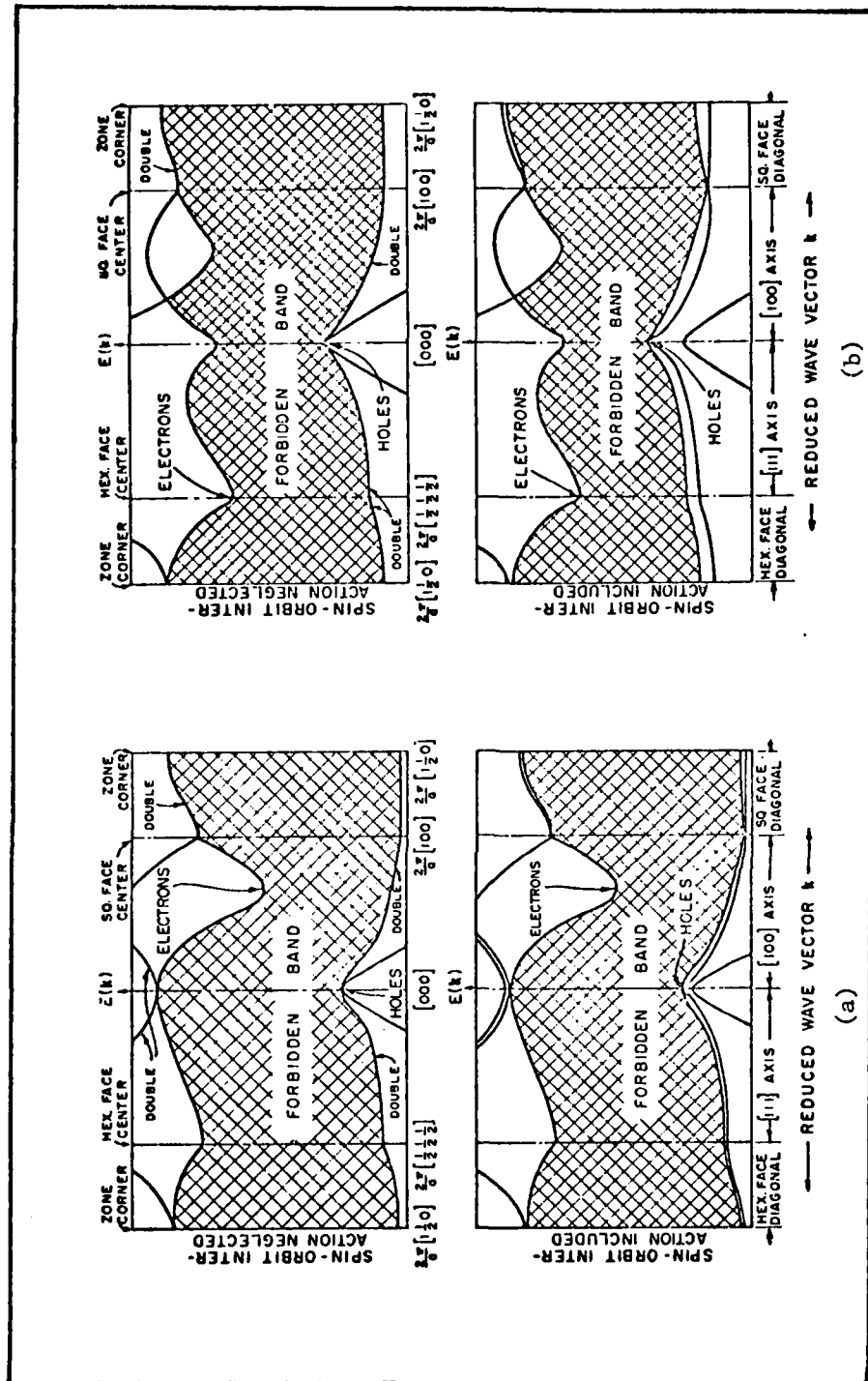


Fig 19. The energy band structures of a) Si and b) Ge (Ref 23:1716).

where

$$\begin{aligned} a_{kj}^i &= - \left( \phi_{ki} / \nu_{kj} \right) \\ &= - \int \phi_{ki}^* \nu_{kj}(\bar{r}) d^3 r \end{aligned} \quad (75)$$

The problem is in determining  $\nu_{ki}$ . By determining the eigenfunctions for the crystal Hamiltonian (obtained by the tight-binding approximation) which represent the core function by

$$H \phi_{kj} = \epsilon_{kj} \phi_{kj} \quad (76)$$

and

$$H \psi_{ki} = \epsilon_{ki} \psi_{ki} \quad (77)$$

the equation becomes

$$H \nu_{ki} + \sum_j a_{kj}^{-1} (\epsilon_{kj} - \epsilon_{ki}) \phi_{kj} = \epsilon_{ki} \nu_{ki} \quad (78)$$

The pseudopotential is defined by

$$V_p = \sum_j a_{kj}^i (\epsilon_{kj} - \epsilon_{ki}) \frac{\phi_{kj}}{\nu_{ki}} \quad (79)$$

or

$$(H+V_p) \nu_{ki} = \epsilon_{ki} \nu_{ki} \quad (80)$$

The pseudopotential represents a repulsive force which distorts the actual crystal potential. The results of this method for Ge and Si are shown

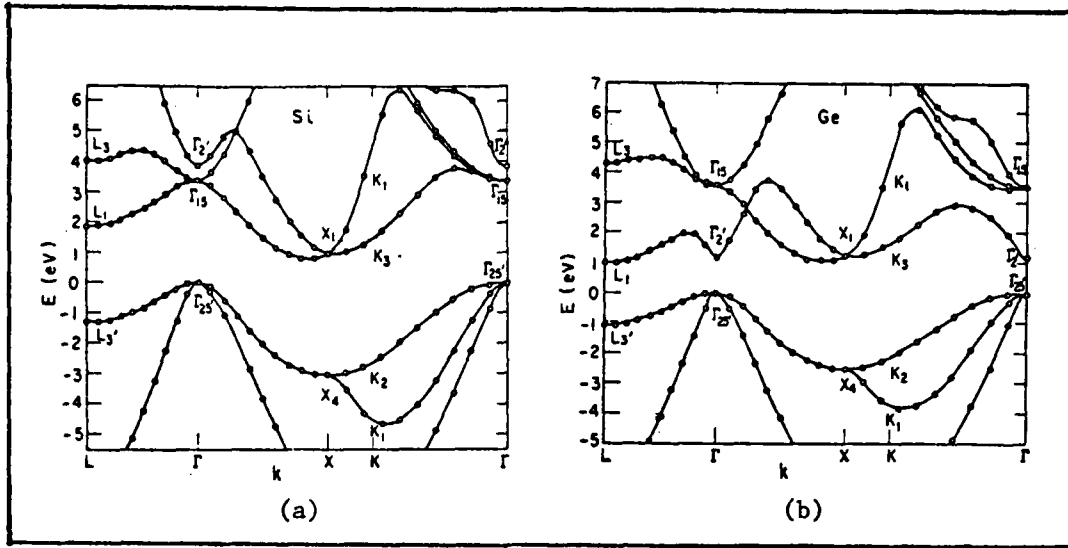


Fig 20. The energy band structures for a) Ge and b) Si using the method of pseudopotentials (Ref 10:739).

in Figure 10 (Ref 10:793; 29:316-317).

#### The Cellular Method

The cellular method is an old, specialized method for finding  $\epsilon(k)$  at a point of high symmetry (Ref 23; 44:45-75). The method involves solving the Schrodinger equation in a single atomic cell whose wavefunctions must satisfy the boundary conditions in terms of the derivatives given by Bloch's Theorem. Since boundary conditions are too complicated in complex crystals and applicable only to simple ones, it is assumed the cellular method would not be suitable for the Ge-Si alloy. Also, assumptions based on spherical symmetry of the lattice potential may not be accurate in the binary alloy case.

#### Effective Mass Approach

An adaptation of the cellular method to the states at the bottom of

the lowest valence band form the basis of this approach (Ref 44:46-47). Since the calculations are based on the assumption of spherical symmetry to determine the boundary conditions, it is surmised that this approach would not be appropriate to the case of the Ge-Si alloy for the same reasons given for the cellular method.

#### Augmented Plane Waves

In the augmented plane wave method, the wavefunction of an electron is expanded in terms of a combination of outer plane waves and inner spherical waves (Ref 44:47). Spherical assumptions have been previously mentioned as inadequate for the binary alloy so this method is not advisable for theoretical determination of the  $\epsilon$ - $k$  structure of Ge-Si.

#### Ge-Si Alloy Considerations

Although an alloy is not a perfect crystal, one can still speak of its energy band structure. The allowed bands are energy intervals in which there is a high density of allowed states, and the forbidden bands are energy intervals in which there is a low density of allowed states (Ref 23:1721-1722). The Ge-Si alloy is treated as having an energy band structure which is very similar to perfect crystals and the optical gap is considered to be a measure of the width of a forbidden band.

The Ge-Si energy band structure has been described previously in Figure 3 (Ref 27; 23:1722; 8:76). As Si is added to Ge in the 0-15% range, the lowest conduction band moves away from the highest valence band. The position of the minima along the (111) and (100) directions also changes in terms of the distance the minima move away from the edge of the valence band. Since the (111) minima lie below the (100) minima

in the range of interest, and the (111) minima in the conduction band moves away from the valence band at a faster rate than the (100) minima, the optical gap is determined by the position of the (111) minima. The conduction band minimum at the origin moves away from the valence band edge much more rapidly than the (111) and (100) minima and therefore does not influence the measurement of the energy gap. Magnetoresistance measurements have been shown to be consistent with the theory thus described (Ref 23:1722) for the range of interest of MOL % Si in Ge.

#### The Tight-Binding (LCAO) Approach to the Ge-Si Alloy

The decision to apply the tight-binding approximation to the Ge-Si alloy was based on the approximation's suitability for semiconductors. The equivalent simplified LCAO method for periodic potentials has been described by Slater and Koster for diamond structures, specifically Ge, and compared with Herman's OPW calculations (Ref 52:1516-1524).

General Approach of the LCAO Method for Solids. The following discussion is taken after a rather complete article by Slater and Koster describing the application of the LCAO method for the periodic potential problem (Ref 52). Recall that the LCAO method used to solve the problem of the periodic potential consisted of taking a linear combination of atomic orbitals of the various atoms of the crystal. The coefficients of the linear combination are equivalent to the values of the plane wave  $e^{i\vec{k}\cdot\vec{R}}$  at the various positions  $\vec{R}$  where the atoms are located. The method can involve many complicated integrals which must be evaluated. These integrals are treated as disposable constants which in turn are chosen to fit the results of more accurate calculations, such as the OPW method,

at restricted points of symmetry in the Brillouin zone (Ref 52:1498-1502).

Consider an atomic orbital  $\phi_n(\bar{r}-\bar{R}_i)$  located on an atom at a vector position  $\bar{R}_i$ , where the subscript n denotes the quantum numbers. The Bloch sum for one atom in the unit cell of the crystal (Ref 52:1498):

$$\sum \underbrace{(\bar{R}_i)}_{\substack{\text{position} \\ \text{of an atom}}} \underbrace{\exp(i\bar{k}\cdot\bar{R}_i)}_{\substack{\text{the plane wave} \\ \text{at } \bar{R}_i}} \underbrace{\phi_n(\bar{r}-\bar{R}_i)}_{\substack{\text{nth atomic orbital} \\ \text{of an atom at } \bar{R}_i}} \quad (81)$$

will be extended over the atoms in equivalent positions in all the unit cells of the crystal. Normalization will be set up later. Such a Bloch sum can be written corresponding to each atomic orbital of a particular atom, and for each atom in the unit cell of the crystal. The set of linear combinations is equivalent to the set of sums of atomic orbitals operated on by the Hamiltonian operator. The matrix of the Hamiltonian operator has no diagonal components representing the kinetic energy and periodic potential functions for Bloch sums with different  $\bar{k}$ 's. For Bloch sums with the same  $\bar{k}$  values, there are matrix components of the Hamiltonian which do not vanish. These correspond either to different atomic orbitals on the same atom, or to atomic orbitals on different atoms in the unit cell. Some nondiagonal components of the Hamiltonian matrix vanish at special symmetry points of the Brillouin zone or special values of  $\bar{k}$ . The vanishing feature of some of the matrix elements determines the special properties of the energy bands at the symmetry points.

An approximate solution of the periodic potential problem can be set up using the following steps (Ref 52:1498-1500):

1. A finite set of atomic orbitals is taken on each of the atoms of the unit cell, starting with the lowest atomic states and

ending with the highest levels occupied by the crystal (or a little higher).

2. A Bloch sum is constructed from each of the atomic orbitals.
3. For a given value of  $\bar{k}$ , a wave function is set up as a linear combination of all the Bloch sums.
4. There are matrix components of energy between all these Bloch sums producing a secular problem of an order equal to that of the total number of atomic orbitals considered. At special values of  $\bar{k}$ , the secular equation can be factored and thus greatly simplified.
5. The secular equations can be solved using modern digital computers to give wavefunctions and energy levels which form useful approximations to the periodic potential problem.
6. For a given value of  $\bar{k}$ , the secular equation has distinct roots. Wavefunctions of different  $\bar{k}$  values which have the lowest energy are grouped together into the lowest energy band, and similarly for the second energy band on up.
7. At special symmetry points, the energy bands can be degenerate.

The LCAO method described above is a good approximation to the periodic potential problem but it requires a great amount of numerical work to compute the various matrix components of energy. These will be simplified later on. The choice of one set of atomic orbitals over another can make the calculation of the matrix components or the solving of the secular equation more convenient, but the final result is the same regardless of the set of atomic orbitals used to start with.

So far, the general outline of the LCAO method has been described. When treated as an interpolation tool, the complicated rigorous application of the method can be simplified. The first simplifying step involves the atomic orbitals. The Bloch sums of the atomic orbitals  $\phi_n$  on the various atoms of a unit cell are not orthogonal to each other. This is because the atomic orbitals of different atoms are not orthogonal. This complicated situation is removed by obtaining a new set of atomic orbitals which are linear combinations of the original orbitals and are orthogonal to each other. The orthogonal atomic orbitals are denoted by  $\psi_n$ . This simplification does not solve the periodic potential problem. The non-diagonal matrix components of energy between the Bloch sums from different  $\psi_n$  remain to be found. The  $\psi_n$ , also known as Lowdin functions, have the symmetry properties of the  $\phi_n$  from which they were derived, which thus simplifies the problem of solving the secular equation (Ref 52:1524).

Bloch sums are constructed from the Lowdin functions in the form (Ref 52:1501):

$$N^{-1} \sum (\bar{R}_i) \exp i(\bar{k} \cdot \bar{R}_i) \psi_n(\bar{r} - \bar{R}_i) \quad (82)$$

which are normalized and orthogonal. Periodic boundary conditions are assumed and N equals the number of unit cells in the crystal. The sum is over the N unit cells and the normalization is over the repeating crystal. The Bloch function is formed from just one atomic orbital per unit cell which will have implications in the diamond structure. The next step is to find the matrix component of energy between two of these Bloch sums. The matrix component is (Ref 52:1501):

$$N^{-1} \sum (\bar{R}_i, \bar{R}_j) \exp i\bar{k} \cdot (\bar{R}_j - \bar{R}_i) \\ \times \int \psi_n^* (\bar{r} - \bar{R}_i) H \psi_m (\bar{r} - \bar{R}_j) dv \quad (83)$$

where  $H$  the Hamiltonian operator,  $\bar{R}_i$  ranges over the positions of the atoms on which the orbitals  $\psi_n$  are located, and  $\bar{R}_j$  ranges over the positions of orbitals  $\psi_m$ . The sum is over  $N$ . The double sum can be written as a single summation because the single summation is multiplied by  $N$ , cancelling  $N^{-1}$ . If  $\bar{R}_i$  represents the position of the atom in the central unit cell having orbital  $\psi_n$ , and the sum is taken over  $\bar{R}_i$ , the remaining single sum over  $\bar{R}_j$  amounts to summing over all the neighbors of the original atom. This gives (Ref 52:1501):

$$\sum (\bar{R}_j) \exp i\bar{k} \cdot (\bar{R}_j - \bar{R}_i) \int \psi_n^* (\bar{r} - \bar{R}_i) H \psi_m (\bar{r} - \bar{R}_j) dv \quad (84)$$

where  $\bar{R}_j - \bar{R}_i$  represents the vector displacement from the atom on which the orbital  $\psi_n$  is located, to a neighboring atom on which the orbital  $\psi_m$  is located. Each term depends on the propagation constant  $\bar{k}$  and each term of the summation is related to a pair of orbitals of neighboring atoms.

Finding the Lowdin functions from the atomic orbitals can be very difficult; for the moment, it will be assumed to have been accomplished. Since each  $\psi_n$  is a combination of atomic orbitals on many nearby atoms, the integral in Equation (84) represents a linear combination of many integrals of the form (Ref 52:1501):

$$\int \phi_n^* (\bar{r} - \bar{R}_i) H \phi_m (\bar{r} - \bar{R}_i) dv. \quad (85)$$

The Hamiltonian,  $H$  involves a periodic potential which can be written as the sum of a kinetic energy operator and a potential. The potential is approximately a sum of spherically potential wells located at all the atoms of the crystal. The integral can then be viewed as a linear combination of integrals of a product of three functions (Ref 52:1501):

- 1) an atomic function  $\phi_n^*(\bar{r}-\bar{R}_i)$  located on the atom at  $\bar{R}_i$ ,
- 2) another atomic function  $\phi_m(\bar{r}-\bar{R}_j)$  on the atom at  $\bar{R}_j$ , and
- 3) a spherical potential function located on a third atom.

These three-center integrals are very difficult calculations as is the calculation of the matrix components of energy; in fact, the calculations are impossible without the use of high-speed computers. This is the point at which the simplifications of the LCAO are introduced which converts the method from a rigorous one to a simple interpolation method.

The form of Equation (84) is used for the matrix components of energy but the integrals are replaced by disposable constants chosen to fit accurately determined energies at particular values of  $\bar{k}$ . Some care must be taken regarding the precision of the method which depends upon the finite number of disposable constants. Only a finite number of arbitrary constants is necessary to fit a finite number of accurate calculations of energy. In choosing a finite number three simplifying observations are made (Ref 52:1501-1504) and are discussed in the following paragraphs.

The integrals in Equation (84) will get smaller numerically as the  $i$ -th and  $j$ -th atoms get farther apart. If the functions  $\psi_n$  were atomic orbitals then the integral would go to zero unless the two atoms were close enough in proximity to have their atomic orbitals overlap appreciably. Since the  $\psi_n$  are actually orthogonalized Lowdin functions

containing contributions from the orbitals of nearby atoms, the integrals will be appreciable for greater interatomic distances than if the integrals were formed directly from the atomic orbitals. All the same, the integrals will decrease fairly rapidly as the distance between atoms decreases (Ref 52:1501-1502).

The symmetry properties of the crystal suggest that the integrals in Equation (84) are related (Ref 52:1502). For example, symmetric rotation and inversion operations about an atom at  $\bar{R}_i$ , where the orbital  $\psi_n$  is located, will carry the atom at  $\bar{R}_j$  into another similar atom into the same unit cell or another unit cell. The relations between integrals involving orbitals  $\psi_n$  and  $\psi_m$  on various atoms will be all the same at equal distances from the first atom. Noting this, the number of independent integrals decreases and in some cases the finite number of disposable constants remaining are nearly the right amount needed to fit the results of accurate calculations at the symmetry points in the Brillouin zone which have already been made. Using these symmetry properties results in simple formulas for the matrix components of energy (Ref 42).

A second simplification is made by considering only the atomic orbitals whose energy is somewhere near the energy of the energy bands of interest (Ref 52:1502). For example, when considering the valence and conduction bands of diamond, for an element in the 3d transition group, one can consider the 3d, 4s, and 4p atomic orbitals and disregard the others. Using only a few atomic orbitals reduces the order of the secular equation to one that can be handled more easily. In diamond, there are eight orbitals: the 2s orbital and the threefold degenerate 2p orbitals for each of the two atoms in the unit cell, which produces an eighth-order secular equation.

The third simplification is called the two-center approximation (Ref 52:1502-1504). Three-center integrals are smaller than two-center integrals and in some cases the former can be disregarded thus simplifying the equation even further. When the potential energy in the Hamiltonian is written as the sum of spherical potentials located on the various atoms, the three-center integrals can be neglected. Part of the potential energy remains which represents the sum of spherical potentials located on the two atoms on which the atomic orbitals are located, analogous to the case of a diatomic molecule. Let  $\bar{R}_j - \bar{R}_i$  represent the vector from one atom to another, i.e. the axis. The functions  $\psi$  can be expanded as linear combinations of the components of angular momentum around the axis:  $\sigma$ ,  $\pi$ , and  $\delta$ . Although the  $\psi$ 's are Lowdin orthogonalized functions and not atomic orbitals, they have the same symmetry properties with respect to the crystal so the expansion is still a good approximation. Each integral can be symbolized by  $E_{x,xy}(1,m,n)$ , for example, where 1,m and n denote the direction cosines of the  $\bar{R}_j - \bar{R}_i$  vector (Ref 52:1503). The first subscript x,y, or z refers to the  $p_x$ ,  $p_y$ , or  $p_z$  functions, respectively. The second subscript refers to the various d functions; these subscripts stand for the functions whose dependence on angle is of the form xy, yz, xz,  $x^2 - y^2$ , or  $3z^2 - r^2$  multiplied by the appropriate function of r. The energy integral represents an integral in which the function  $\psi_n$  is a  $p$ -like function, and  $\psi_m$  is a d function with symmetry properties like xy.  $E_{x,xy}(1,m,n)$  is a function which can be written in terms of two integrals: the first is between a  $p\sigma$  orbital on the first atom and a  $d\sigma$  orbital on the second, symbolized by  $(pd\sigma)$ ; and the second is between a  $p\pi$  orbital on the first atom and a  $d\pi$  orbital on the

TABLE II

Energy integrals for a crystal in terms of two center integrals

$E_{s,s}$	$(ss\sigma)$
$E_{s,p}$	$l(sp\sigma)$
$E_{s,p}$	$P(pp\sigma) + (1-P)(pp\pi)$
$E_{s,p}$	$lm(pp\sigma) - lm(pp\pi)$
$E_{s,p}$	$ln(pp\sigma) - ln(pp\pi)$
$E_{s,sp}$	$\sqrt{3}lm(sd\sigma)$
$E_{s,s^2-p^2}$	$\frac{1}{2}\sqrt{3}(P^2 - m^2)(sd\sigma)$
$E_{s,s^2-p^2}$	$[n^2 - \frac{1}{2}(P^2 + m^2)](sd\sigma)$
$E_{s,sp}$	$\sqrt{3}Pm(pd\sigma) + m(1 - 2P^2)(pd\pi)$
$E_{s,sp}$	$\sqrt{3}lmn(pd\sigma) - 2lmn(pd\pi)$
$E_{s,sp}$	$\sqrt{3}Pn(pd\sigma) + n(1 - 2P^2)(pd\pi)$
$E_{s,s^2-p^2}$	$\frac{1}{2}\sqrt{3}l(P^2 - m^2)(pd\sigma) + l(1 - P^2 + m^2)(pd\pi)$
$E_{p,s^2-p^2}$	$\frac{1}{2}\sqrt{3}m(P^2 - m^2)(pd\sigma) - m(1 + P^2 - m^2)(pd\pi)$
$E_{s,s^2-p^2}$	$\frac{1}{2}\sqrt{3}n(P^2 - m^2)(pd\sigma) - n(P^2 - m^2)(pd\pi)$
$E_{s,s^2-p^2}$	$l[n^2 - \frac{1}{2}(P^2 + m^2)](pd\sigma) - \sqrt{3}ln^2(pd\pi)$
$E_{p,s^2-p^2}$	$m[n^2 - \frac{1}{2}(P^2 + m^2)](pd\sigma) - \sqrt{3}mn^2(pd\pi)$
$E_{s,s^2-p^2}$	$n[n^2 - \frac{1}{2}(P^2 + m^2)](pd\sigma) + \sqrt{3}n(P^2 + m^2)(pd\pi)$
$E_{sp,sp}$	$3P^2m^2(dd\sigma) + (P^2 + m^2 - 4Pm^2)(dd\pi) + (n^2 + P^2m^2)(dd\delta)$
$E_{sp,sp}$	$3lm^2n(dd\sigma) + ln(1 - 4m^2)(dd\pi) + ln(m^2 - 1)(dd\delta)$
$E_{sp,sp}$	$3P^2mn(dd\sigma) + mn(1 - 4P^2)(dd\pi) + mn(P^2 - 1)(dd\delta)$
$E_{sp,s^2-p^2}$	$\frac{1}{2}lm(P^2 - m^2)(dd\sigma) + 2lm(m^2 - P^2)(dd\pi) + \frac{1}{2}lm(P^2 - m^2)(dd\delta)$
$E_{p,s^2-p^2}$	$\frac{1}{2}mn(P^2 - m^2)(dd\sigma) - mn[1 + 2(P^2 - m^2)](dd\pi) + mn[1 + \frac{1}{2}(P^2 - m^2)](dd\delta)$
$E_{s,s^2-p^2}$	$\frac{1}{2}nl(P^2 - m^2)(dd\sigma) + nl[1 - 2(P^2 - m^2)](dd\pi) - nl[1 - \frac{1}{2}(P^2 - m^2)](dd\delta)$
$E_{sp,s^2-p^2}$	$\sqrt{3}lm[n^2 - \frac{1}{2}(P^2 + m^2)](dd\sigma) - 2\sqrt{3}lmn^2(dd\pi) + \frac{1}{2}\sqrt{3}lm(1 + n^2)(dd\delta)$
$E_{p,s^2-p^2}$	$\sqrt{3}mn[n^2 - \frac{1}{2}(P^2 + m^2)](dd\sigma) + \sqrt{3}mn(P^2 + m^2 - n^2)(dd\pi) - \frac{1}{2}\sqrt{3}mn(P^2 + m^2)(dd\delta)$
$E_{s,s^2-p^2}$	$\sqrt{3}ln[n^2 - \frac{1}{2}(P^2 + m^2)](dd\sigma) + \sqrt{3}ln(P^2 + m^2 - n^2)(dd\pi) - \frac{1}{2}\sqrt{3}ln(P^2 + m^2)(dd\delta)$
$E_{s^2-p^2,s^2-p^2}$	$\frac{1}{2}(P^2 - m^2)^2(dd\sigma) + [P^2 + m^2 - (P^2 - m^2)^2](dd\pi) + [n^2 + \frac{1}{2}(P^2 - m^2)^2](dd\delta)$
$E_{s^2-p^2,s^2-p^2}$	$\frac{1}{2}\sqrt{3}(P^2 - m^2)[n^2 - \frac{1}{2}(P^2 + m^2)](dd\sigma) + \sqrt{3}n^2(m^2 - P^2)(dd\pi) + \frac{1}{2}\sqrt{3}(1 + n^2)(P^2 - m^2)(dd\delta)$
$E_{s^2-p^2,s^2-p^2}$	$[n^2 - \frac{1}{2}(P^2 + m^2)]^2(dd\sigma) + 3n^2(P^2 + m^2)(dd\pi) + \frac{1}{2}(P^2 + m^2)^2(dd\delta)$

(Ref 52:1503).

second atom, symbolized by  $(pd\pi)$ . The first index refers to the first orbital and similarly for the second. The energy integral was determined by the product of the three integrals outlined earlier. Formulas for the energy integrals for all the combinations of the s, p, and d functions are given in Table II (Ref 52:1503). By using Table II, the various energy integrals E can be approximated in terms of a smaller number of

integrals which is a good approximation in some cases (Ref 52:1504). The table is also very useful in making comparisons with other existing calculation which automatically assume two-center integrals.

Applying the LCAO to the Diamond Structure (Ref 52:1516-1522). The diamond structure can be described as a face-centered cubic structure having two atoms in the unit cell rather than one. One atom is located at  $p\bar{a}_i + q\bar{a}_j + r\bar{a}_k$ , site 1, and the other atoms are displaced by  $\frac{1}{2} a(\bar{i}+\bar{j}+\bar{k})$ , called site 2, where  $p$ ,  $q$ , and  $r$  are integers,  $p+q+r$  is an even integer, and  $a$  is the lattice constant. Eight Bloch sums are obtained by setting up Bloch functions of  $s$ ,  $p_x$ ,  $p_y$ ,  $p_z$  orbitals on each of the two types of atomic sites. The matrix components of energy obtained by means of the Bloch sums are denoted by symbols such as  $(s/x)_{12}$ . This represents a matrix component between an  $s$ -orbital Bloch function on site 1 and a  $p_x$  Bloch function on site 2. There are four nearest neighbors of an atom in the diamond structure as shown in Figure 21 (Ref 35:9). If the atom under consideration is at the origin, its neighbors are located at the positions  $a(\frac{1}{2} \frac{1}{2} \frac{1}{2})$ ,  $a(-\frac{1}{2} -\frac{1}{2} -\frac{1}{2})$ ,  $a(-\frac{1}{2} \frac{1}{2} -\frac{1}{2})$ , and  $a(-\frac{1}{2} -\frac{1}{2} \frac{1}{2})$ . The second nearest neighbors are the type denoted by  $a(110)$ . The resulting matrix components are given in Table III (Ref 52:1517) where  $\xi$ ,  $\eta$ , and  $\zeta$  denote the symmetry symbols for the diamond structure and the energy integrals (Ref 52:1517) are given by

$$\begin{aligned}
 E_{s,s}(\frac{1}{2}\frac{1}{2}\frac{1}{2}) &= (ss\sigma)_1, \\
 E_{x,x}(\frac{1}{2}\frac{1}{2}\frac{1}{2}) &= \frac{1}{3}(pp\sigma)_1 + \frac{2}{3}(pp\pi)_1, \\
 E_{x,y}(\frac{1}{2}\frac{1}{2}\frac{1}{2}) &= \frac{1}{3}(pp\sigma)_1 - \frac{1}{3}(pp\pi)_1, \\
 E_{x,s}(\frac{1}{2}\frac{1}{2}\frac{1}{2}) &= 3^{-1}(sp\sigma)_1, \\
 E_{s,s}(110) &= (ss\sigma)_2, \\
 E_{x,x}(011) &= (pp\pi)_2, \\
 E_{x,y}(110) &= \frac{1}{3}(pp\sigma)_2 - \frac{1}{3}(pp\pi)_2, \\
 E_{x,s}(110) &= \frac{1}{3}(pp\sigma)_2 + \frac{1}{3}(pp\pi)_2, \\
 E_{x,s}(110) &= 2^{-1}(sp\sigma)_2, \\
 E_{x,x}(011) &= E_{x,y}(011) = 0.
 \end{aligned}
 \tag{86}$$

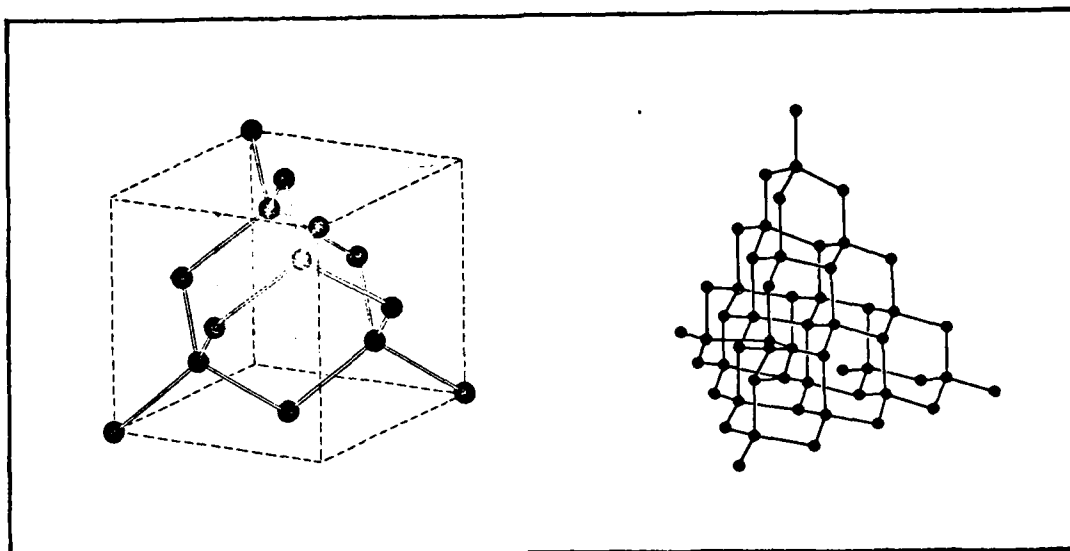


Fig 21. The diamond lattice (Ref 29:28; 35:9).

The resulting Hamiltonian matrix is real and symmetric, and has the following components (Ref 52:1517):

$$\begin{array}{ll}
 (s/s)_{11} = (s/s)_{22} & E_{s,s}(000) + 4E_{s,s}(110)(\cos\xi \cos\eta + \cos\eta \cos\xi + \cos\xi \cos\xi) \\
 (x/x)_{11} = (x/x)_{22} & E_{x,x}(000) + 4E_{x,x}(110)(\cos\xi \cos\eta + \cos\xi \cos\xi) + 4E_{x,x}(011) \cos\eta \cos\xi \\
 (s/s)_{12} = (s/s)_{21}^* & 4E_{s,s}(\frac{1}{2}\frac{1}{2}) (\cos\frac{1}{2}\xi \cos\frac{1}{2}\eta \cos\frac{1}{2}\xi - i \sin\frac{1}{2}\xi \sin\frac{1}{2}\eta \sin\frac{1}{2}\xi) \\
 (s/x)_{12} = -(s/x)_{21}^* & 4E_{s,x}(\frac{1}{2}\frac{1}{2}) (i \sin\frac{1}{2}\xi \cos\frac{1}{2}\eta \cos\frac{1}{2}\xi - \cos\frac{1}{2}\xi \sin\frac{1}{2}\eta \sin\frac{1}{2}\xi) \\
 (s/x)_{11} = -(s/x)_{22}^* & -4E_{s,x}(011) \sin\xi \sin\eta + 4iE_{s,x}(110) (\sin\xi \cos\eta + \sin\xi \cos\xi) \\
 (x/x)_{12} = (x/x)_{21}^* & 4E_{x,x}(\frac{1}{2}\frac{1}{2}) (\cos\frac{1}{2}\xi \cos\frac{1}{2}\eta \cos\frac{1}{2}\xi - i \sin\frac{1}{2}\xi \sin\frac{1}{2}\eta \sin\frac{1}{2}\xi) \\
 (x/y)_{12} = (x/y)_{21}^* = (y/x)_{12} & 4E_{x,y}(\frac{1}{2}\frac{1}{2}) (i \cos\frac{1}{2}\xi \cos\frac{1}{2}\eta \sin\frac{1}{2}\xi - \sin\frac{1}{2}\xi \sin\frac{1}{2}\eta \cos\frac{1}{2}\xi) \\
 (x/y)_{11} = (x/y)_{22}^* & -4E_{x,y}(110) \sin\xi \sin\eta - 4iE_{x,y}(011) (\sin\xi \cos\xi - \sin\eta \cos\xi)
 \end{array} \tag{87}$$

This can be reduced to a 2x2 matrix whose determinant

$$\begin{vmatrix} H_{11} + H_{13} - E & H_{12} + H_{14} \\ H_{12} + H_{14} & H_{22} + H_{24} - E \end{vmatrix} = 0 \tag{88}$$

assuming  $\Delta$  symmetry (Ref 52:1517).

For the (100) and (111) directions, the equation predicts a number of levels and their degeneracy, and the symmetry at the edges of the Brillouin zone. Some values of the energy integrals vanish as a result of the two-center approximation but the same type of integrals can be chosen to approximate known results. Much use has been made of the diamond structure, partly due to Herman's results using the OPW method (Ref 24; 25) and the comparison with the results of the LCAO method. The general agreement comes from the minimal contributions of the second-nearest neighbors compared to those of the nearest neighbors. The OPW method was applied to diamond by Herman (Re 24), to Ge by Herman and Callaway (Ref 8:74-78; 23), and to Si by Woodruf and Bassani (Ref 8:70-74). The results are shown in Figures 22 and 23.

Suggestions for Applying the LCAO Method to the Ge-Si Crystal.

There are many things to consider in applying the LCAO method to the Ge-Si alloy of interest. The alloy is not a pure crystal by definition. In addition to the binary property of the alloy, the microscopically nonuniform distribution of each element does not facilitate easy application of the LCAO method. Assuming the lattice retains its crystal proerties at 10% Si and 90% Ge, the uneven nature of the composition suggests very complicated Bloch sums and thus very complicated wavefunctions  $\psi_n$ . The binary alloy keeps its diamond crystal structure but a difficulty arrises in representing a 10% Si and 90% Ge alloy in a tetrahedral unit cell.

A recommended approach is to take the statistical average of the results of several applications of the LCAO method to a crystal which may

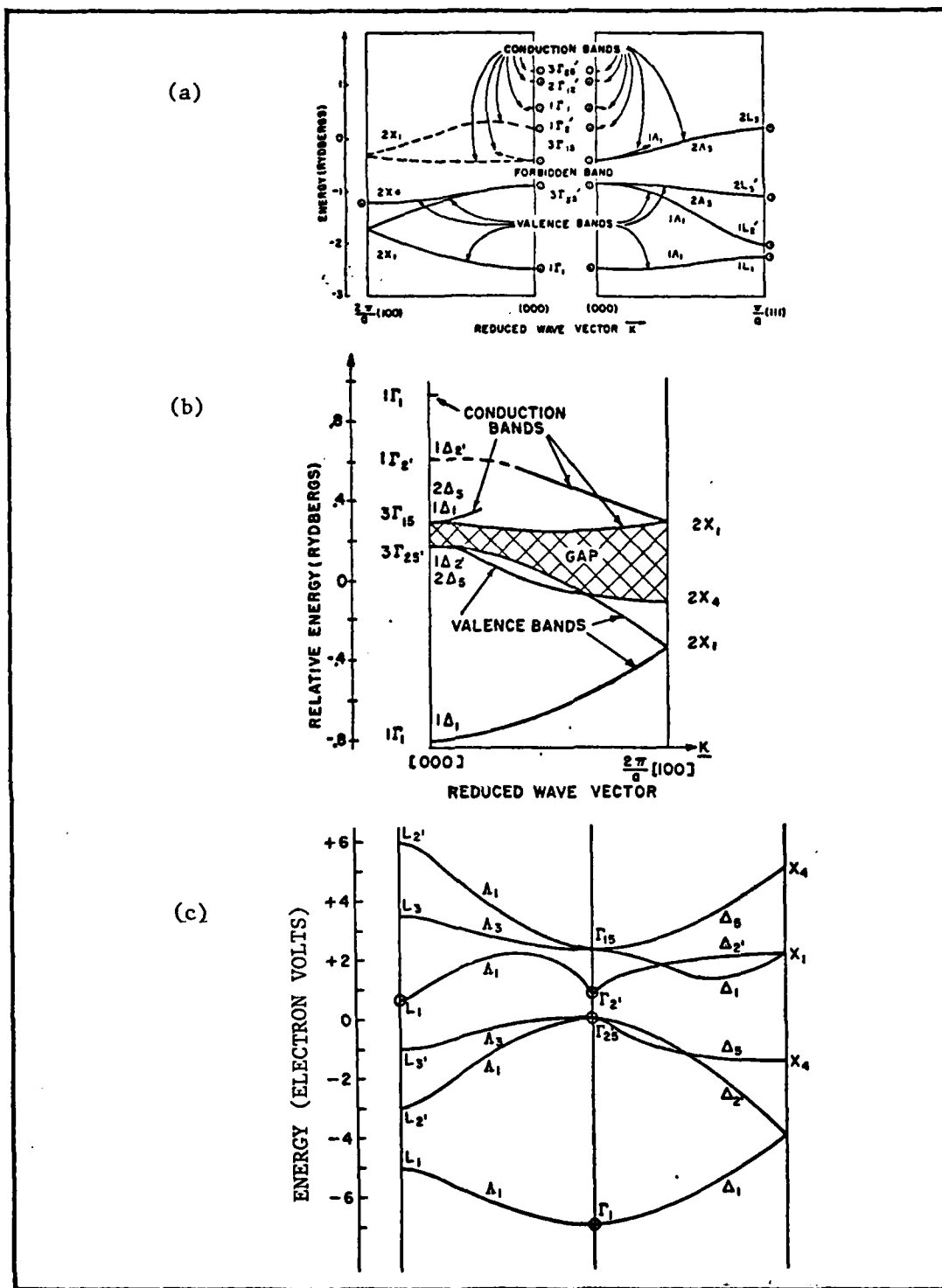


Fig 22. a) The energy bands of a diamond crystal in the 100 and 111 directions (Ref 24),  
 b) the energy band structure of a Ge crystal (Ref 25),  
 c) the energy bands of Ge along the 100 and 111 axes (Ref 8:76).

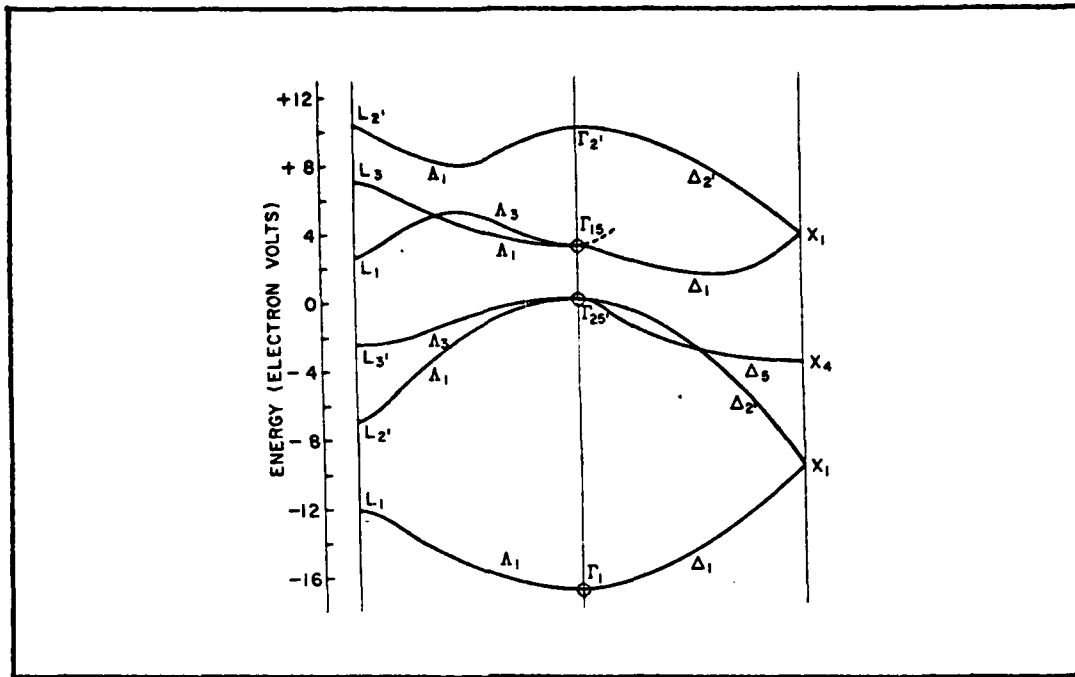


Fig 23. The energy bands of Si along the 100 and 111 directions (Ref 8:72).

be 10% Si over its total volume but not over the volume of the unit cell. The LCAO method involves linear combinations of Bloch sums between atomic orbitals of atoms even though the atoms under consideration may not be the same. Assume also that the periodic potential remains periodic after the substitutional addition of Si in the Ge crystal is 10% Si and 90% Ge, the distribution is a uniform as possible, and the location of the Si atoms are periodic when moving from one unit cell to another ( a reasonable assumption for crystals grown by epitaxy), then the LCAO method can be applied to each unit cell, producing an energy band structure for each cell in the volume.

It is obvious that a single unit cell cannot have a 10% composition of Si because whole atoms must be preserved. The binary alloy, then, is

really made up of unit cells which may have zero, one, two, or more Si atoms mixed with the Ge atoms of the unit cell so that the concentration over the volume of the crystal will have 10% Si - 90% Ge. When the LCAO method is applied to a unit cell having no Si atoms, the resulting energy band structure, which has already been calculated by Herman and Slater and Koster (Ref 25; 52), will be that of Ge as shown in Figure 22. When the LCAO method is applied to unit cells having one Si atom, the resulting energy band structure will closely resemble that of Ge with slight modifications of the Si (100) and Ge (100) conduction band curves (Ref 5; 8:76; 27). Similar applications of the LCAO method would have to be done for all the unit cells of the crystal or a representative subgroup. A weighted average of the resulting energy band structures should produce an energy band structure which describes the macroscopic behavior of holes and electrons in the Ge-Si alloy.

It would be helpful in evaluating the constants arising in the LCAO results to have some idea of the energy band structure along the symmetry lines of the crystal. This information can be obtained from the results of optical and cyclotron resonance experiments (Ref 35:290-307; 29:318-322; 59) as in the results of Johnson and Christian for a 0-199% range of Si in Ge (Ref 27). The absorption properties of the alloy have been studied by Braunstein, Moore, and Herman (Ref 5) for the same compositions of Si and Ge. At about 15% Si the energy band structure changes from a Si-like (100) to a Ge-like (100) conduction band structure which is the crucial point of interest for the subject of this thesis.

While work progresses in the area of the crystal growth of the Ge-Si alloy, the predicted results of the quantum mechanical analysis of the binary alloy forms the basis for the decision to treat the photodetector alloy as pure Ge with regard to its chemical and material properties which come into play during the fabrication process. The following chapter describes the fabrication procedure for the five Ge photodiodes discussed in the thesis.

#### IV Device Fabrication and Testing

The five Ge photodiode samples which were analyzed in this thesis research are described in this section in terms of device fabrication. The process for each sample can be found in Table III. The three samples that were implanted are G-7-1, G-7-4, and G-8-1. The diffused samples, D-6-1 and D-6-3, were separate diodes from the same wafer. The starting material for all samples was  $3 \Omega\text{-cm}$ , p-type Ge wafers three inches in diameter.

The implanted diodes were processed as 130 x 135 mil/square chips which underwent processing mounted in an implant holder shown in Figure 24. The holder was capable of processing four chips each containing four diodes in a square matrix. The 30-mil implant mask is also shown in Figure 24 next to the 3-mil contact mask fitted inside the implant holder.

In the case of implanted samples, the individual chips were sputtered with  $\text{Si}_3\text{N}_4$  for five minutes. This 1000 Å, very thin film provided a protective film on the surface of the chip during the following implant step. Residual hydrocarbons from the vacuum system of the accelerator can be polymerized on the chip surface by ion implantation; this is analogous to hitting photoresist. The polymerized hydrocarbons can interfere with the implantation and are also very hard to remove. The As implants were performed as listed in the process schedule of Table III, followed by thermal annealing.

Front contacts of Ni/Au/Ge were evaporated on the chips using a

TABLE III

Implanted Samples	Protective Film	Implant	Anneal	Front Contacts	Back Contacts	Mesa	Bonding
G-7-1 #9	Sputter 5 min Si <sub>3</sub> N <sub>4</sub>	2x10 <sup>14</sup> cm <sup>-2</sup> <sup>14</sup> As 200 KeV	750°C 30 min in H <sub>2</sub>	Evaporate Ni/Au/Ge 3 mil lift-off mask	Au/Mg	planar	Ultrasonic room temp.
G-7-4 #23	Sputter 5 min Si <sub>3</sub> N <sub>4</sub>	2x10 <sup>14</sup> cm <sup>-2</sup> <sup>14</sup> As 200 KeV	750°C 1 hour in H <sub>2</sub>	Evaporate Ni/Au/Ge 3 mil lift-off	Ni/Au/Mg	H <sub>2</sub> O <sub>2</sub> etch 43 min dots of black wax	Ultrasonic room temp.
G-8-1 #23	Sputter 5 min Si <sub>3</sub> N <sub>4</sub>	1x10 <sup>14</sup> cm <sup>-2</sup> <sup>14</sup> As 200 KeV	700°C 30 min in H <sub>2</sub>	Evaporate Ni/Au/Ge 3 mil lift-off mask	Au/Mg	planar	Ultrasonic 280°C
Diffused Samples	Diffusion	x <sub>1</sub>		Front Contacts	Back Contacts	Mesa	Bonding
D-6-1 #6 and D-6-3 #6	775°C 60 min Phosphene	~1.2 μm	2.25 μsec	Ni/Au/Ge lift-off	used silver paint	H <sub>2</sub> O <sub>2</sub> etch 40 min 20mil mask	Ultrasonic room

3-mil lift-off mask to define the contact pattern. The procedure was as follows. A mask containing an array of 3-mil holes, as shown in the implant holder of Figure 24, was used to cut holes in the photoresist as shown in Figure 25(a). A commercial buffered HF etch was used to remove the  $\text{Si}_3\text{N}_4$  inside the 3 mil holes in Figure 25(b). After the  $\text{Si}_3\text{N}_4$  was lifted off the wafer inside the 3 mil holes, 1000-1200 Å of Ni/Au/Ge metallization was evaporated on the wafer as shown in Figure 25(c). The thick photoresist (AZ) layer enabled a discontinuity to form between the metal that forms the contact and the metal deposited on top of the photoresist. The discontinuity allowed the latter to be lifted off at the same time the photoresist was removed with acetone. The remaining structure is shown in Figure 25(d) with a final metallization thickness of 1000-1200 Å.

After back contacts were evaporated on the chips, two samples, G-7-1 and G-8-1, were left planar and G-7-4 was mesa etched. Dots of black wax were placed by hand over the contacts of a sample and part of implanted region as shown in Figure 26(a). The sample was then mounted on a glass slide and placed in a peroxide etch (1  $\text{H}_2\text{O}_2$  : 5 DI- $\text{H}_2\text{O}$ ) for 43 minutes. The peroxide etches at a rate of 0.0275  $\mu\text{m}$  per minute (Ref 46:88-91). A rinse in acetone following the etch removed the wax leaving a mesa structure as shown in Figure 26(b). Obviously, diode area by this means was not well controlled. The result of the imprecision will be discussed in Chapter VII.

A number of diodes were probed using the set-up in Figure 27 where the probes were connected to a conventional curve-tracer. Chips containing working diodes were mounted on a 28-pin DIP package. Ultrasonic bonding

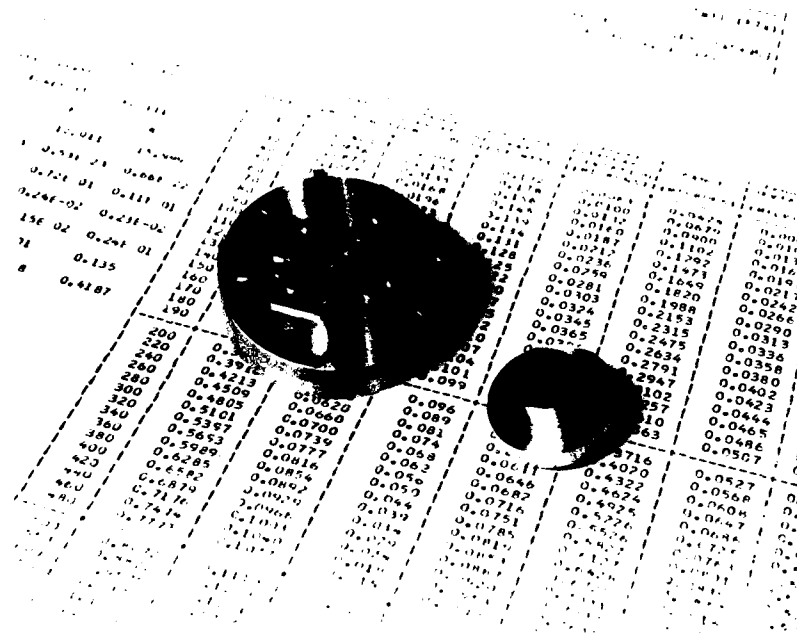


Fig 24. Implant holder and mask used for processing four chips of four diodes each.

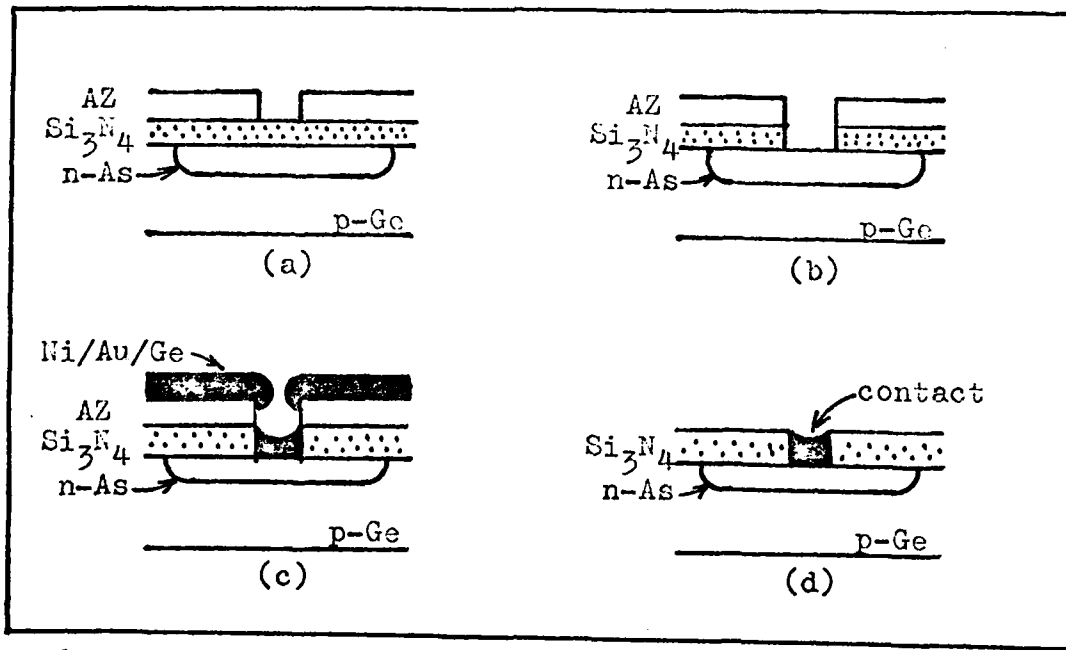


Fig 25. The 3-mil lift-off process.

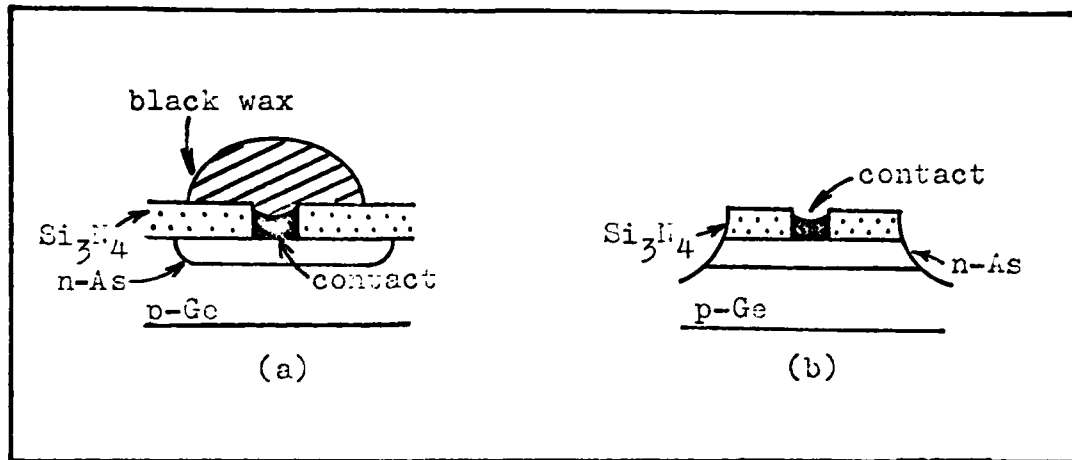


Fig 26. Mesa etching using dots of black wax over the diode area.

at room temperature damaged some samples which explains the difference in the bonding of sample G-8-1. One problem with the shallow junction is that the "shallowness" is very sensitive to the pressure placed on it by bonding wires and bonding procedures themselves. Some samples that displayed excellent I-V curves prior to bonding were unfortunately lost as a result of being shorted by ultrasonic bonding. By heating the package to 280°C, it was possible to lower the power and time settings for ultrasonic bonding. For the four-diode chips, bonds were made from the contacts to pins #6, 9, 20, and 23. A ground wire was also bonded from the substrate to pin #15. See Figure 28.

The diffused samples D-6-1 and D-6-3 originated from the same 3 inch wafer. The 3 Ω-cm p-type Ge wafer experienced diffusion of phosphorus from a phosphene ambient for 60 minutes at 775°C. Front contacts were evaporated and patterned using a conventional mask consisting of an array of 3-mil holes. The lift-off process described in Figure 25 was used here also. Back contacts were omitted in favor of mounting chips on the DIP using silver paint because of difficulties with the vacuum system in



Fig 27. The diodes are tested using probes which lead to a conventional curve tracer.

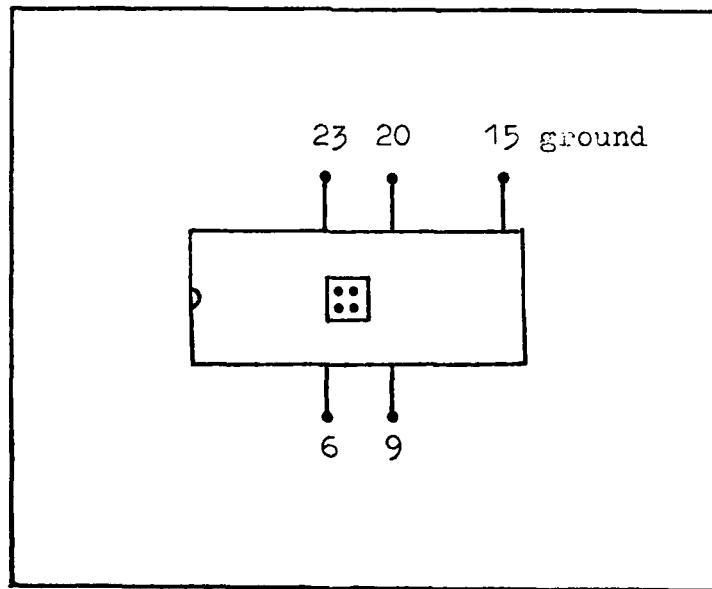


Fig 28. Diagram showing pin connections for a 4-diode chip.

the evaporator. A mask containing an array of 20-mil holes was aligned with the 3-mil contacts to pattern the photoresist for mesa etching. The remaining structure was similar to that shown in Figure 26. After scribing, only one diode was contained in each chip. Bonding wires were connected to pins 6 and 15 for the contact and ground respectively. A close-up view of a single diode is shown in Figure 29. It shows the center contact, the bonding wire, and the perimeter of the diode defined by the mesa etch.

The diffusion process followed the same sequence as the implantation schedule except that the diffused diodes were processed as complete wafers and the P impurity atoms for the n<sup>+</sup> region were supplied by the phosphene ambient in the diffusion furnace. In contrast to the implanted samples, mesa etching was required in the diffused samples to define the perimeter of the area of the diode. The mesa etch was done using photoresist and masking steps instead of the dots of black wax described earlier. Packaging and testing of the diffused samples was the same as for the implanted samples.

Table III summarizes the device fabrication steps of the implanted and diffused Ge photodiodes. The finished samples were probed and packaged, then tested again for reassurance that workable diodes still existed after bonding. It should be noted that the performance of some of the Ge photodetectors as diodes degraded somewhat after bonding. The next step was to test the performance of the Ge photodetectors for their optical characteristics, namely photoresponse. This requires a discussion of the photometric system used to test the detectors which follows in the next chapter.

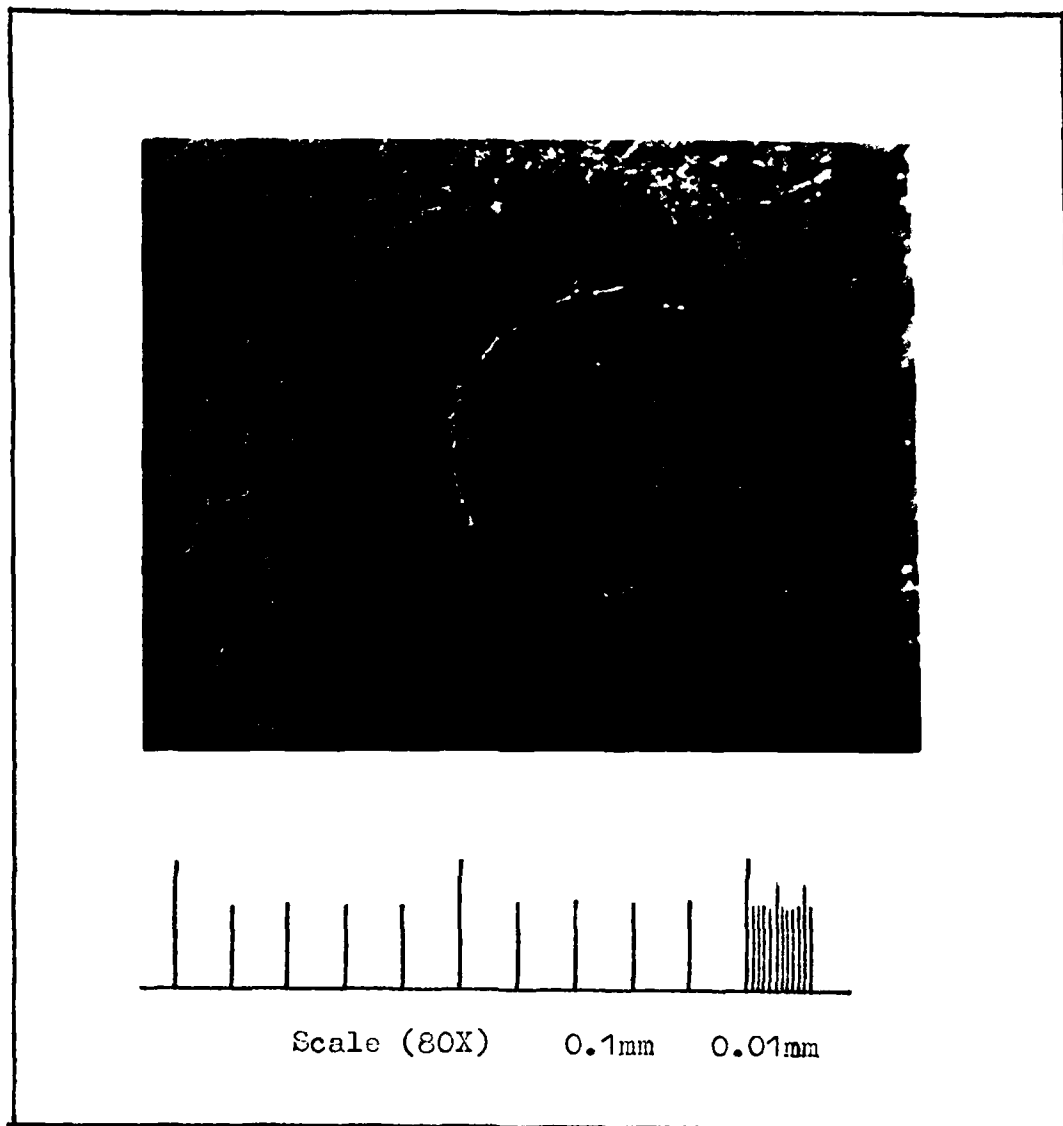


Fig 29. Typical diode structure showing center contact, bonding wire, and perimeter of the diode with measuring scale.

## V Experimental Procedure and Equipment

### Photometric System

The photometric system used to test the photoresponse of the samples is shown in block diagram form in Figure 30 (Ref 6:3). It requires basically four components: source, detector, amplifier, and recorder. The source emits optical radiation over a wide range of wavelengths, which is incident on the photodetector. The photodetector does not respond over the same wide spectrum of wavelengths emitted by the light source. In the smaller range of wavelength over which it does respond, incident light generates enough electron-hole pairs to produce a very weak signal. The weak output signal is amplified to appropriate levels for signal processing and is recorded.

Weak Signals Buried in Noise. There are various noise limitations associated with the detection of optical radiation. The main problem is that the electrical signal is so weak it is usually buried in noise. One requirement to obtain meaningful measurements is to reduce the system noise to that of the detector or the source. The detector must have at least three times the noise resistance of the amplifier (Ref 6:10). A comparison of three systems is made in Reference 6 and the synchronous detection scheme described in Appendix A (Ref 6; 26; 45; 50) is preferred over the DC and conventional AC systems. The preference can be attributed to minimized noise problems.

Equipment. In terms of the block diagram of the photometric system shown in Figure 30, the radiant source takes the form of a globar. The globar is a water-cooled, silicon carbide light source whose spectral

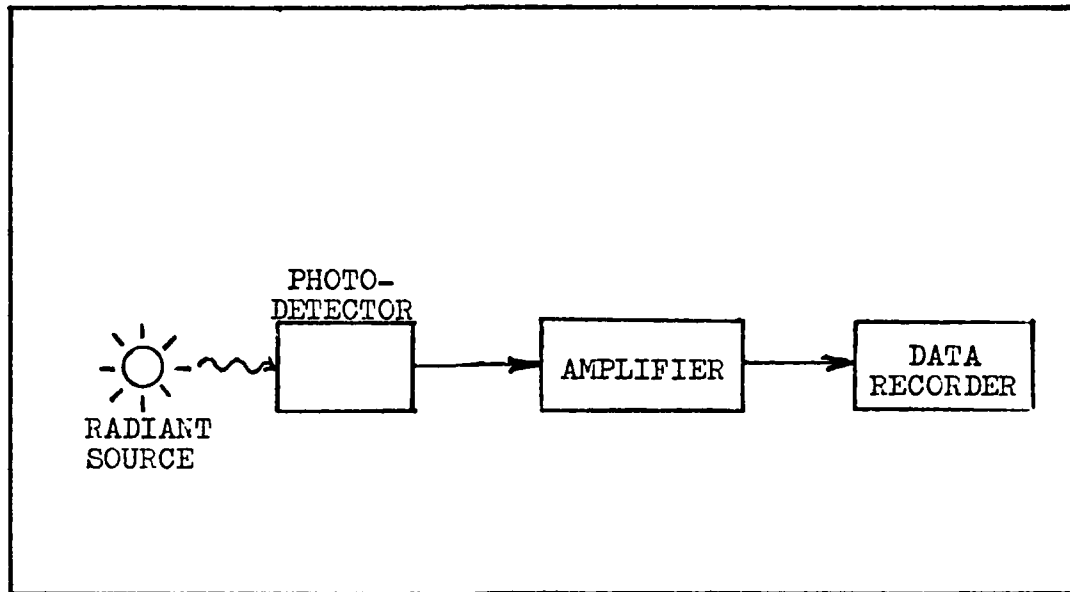


Fig 30. The block diagram of a photometric system (Ref 6:3).

characteristics have been calibrated and measured for operation at 230 watts of global power. The characteristics are listed in Table IV by drum number, the corresponding wavelength  $\lambda$  ( $\mu\text{m}$ ), energy  $E$  (eV), and global power per unit area  $H$  ( $\mu\text{W}/\text{cm}^2$ ). The drum number comes from the monochromator used to manually tune the desired wavelength or scan the spectrum of the global light source.

Erratic behavior on the part of the global light source prompted the run of a second set of calibration data. The first set of data was taken on May 30, 1979. During the course of the thesis work, the global was stable. Instability in the operation of the global near the end of the thesis quarter required the recalibration on September 28, 1979; the unstable behavior was due to contact problems. The second set of calibration data tended to flatten the output power spectrum of the global in a nonlinear fashion as can be seen by the  $\Delta H$  column of Table IV.

TABLE IV  
Calibration Data

Drum Number	E (eV)	$\lambda$ ( $\mu\text{m}$ )	H* ( $\mu\text{W}/\text{cm}^2$ )	H** ( $\mu\text{W}/\text{cm}^2$ )	$\Delta\text{H}$ ( $\mu\text{W}/\text{cm}^2$ )
1580	1.19	1.04	28	22	6
1570	1.11	1.11	140	142	2
1560	1.04	1.19	307	306	1
1550	0.973	1.28	432	437	5
1540	0.908	1.37	523	516	7
1530	0.852	1.46	643	623	20
1520	0.800	1.55	721	695	26
1510	0.752	1.65	766	730	36
1500	0.710	1.75	777	742	35
1490	0.672	1.85	750	713	43
1470	0.611	2.03	768	728	50

\* Calibration data taken 30 May 1979.

\*\* Calibration data taken 28 September 1979.

The monochromator is a Model 098 (Serial No. 297) from the Perkin-Elmer Corporation in Norwalk, Ct. It is a single pass, basic prism monochromator designed for use in the infrared region but can be used with other prisms to change the wavelength region or vary the amount of dispersion. Wavelength is scanned manually by rotating a drum which adjusts the internal optics of the monochromator to vary the wavelength. A schematic diagram of a monochromator is given in Figure 31.

Figure 32 shows the experimental set-up for the photometric system. The tall cylindrical shaft is the vacuum chamber, the top of which holds

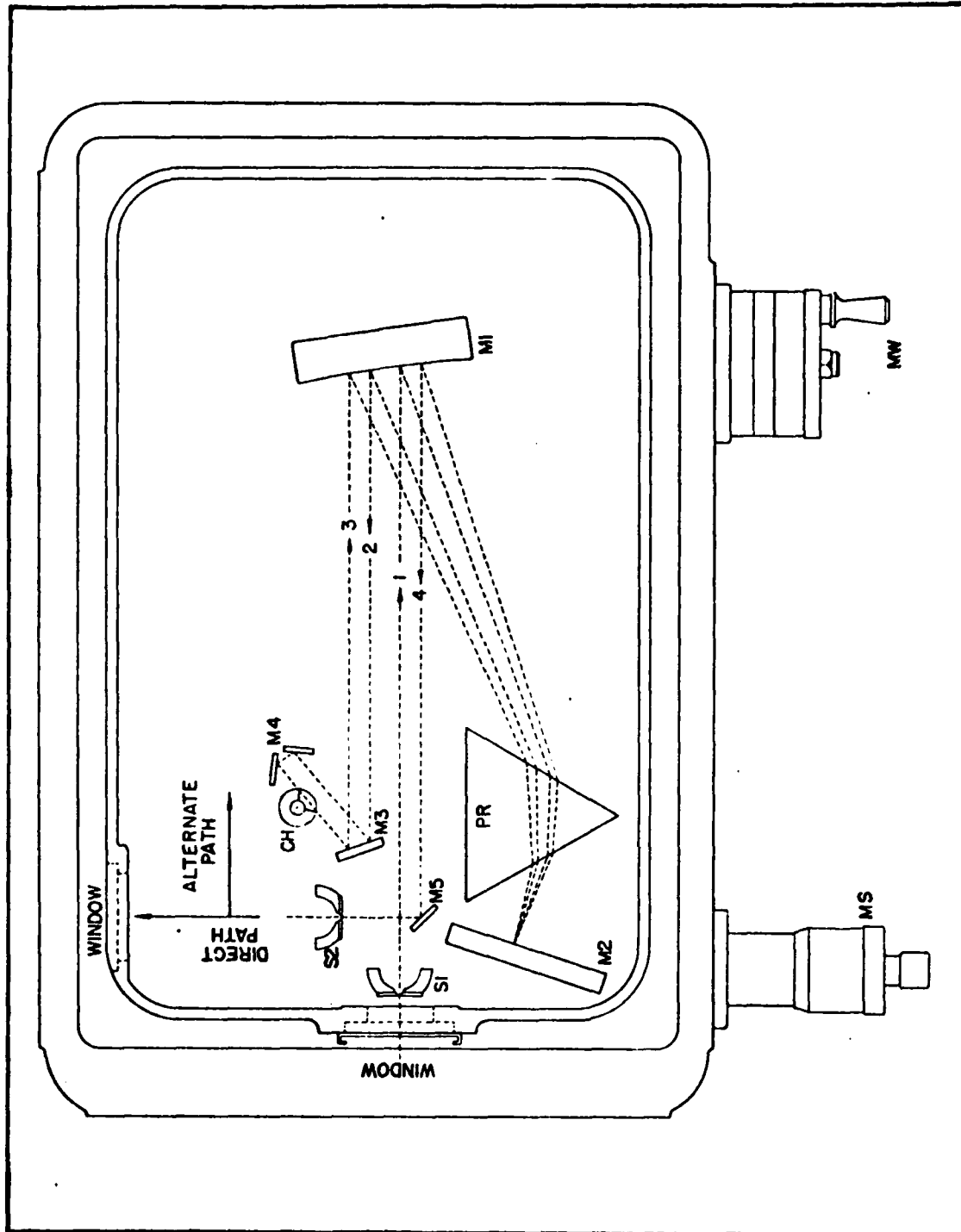


Fig 31. Schematic optical path of a monochromator (Ref 39).

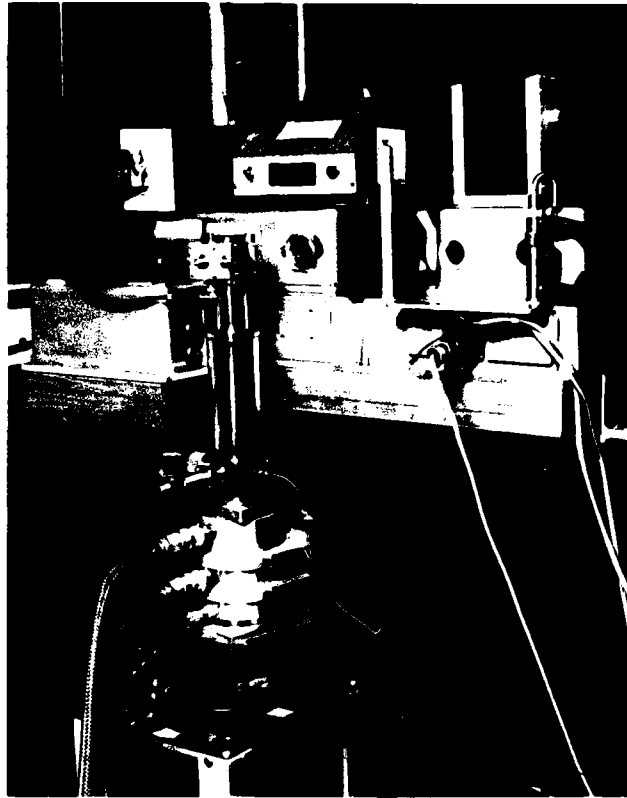


Fig 32. The experimental set-up for the photometric system.

the DIP package on which the photodiode chip is mounted. Refer to the diagram in Figure 33. The diode is clamped to the header and the cylinder slides over the header making a seal for pumping down the chamber. The vacuum gauge at the top center of the photo in Figure 32 monitors the vacuum pressure inside the chamber. Coaxial cables from the photodetector lead to a preamplifier and to the rack of instruments shown in Figure 34. The instruments are listed in Table V and their uses will be demonstrated in the following paragraph.

System operation can be summarized as follows. The monochromator selects a wavelength provided by the globar and emits the infrared

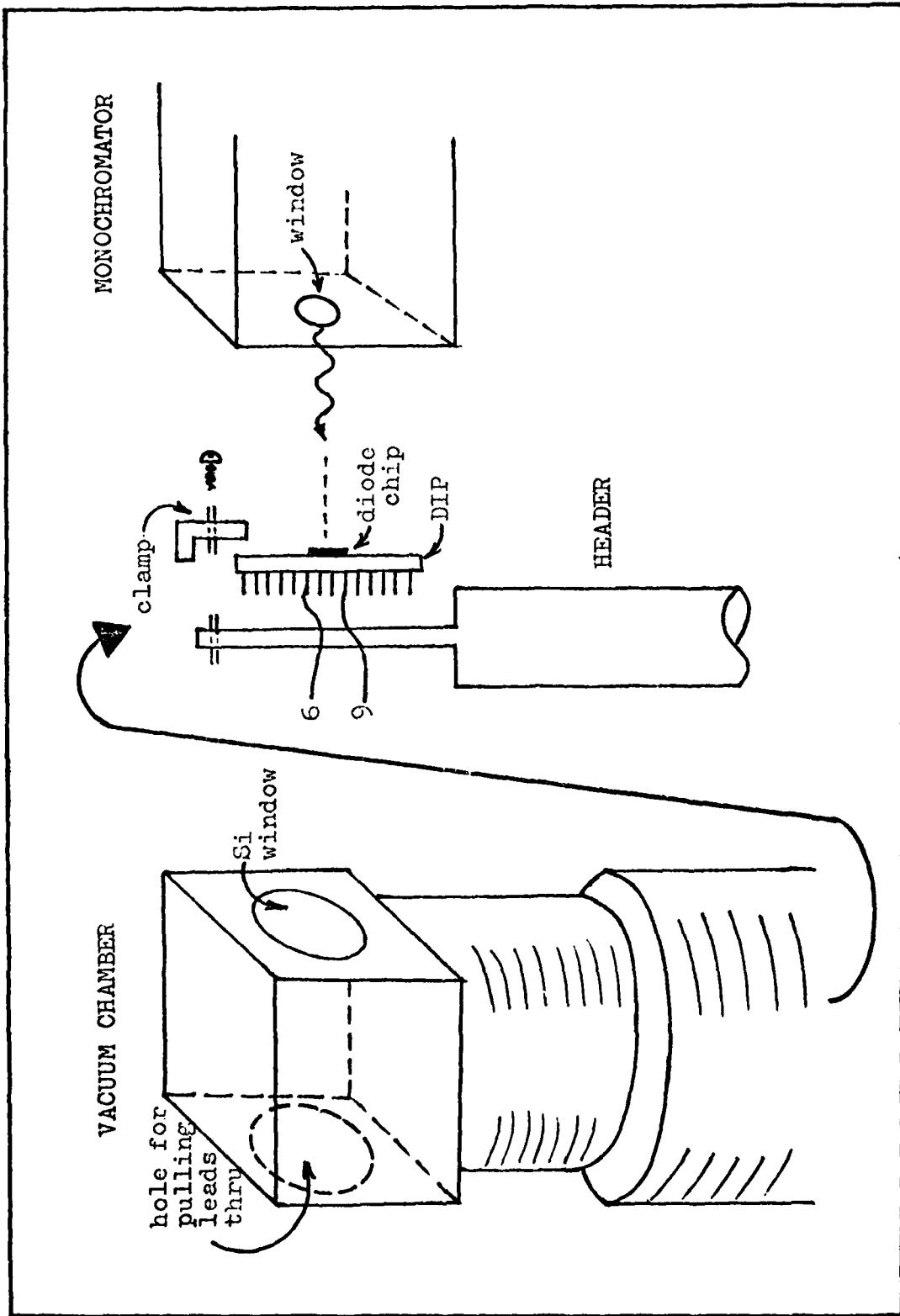


Fig 33. Laboratory set-up for mounting a sample for testing.

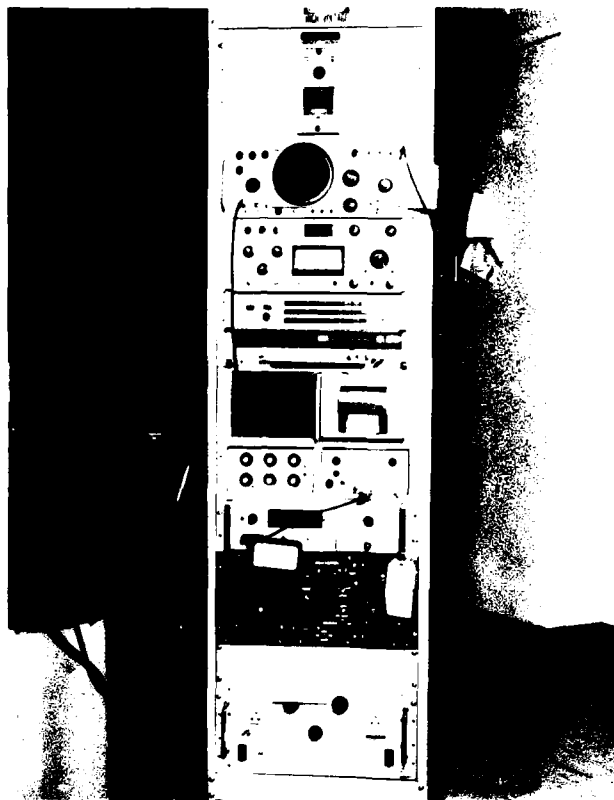


Fig 34. Panel of instruments used in processing and recording the output of the photodetector.

radiation through a slit. The sample mounted on the vacuum header receives the incident light through a silicon glass window which is aligned with the output window of the monochromator. The x-y alignment of the diode is adjustable at the base of the vacuum chamber. The bias voltage is set using the KEPCO programmer and DC regulated supply. Coaxial cables from the diode under test lead to a preamplifier which feeds the lock-in voltmeter for signal processing as outlined earlier. The 5055A digital recorder prints the output. A 100K resistor is connected in series with the diode so that what is actually being measured is the voltage across

the resistor due to the photocurrent generated at the wavelength selected by the monochromator. Therefore, the 3490A Multimeter is actually measuring output voltage. It will be converted to photocurrent later for determination of the photoresponse characteristics.

Full details of the experimental procedure are described in Appendix B. The test run consisted mainly of placing the diode under 0, 5, and 10V bias and obtaining the output voltage across a 100K resistance for the spectrum of wavelengths listed in Table IV. The raw data are presented in the following results chapter.

TABLE V

## List of Equipment used in the Photometric System.

<u>Instrument</u>	<u>Model</u>	<u>Serial No.</u>	<u>Manufacturer</u>
Monochromator	098	297	The Perkin-Elmer Corporation Norwalk, Ct.
Oscilloscope	RM503	002185	Tektronix, Inc. Portland, Oregon
Lock-In Voltmeter	131		Brower Laboratories Inc. Westboro, Mass.
Programmer	500		Brower Laboratories Inc. Westboro, Mass.
Multimeter	3490A		Hewlett Packard
Digital Recorder	5055A		Hewlett Packard
ABC Regulated DC Supply			KEPCO
Digital Programmer	KP-1	C-64409	KEPCO
Digital Voltmeter	3440A		Hewlett Packard
Automatic Range Selector	3442A		
Curve Tracer	577	B071481	Tektronix, Inc.
Standard Test Fixture	177		Tektronix, Inc.

## VI Results

This chapter presents the experimental results obtained with five photodetector diodes of varying structures. The results include the forward and reverse bias diode characteristics, the diode and contact diameters, and the output voltage as a function of applied bias for each sample. The I-V data points are listed in Tables C-1 through C-5 in Appendix C by sample number. The I-V characteristics will be given in a plot later in the next section. A list of diameters and resulting total areas is given in Table VI. The diameters for each diode were obtained by photographing the diode at high magnification (80x) and measured by using a 1mm scale photographed at the same magnification as shown in Figure 29. The area was calculated in square centimeters for convenience. For example, the total active area of photodiode G-7-1 #9 was found by subtracting the contact area from the total area of the diode:

$$\begin{aligned} \text{total area: } & \pi(0.062 \text{ cm})^2/4 \\ \text{contact area: } & - \pi(0.034 \text{ cm})^2/4 \\ \text{active area: } & 2.11 \times 10^{-3} \text{ cm}^2 \end{aligned}$$

which is the first entry in Table VI. It was assumed that no radiation penetrated the metallization of the contact.

As explained in Chapter V, the output voltage recorded is actually the voltage across a 100K resistor in series with the photodetector which is due to the photocurrent generated therein. These photovoltages are listed in Tables D-1 through D-10 in Appendix D for each sample for 0, 5, and 10 volts bias for each set of calibration data. These voltages are used to determine the photocurrent values simply by dividing by the 100K

TABLE VI

Diameters of Diodes and Contacts Used to Determine Active Area

	Total Diameter	Contact Diameter	Active Area
G-7-1 #9	0.62mm	0.34mm	$2.11 \times 10^{-3} \text{ cm}^2$
G-7-4 #23	0.52mm	0.33mm	$1.27 \times 10^{-3} \text{ cm}^2$
G-8-1 #23	0.97mm	0.34mm	$6.48 \times 10^{-3} \text{ cm}^2$
D-6-1 #6	0.49mm	0.08mm	$1.84 \times 10^{-3} \text{ cm}^2$
D-6-3 #6	0.49mm	0.08mm	$1.84 \times 10^{-3} \text{ cm}^2$

resistance. At 5 volts, the output voltage of G-7-1 #9 at a wavelength of  $1.46 \mu\text{m}$ , is  $122225 \mu\text{V}$ . To obtain the photocurrent, Ohm's law is applied:

$$I = \frac{V}{R} = \frac{1222225 \mu\text{V}}{100 \text{ K}\Omega} = 1.22225 \mu\text{A}.$$

The values for photocurrent, incident optical power, responsivity and quantum efficiency are tabulated in Tables E-1 through E-30 in Appendix E. Since the active area varied with each device, it was important to know the actual optical power falling on a particular diode. Given this quantity in  $\mu\text{W}$  per  $\text{cm}^2$  for each wavelength, because the output of the globar was not uniform over its spectral range, it was a simple matter to convert the optical power to  $\mu\text{W}$  in direct relation to the area of a specific diode. The power is listed next to the photocurrent for ease in calculating the photoresponse.

As a sample calculation, consider the photoresponse of G-7-1 #9 at a wavelength of  $1.46 \mu\text{m}$  and 5 volts bias. It is obtained as defined in Equation (7) of Chapter II. The output of the globar is  $623 \mu\text{W}/\text{cm}^2$ , or

$(623 \mu\text{W}/\text{cm}^2) \times (2.111 \times 10^{-3} \text{cm}^2) = 1.3152 \mu\text{W}$  in this case. Then

$$R = \frac{I}{H} = \frac{1.22225 \mu\text{A}}{1.3152 \mu\text{W}} = 0.929 \mu\text{A}/\mu\text{W}$$

Quantum efficiency is obtained by Equation (15) in Chapter II:

$$\eta = R \frac{1.24}{\lambda(\mu\text{m})} = (0.929) \frac{(1.24)}{(1.46)} = 79.7\%$$

It is defined as the number of electrons generated per photon.

A better grasp of the significance of the results of the experiment can be obtained from plots of photoresponse and quantum efficiency as a function of wavelength. These are shown and discussed in the following section. Other results which were previously given in Table III but not mentioned in context are discussed in the following paragraph.

The availability of spare samples made it possible to bevel and stain a diffused diode to determine its junction depth,  $x_j \sim 1.2 \mu\text{m}$ . Although the luxury of spare samples did not extend to the implanted samples, an estimate of the junction depth can be made from the predictions of Linhart, Scharff and Schiøtt (LSS theory). At 200 KeV, an As implant can be expected to reach a junction depth of  $x_j \sim 1.0 \mu\text{m}$  (Ref 17). It is known from other work that for As implants in Si and Ge under conditions like those in this experiment the measured impurity profiles are reasonably close to those of LSS theory. A measurement of carrier lifetime in the diffused diodes came to  $\tau = 2.25 \mu\text{sec}$  which will also be discussed further in the next section.

In summary, detailed data was obtained on a fairly restricted set of samples. This must now be examined to evaluate the effectiveness of the shallow junction structure. The next chapter describes the analysis.

## VII Analysis of Results

This chapter presents the experimental results of the preceding chapter as curves and analyzes the performance of each diode with varying structures. The forward and reverse bias curves are displayed in Figures 35 through 39 and discussed in terms of diode characteristics. The peak optical characteristics at 10V bias are plotted in Figures 40 through 44 for each set of calibrated data listed in Table IV. The performance of each device can be compared to other Ge photodiodes listed in Table I.

A comparison of the I-V curves of the implanted and diffused diodes reveals the nicer overall characteristics of the diffused samples. The lower, flatter reverse bias currents, characteristic of the diffused samples can probably be attributed to the following features: uniformity of the diffused junction, cleaner processing, and mesa etching. These diodes were fabricated using well developed IC technology, i.e. standard masking and photoresist film processes. Cleaner processing refers to the fabrication of these devices in a clean room using well-established cleaning procedures. Due to the very clean environment during fabrication and tried masking procedures, the probability of a high density of defects is low, assuming a high quality wafer is used to begin with. In contrast, the implanted diodes exhibit higher reverse bias currents, 3-13  $\mu\text{A}$  for implanted diodes versus 1.5-5  $\mu\text{A}$  for diffused diodes. Absorption problems due to humidity are notoriously associated with Ge photodiodes. These diodes were no exception. Under vacuum the higher ( $\sim 10 \mu\text{A}$ ) leakage currents of the diffused diodes was reduced to those plotted in the Figures.

The implanted diodes, on the other hand, were not plagued by absorption problems. Implanted I-V characteristics did not change under vacuum.

The purpose for mesa-etching the two diffused and one implanted diodes was to reduce the leakage current. The mesa structure was necessary to define the area of the photodiodes which had been diffused across the surface of the starting wafer. The decrease in leakage currents is supported by comparing the I-V curves of the five samples. The bottom line of the low leakage current subject is reduced shot noise caused by injected carriers in the p-n junction as discussed in Chapter II. A study of noise characteristics was not done in conjunction with this thesis. With a "picture" of the five diodes in mind, an analysis of the optical characteristics of the photodiodes follows.

The photoresponse characteristics of each sample are plotted at 10V bias for each set of calibration data, thereby making two sets of optical performance data available for comparison. In general, the shape of the response curves agrees with the well known response curves of Ge photodiodes as shown in Figure 1 of Chapter I. Peak response occurs at about  $1.46 \mu\text{m}$  for all the samples. The drop in responsivity in the  $1.0\text{-}1.3 \mu\text{m}$  range is probably due to the drop in optical power at these wavelengths due to reflection losses. A suitable antireflection coating is likely to solve this problem. A study of the photoresponse characteristics of samples G-7-4 #23, D-6-1 #1, and D-6-3 #6 in the Tables referred to in Chapter VI reveal responsivities greater than  $1 \mu\text{A}/\mu\text{W}$  and quantum efficiencies greater than 100% at peak performance. The problem may be attributed to the active areas of the diodes listed in Table VI which are very small in comparison to the other diodes. The responsivity and quantum

efficiency were normalized accordingly to compare the shapes of the curves, which agree with well known results.

Diode G-7-1 #9 has the best photocharacteristics of the five samples. It is a simple planar implanted Ge photodiode displaying peak responsivity of about  $0.9 \mu\text{A}/\mu\text{W}$  and peak efficiency of about 80%. These performance values can compete easily with the other Ge photodiodes described in Table I. The gain in performance is attributed to the shallow junction.

Another characteristic of the Ge photodiodes is carrier lifetime which plays a role in the denominator of the leakage current as shown in Equation (26) (Ref 1; 4; 7; 18; 19; 30; 33; 43; 47; 55). An increase in carrier lifetime would decrease the leakage current. In contrast to Ando's planar avalanche photodiode in Table I which claims a lifetime of 0.9ns, the measured lifetime for the diffused diodes is  $2.25 \mu\text{s}$ ; there is an obvious discrepancy in the orders of magnitudes. High responsivity in the APD is due to the photomultiplication mechanism and requires low values of lifetime to increase the speed performance. On the other hand, in the p-n junction, the high response is due to the shallow junction structure and the "instantaneous" collection of photogenerated carriers in a region where there is a high amount of light absorbed. The longer lifetime reduces the leakage current responsible for noise in p-n diodes, whereas the low lifetime of the APD's makes them inherently noisy devices.

In summary, the response of the planar Ge photodiodes displayed peak performance at the expected  $1.46 \mu\text{m}$  wavelength with competitive values of photoresponse and quantum efficiency. The use of an AR coating is also expected to improve the photocharacteristics. Better IC fabrication facilities would be expected to improve the performance even more.

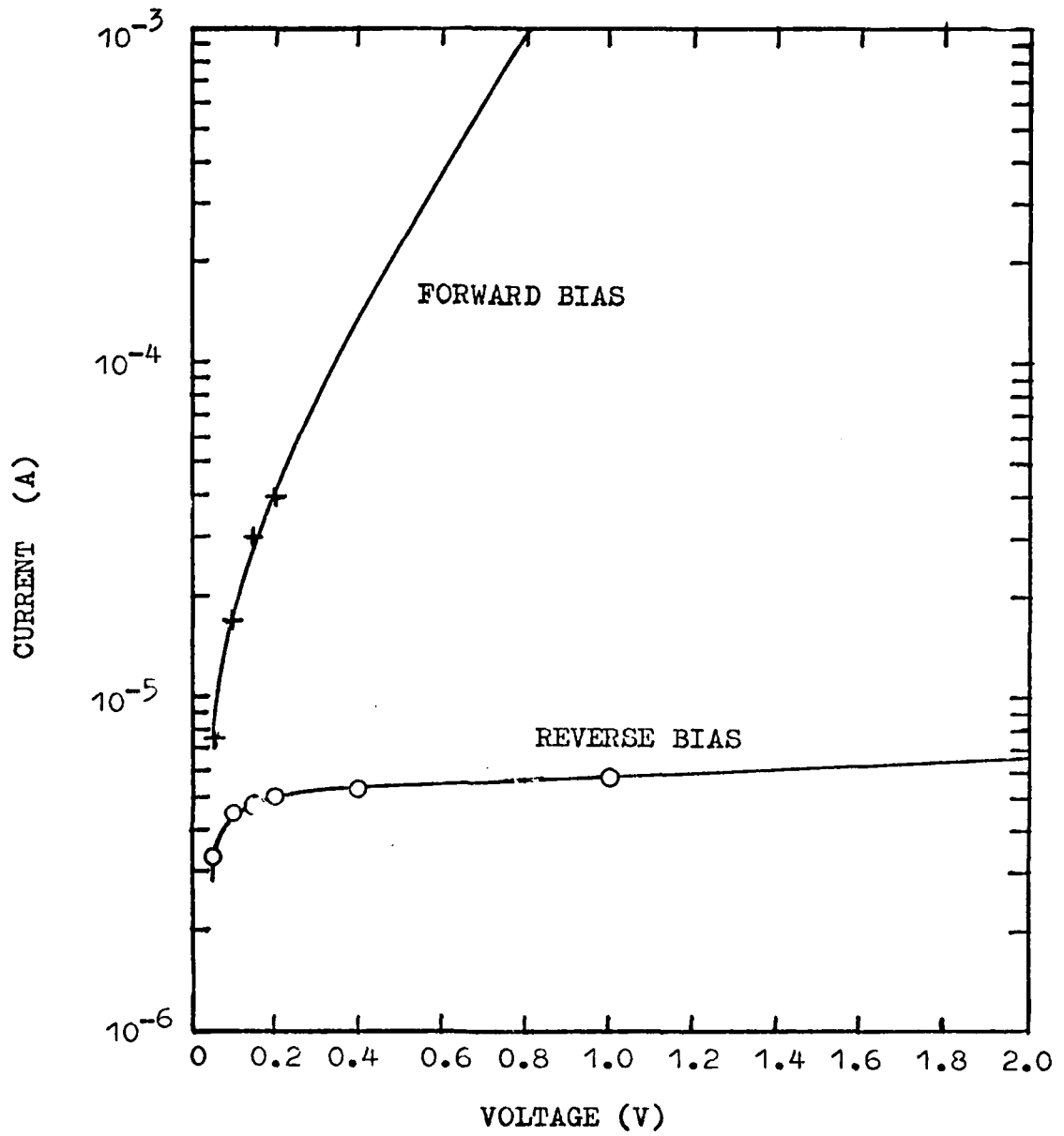


Fig 35. I-V characteristics of G-7-1#9.

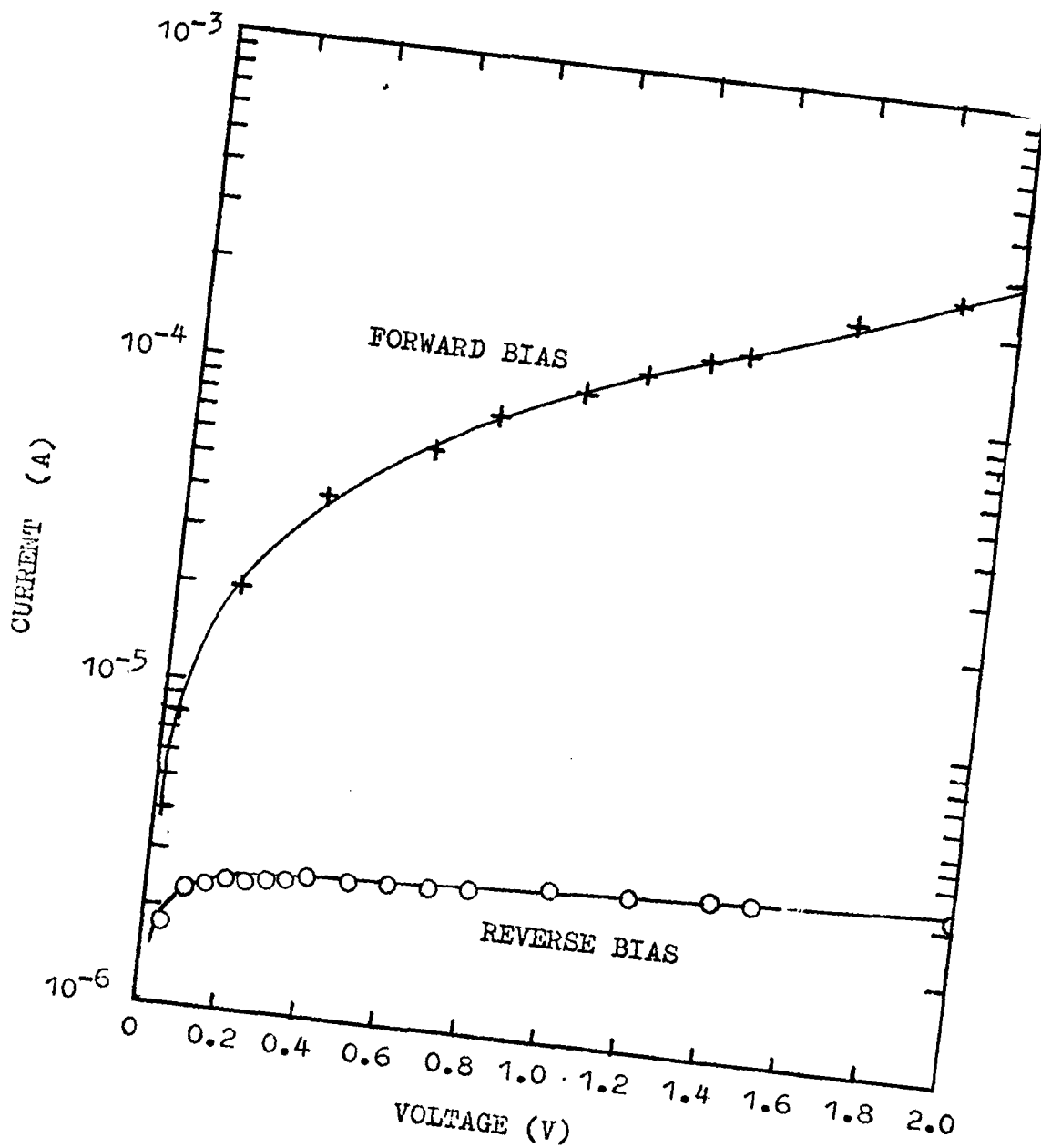


Fig 36. I-V characteristics of G-7-4#23.

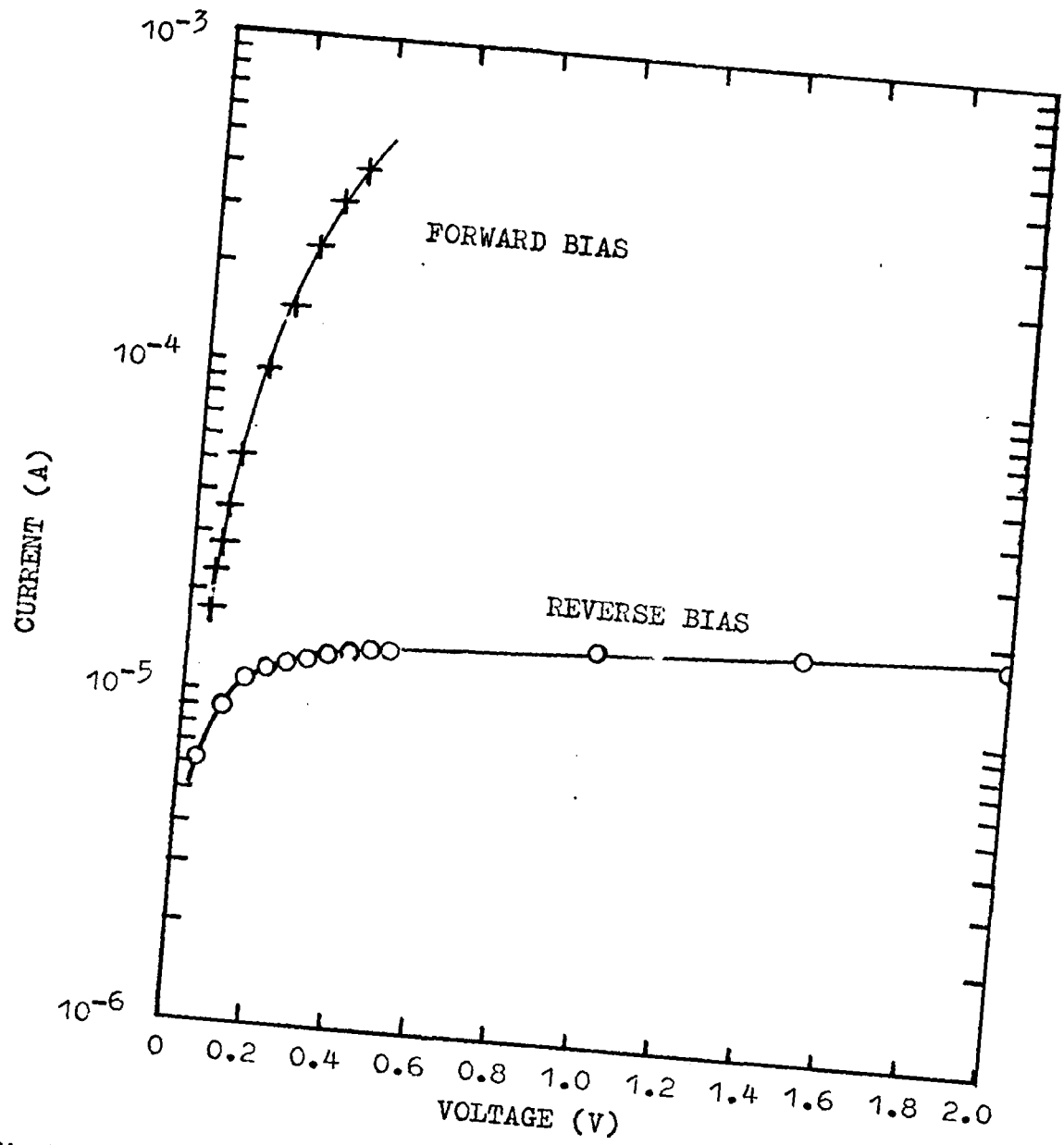


Fig 37. I-V characteristics of G-8-1#23.

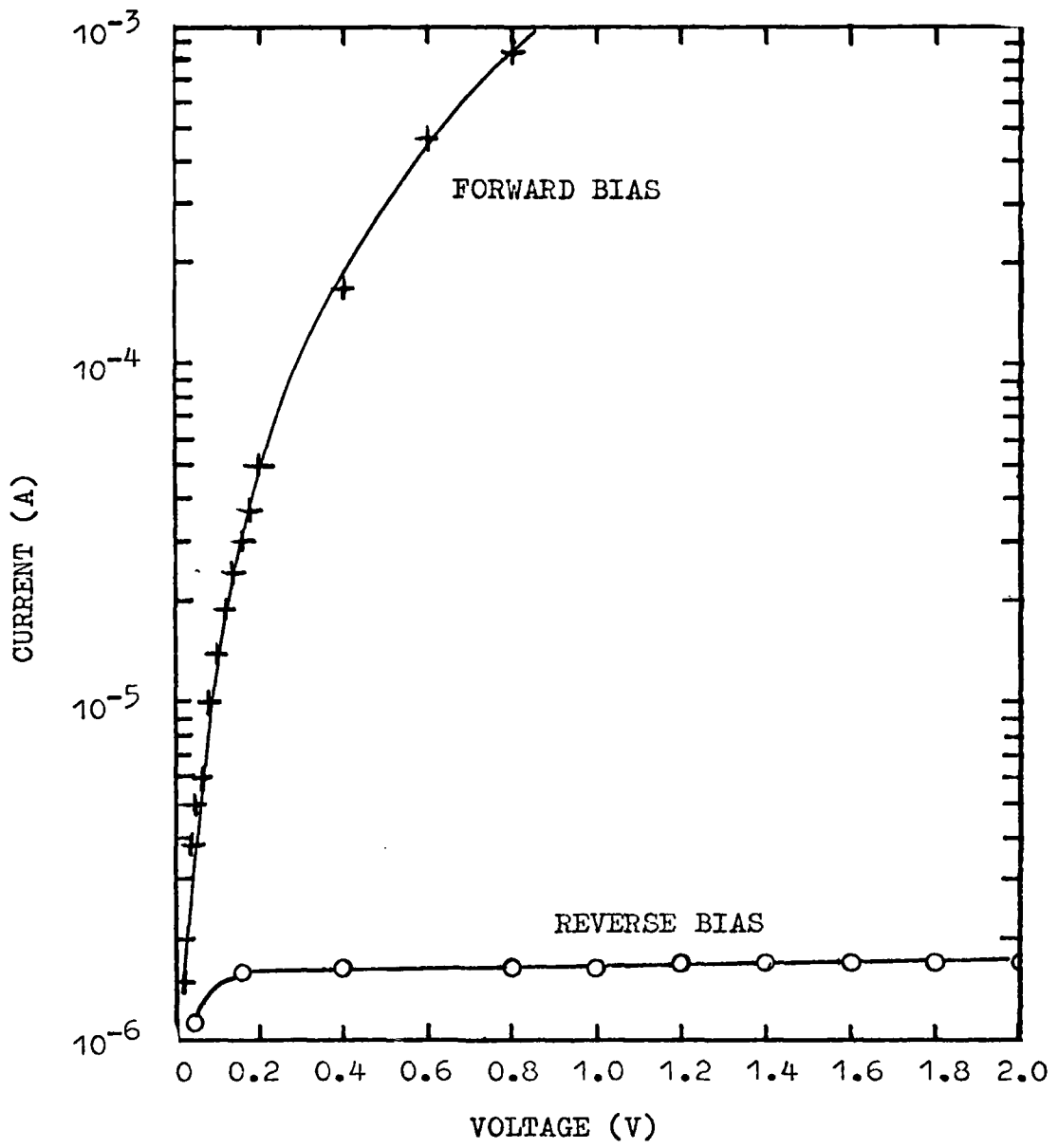


Fig 38. I-V characteristics of D-6-1#6.

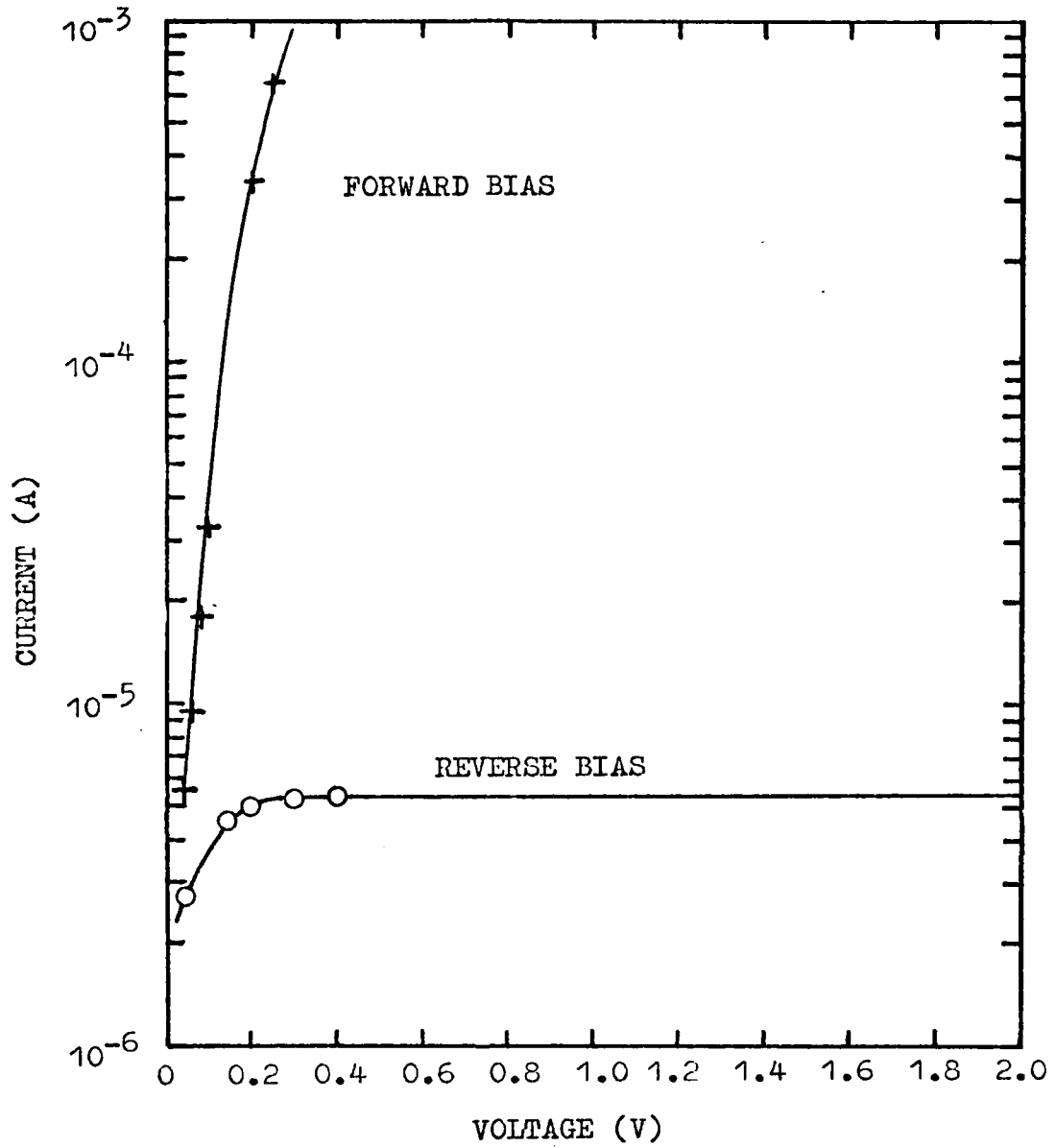


Fig 39. I-V characteristics of D-6-3#6.

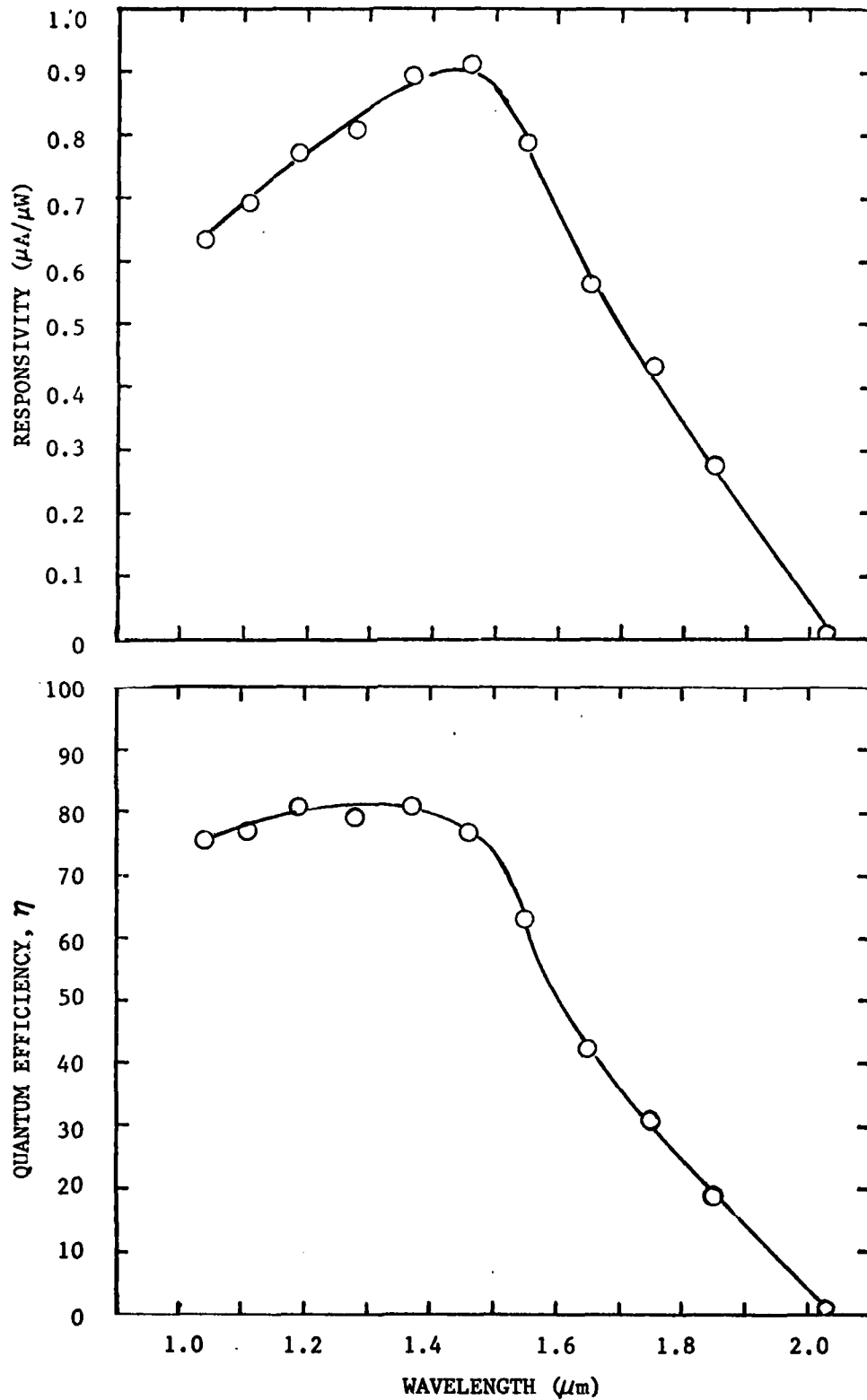


Fig 40(a). Photoresponse and quantum efficiency curves of G-7-1#9 at 10 V bias for H\* calibration data.

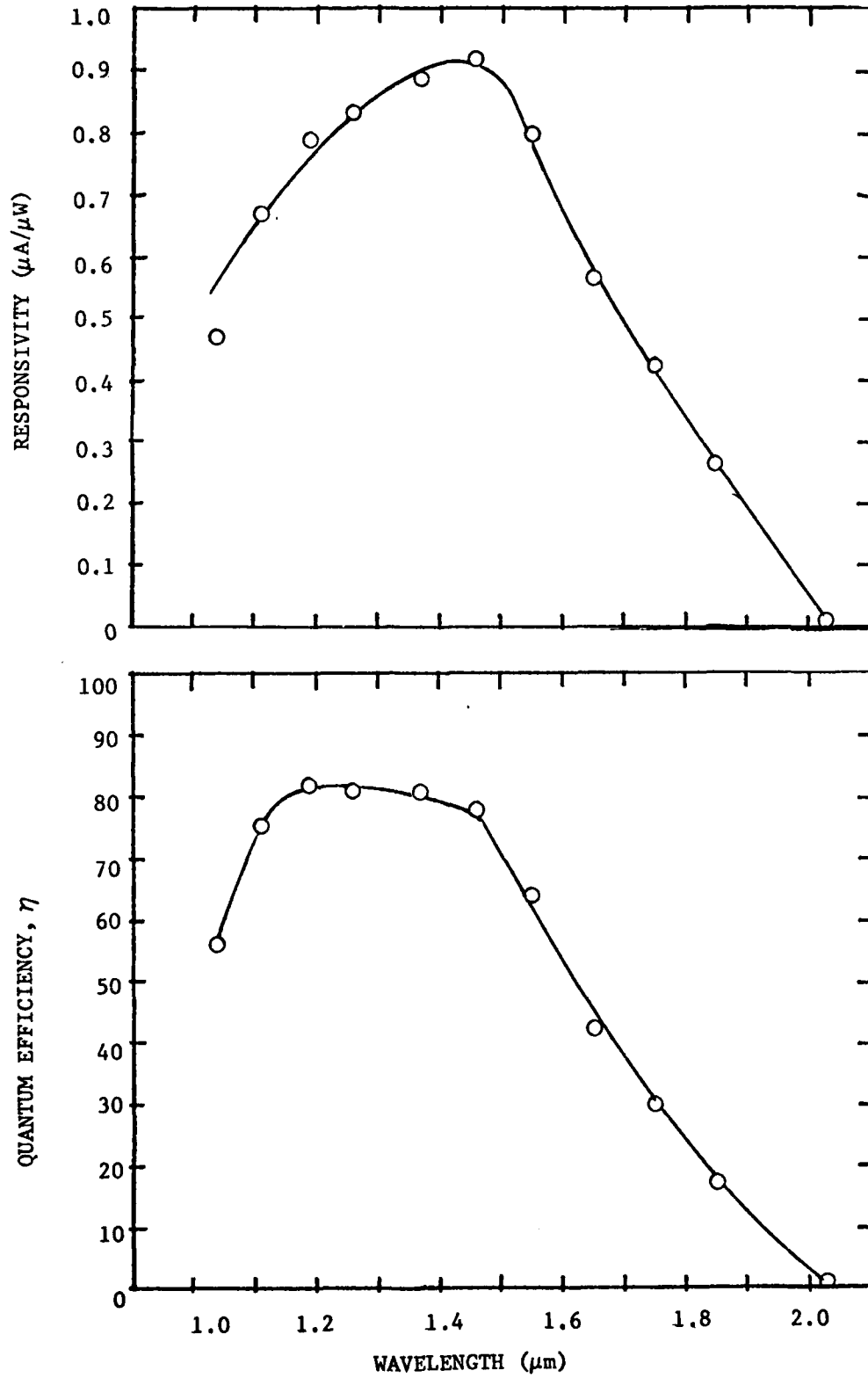


Fig 40(b). Photoresponse and quantum efficiency curves of G-7-1#9 at 10 V bias for H\*\* calibration data.

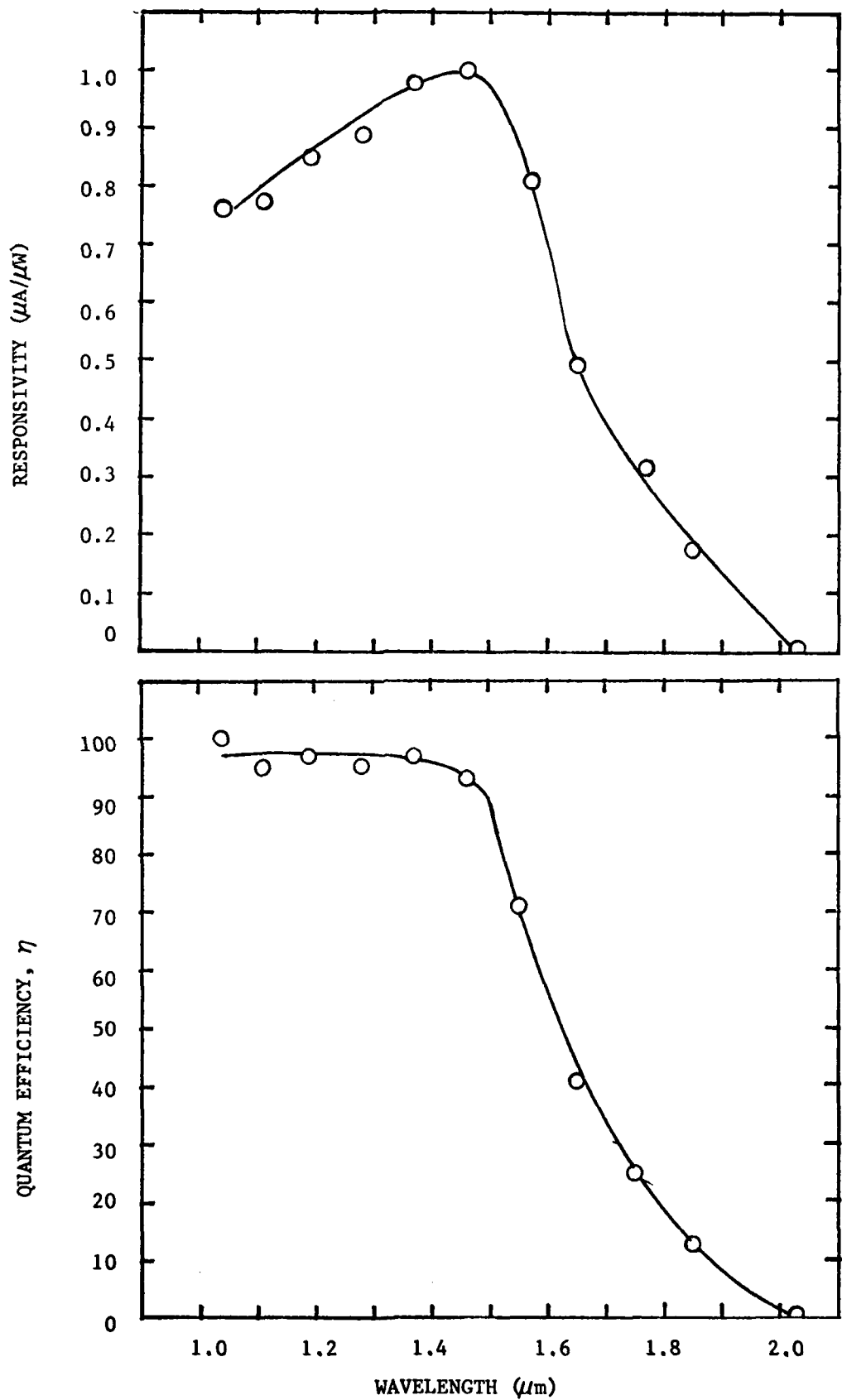


Fig 41(a). Photoresponse and quantum efficiency curves of G-7-4#9 at 10 V bias for H\* calibration data.

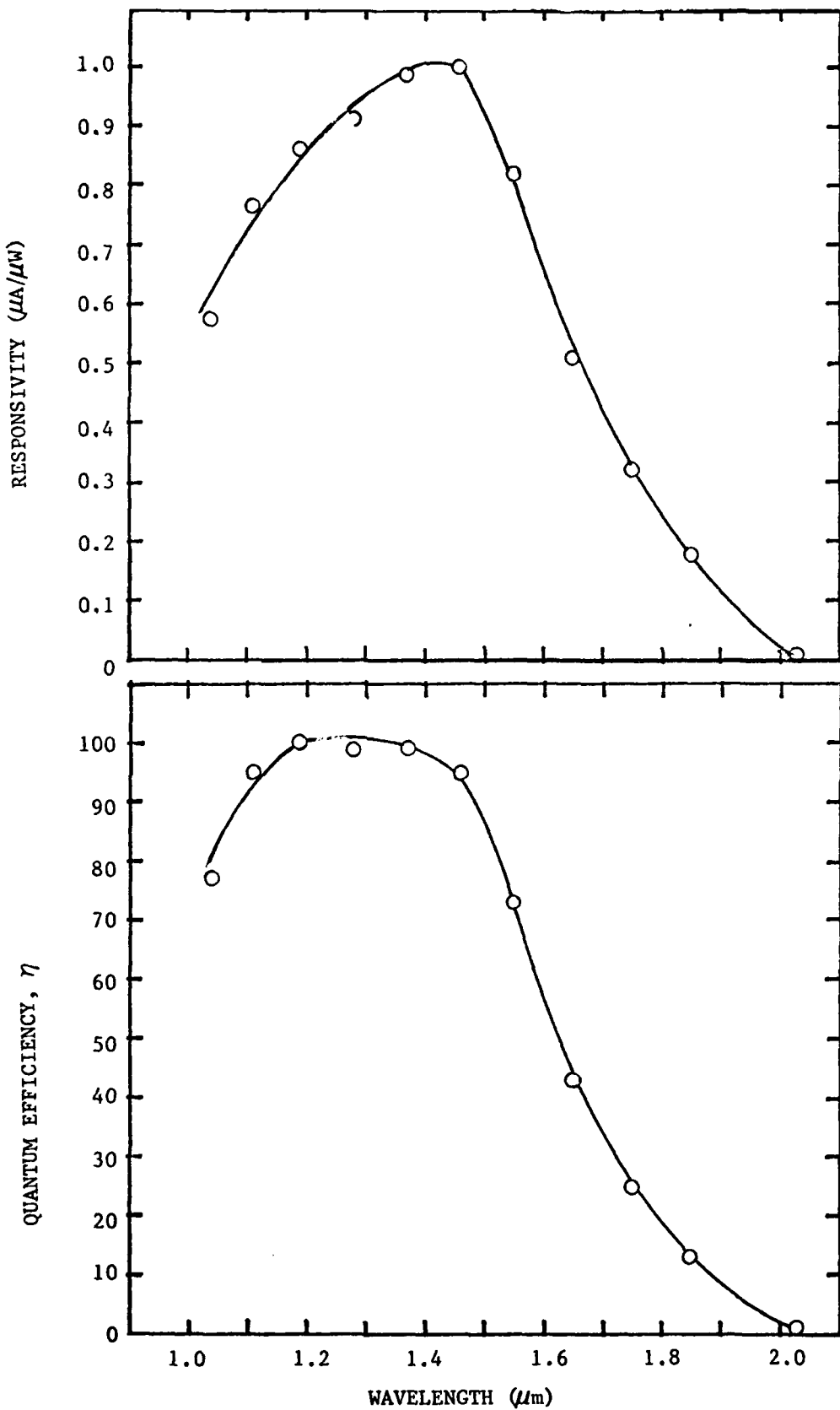


Fig 41(b). Photoresponse and quantum efficiency curves of G-7-4#9 at 10 V bias for H\*\* calibration data.

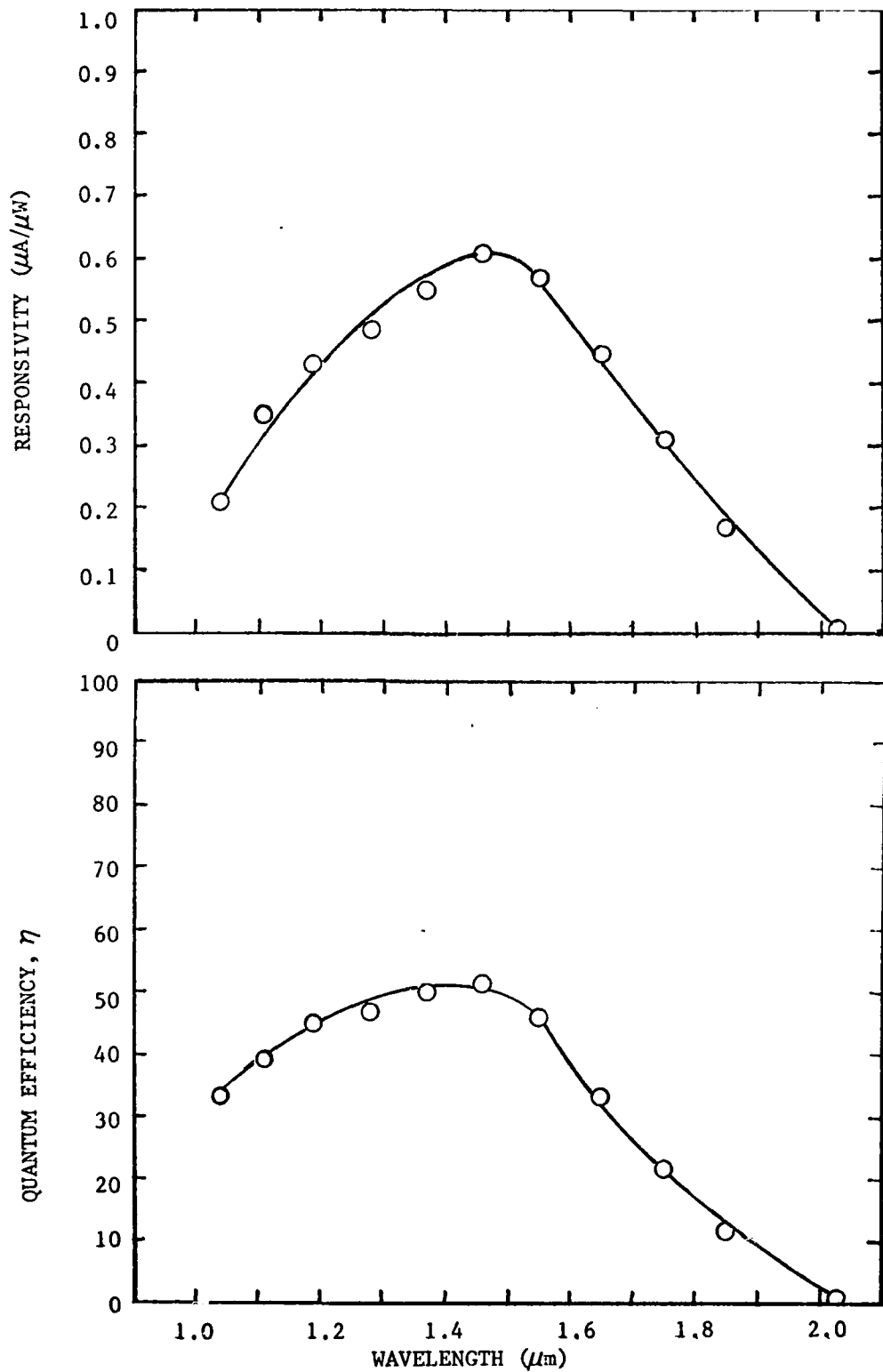


Fig 42(a). Photoresponse and quantum efficiency curves of G-8-1#23 at 10 V for H\* calibration data.

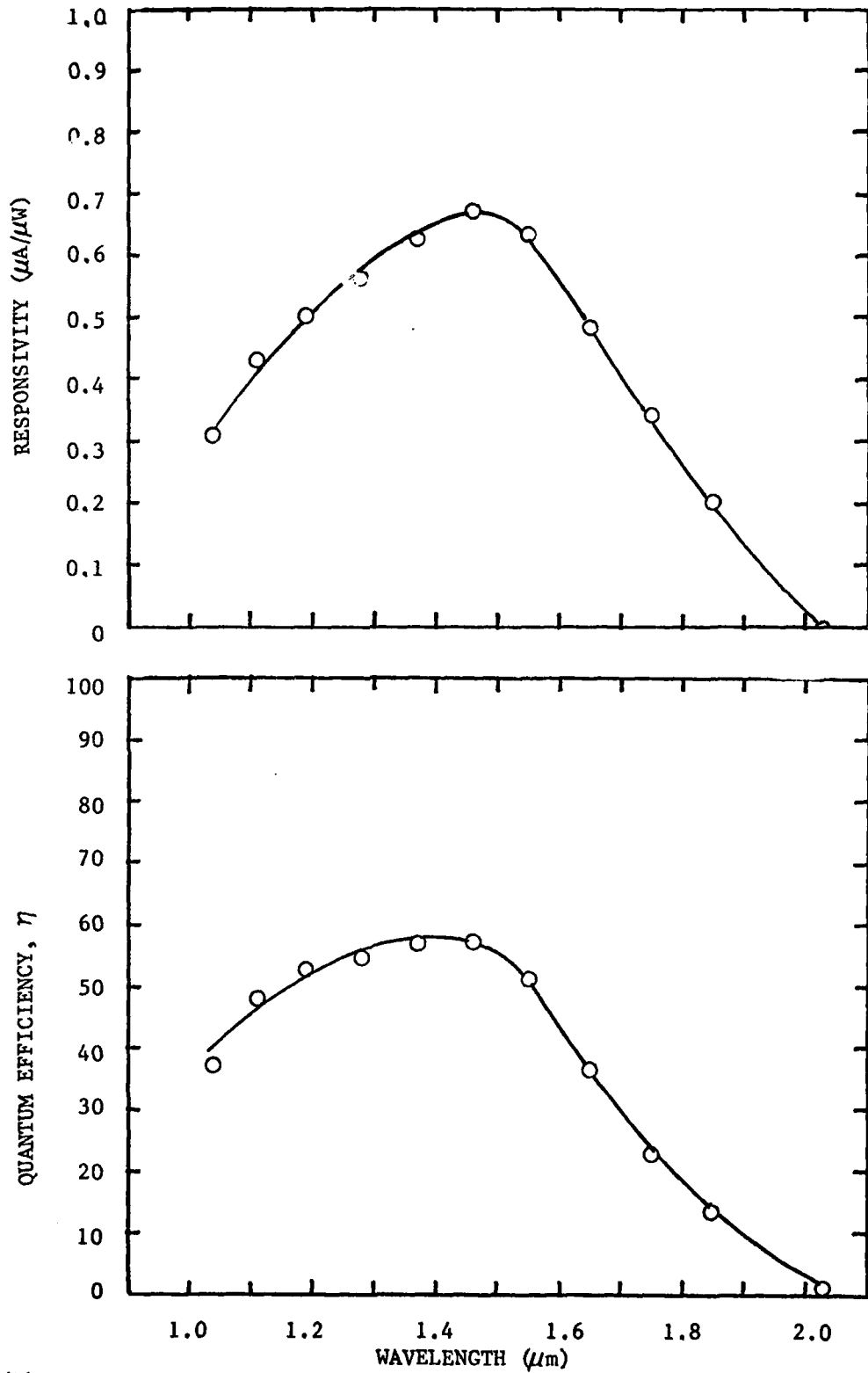


Fig 42(b). Photoresponse and quantum efficiency curves of G-8-1#23 at 10 V bias for H\*\* calibration data.

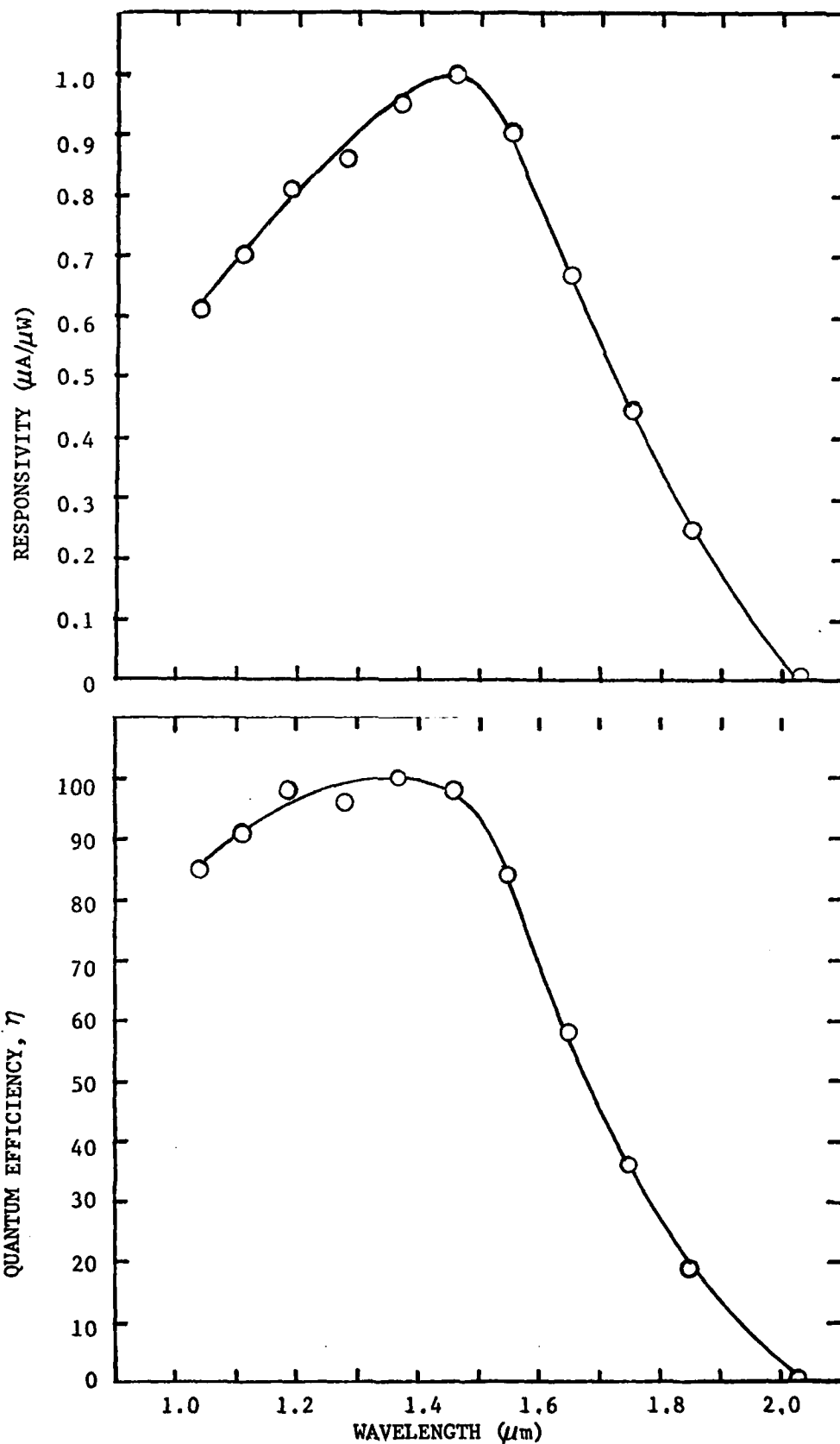


Fig 43(a). Photoresponse and quantum efficiency curves of D-6-1#6 at 10 V bias for H\* calibration data.

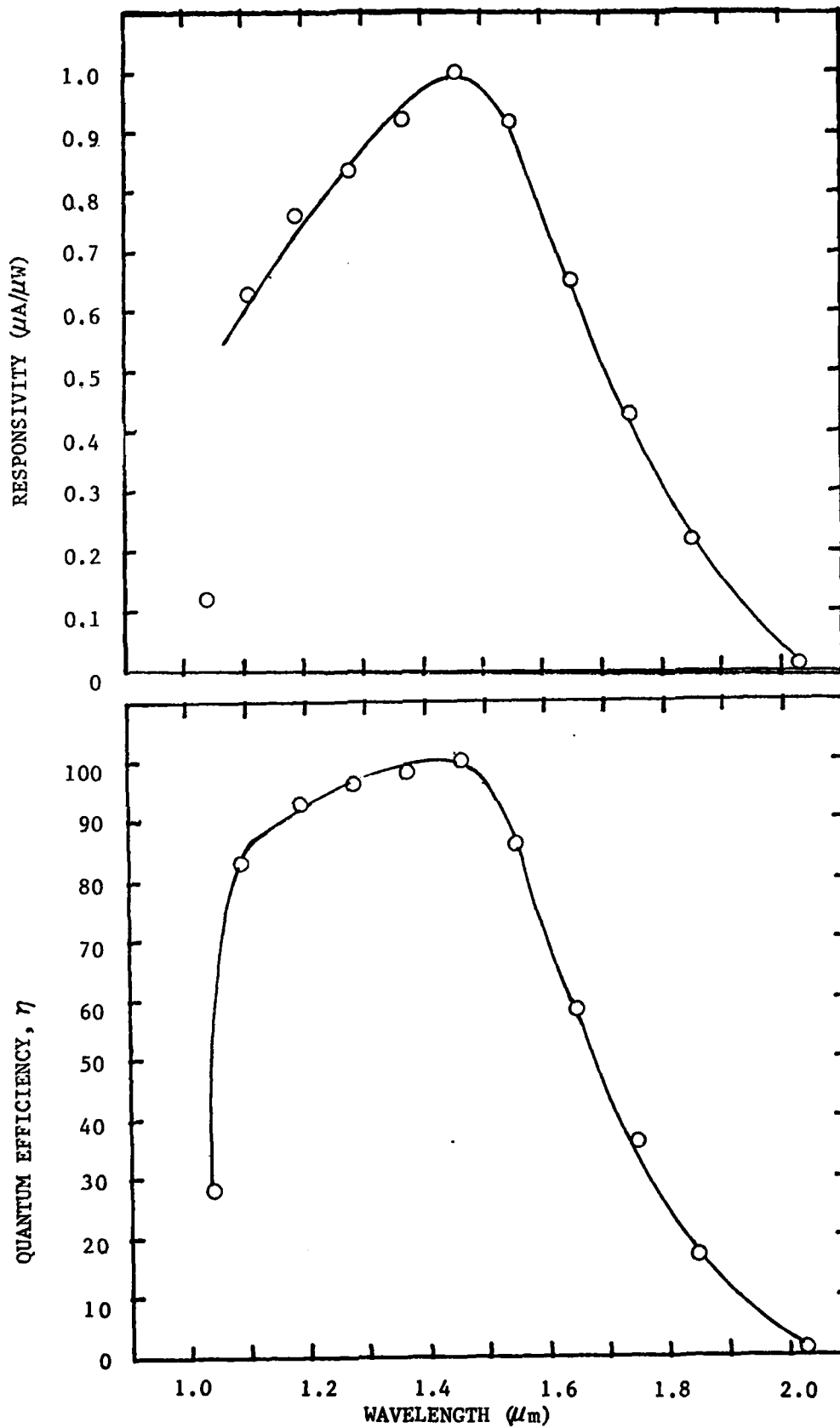


Fig 43(b). Photoresponse and quantum efficiency curves of D-6-1#6 at 10 V bias for H\*\* calibration data.

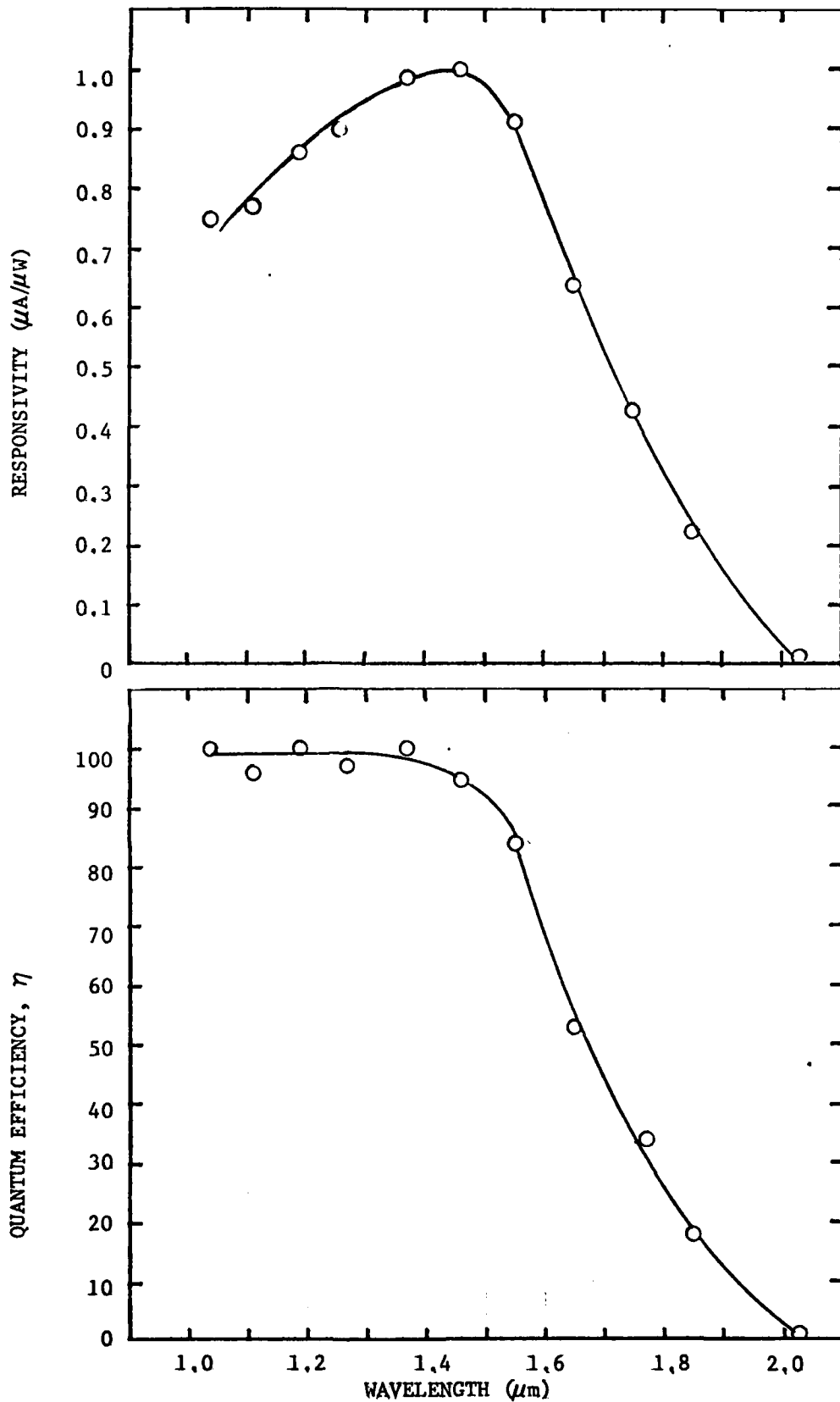


Fig 44(a). Photoresponse and quantum efficiency curves of D-6-3#6 at 10 V bias for H\* calibration data.

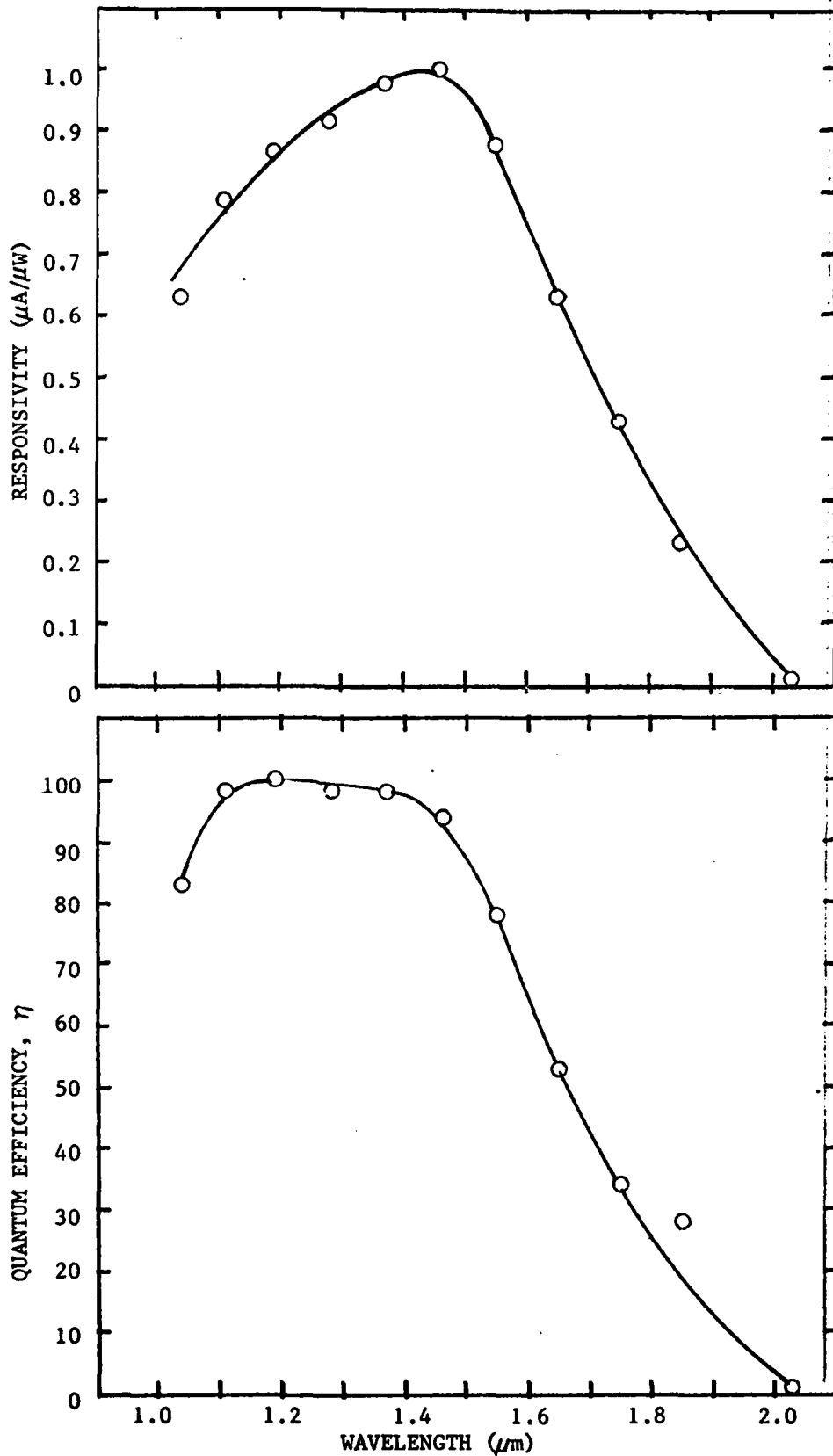


Fig 44(b). Photoresponse and quantum efficiency curves of D-6-3#6 at 10 V bias for H\*\* calibration data.

## VIII Conclusions and Recommendations

In conclusion, the feature which increases the performance characteristics of the everyday Ge photodiode is the implementation of a shallow junction to "capture" most of the light absorbed within  $5\ \mu\text{m}$  from the surface. The best response values for an implanted sample were  $R=0.9\ \mu\text{A}/\mu\text{W}$  and  $\eta = 80\%$ , competitive with other diffused Ge photodiode structures which have been studied. The performance can be further improved with an AR coating to reduce leakage currents, and encapsulant to avoid problems with humidity, guard rings, side contacts, and other conventional improvements not feasible in research facilities.

In the area of Ge-Si alloy crystal growth which is in its very early stages of development, a quantum mechanical analysis of the Ge-Si energy band structure should be made using the tight-binding approximation. A repeated application of the LCAO method as outlined by Slater and Koster should be applied to a representative group of unit cells whose total volume represents a concentration 10% Si and 90% Ge. The band structure of the Ge-Si alloy would be a weighted average of the energy band structures of the individual unit cells. The results of this modeling should predict the energy band structure of the crystal alloy and in doing so its effective mass and energy gap, thereby predicting the behavior of electrons and holes under the influence of an applied field. Also recommended are optical and cyclotron resonance experiments to quantify the theoretical results for bandgap and effective mass values respectively. These values, at crucial points in the symmetry points of the Brillouin zone, would be

helpful in fitting the constants arising in the LCAO method at nonsymmetry points in the zone. Once the Ge-Si alloy is grown and is available in wafer form, a shallow-junction Ge-Si photodiode should be fabricated and tested. It is expected that Ge-Si photodetector will exhibit a peak photoresponse of about  $0.8 - 0.9 \mu\text{A}/\mu\text{W}$  at  $1.27 \mu\text{m}$  where the optical fiber experiences minimum attenuation and dispersion, thereby optimizing system performance in fiber-optic applications.

## Bibliography

1. Alton, G. D. and L. O. Love. "Radiation Damage and Substitutional Chemical Impurity Effects in Single-Crystal Germanium Bombarded with 40 KeV B<sup>+</sup>, Al<sup>+</sup>, Ga<sup>+</sup>, Ge<sup>+</sup>, P<sup>+</sup>, As<sup>+</sup>, and Sb<sup>+</sup> Ions," Canadian Journal of Physics, 46: 695-704 (1968).
2. Ando, Hiroaki, et al. "Characteristics of Germanium Avalanche Photodiodes in the Wavelength Region of 1-1.6  $\mu\text{m}$ ," IEEE Journal of Quantum Electronics, QE-14 (11): 804-809 (November 1978).
3. Bender, Albert and Steven Storozum. "Charts Simplify Fiber-Optic System Design," Electronics, 51(24): 135-142 (November 1978).
4. Blicher, A. and I. H. Kalish. "Reverse Characteristics of Low Lifetime Germanium Diodes," Proceedings of the IRE, 49(9): 1427 (September 1961).
5. Braunstein, Rubin, et al. "Intrinsic Optical Absorption in Germanium-Silicon Alloys," Physical Review, 109(3): 695-710 (February 1, 1958).
6. Brower, Richard. "Taking Noise Out of Weak Signals," Electronics, 42(14): 80-90 (July 8, 1968).
7. Burton, J. A., et al. "Effect of Nickel and Copper Impurities on the Recombination of Holes and Electrons in Germanium," Physical Review: 853-859 (November 1953).
8. Callaway, Joseph. Energy Band Theory. New York: Academic Press, 1964.
9. Chamberlain, Savvas G., et al. "Spectral Response Limitation Mechanisms of a Shallow Junction n<sup>+</sup>-p Photodiode," IEEE Transactions on Electron Devices, ED-25(2): 241-246 (February 1978).
10. Cohen, Marvin L. and T. K. Bergstresser. "Band Structures and Pseudopotential Form Factors for Fourteen Semiconductors of the Diamond and Zinc-Blende Structures," Physical Review, 141(2): 89-796 (January 1966).
11. Conradi, J. "Planar Germanium Photodiodes," Applied Optics, 14(8): 1948-1952 (August 1975).
12. Conradi, Jan, et al. "Fiber-Optical Transmission Between 0.8 and 1.4  $\mu\text{m}$ ," IEEE Journal of Solid State Circuits, SC-13(1): 106-119 (February 1978).
13. Conwell, E. M. "Properties of Silicon and Germanium: II," Proceedings of the IRE, 46: 1281-1300 (June 1958).

14. Dash, W. C. and R. Newman, "Intrinsic Optical Absorption in Single Crystal Germanium and Silicon at 77<sup>o</sup>K and 300<sup>o</sup>K," Physical Review, 99: 1151 (1955).
15. Eisberg, Robert and Robert Resnick. Quantum Physics of Atoms, Molecules, Solids, Nuclei, and Particles. New York: John Wiley and Sons, Inc., 1974.
16. General Purpose Building Block Monochromators. Norwalk, Connecticut: The Perkin-Elmer Corporation, November 1962.
17. Gibbons, J. F., W. S. Johnson, and S. W. Mylroie. Projected Range Statistics (Second Edition). Stroudsburg, Pennsylvania: Halsted Press, 1975.
18. Glicksman, Maurice. "Mobility of Electrons in Germanium-Silicon Alloys," Physical Review, 111(1): 125-128 (July 1, 1958).
19. Goucher, F. S., et al. "Theory and Experiment for a Germanium P-N Junction," Physical Review, 81: 637-638 (February 1951).
20. Grove, A. S. Physics and Technology of Semiconductor Devices. New York: John Wiley and Sons, Inc., 1967.
21. Hansen, Mas, Dr. Phil. Constitution of Binary Alloys, Second Edition. New York: McGraw-Hill Book Company, Inc., 1958.
22. Hemenway, Curtis L., et al. Physical Electronics (Second Edition). New York: John Wiley and Sons, Inc., 1967.
23. Herman, Frank. "The Electronic Energy Band Structure of Silicon and Germanium." IRE Proceedings, 43: 1703-1732 (December 1955).
24. Herman, F. "Electronic Structure of the Diamond Crystal," Physical Review, 88(5): 1210-1211 (December 1, 1952).
25. Herman, Frank and Joseph Callaway. "Electronic Structure of the Germanium Crystal," Physical Review, 89(3): 518-519 (January 15, 1953).
26. How the Lock-In Amplifier Works. Westboro, Massachusetts: Brower Laboratories, Inc., 1968.
27. Johnson, Everett R. and Schuyler M. Christian. "Some Properties of Germanium-Silicon Alloys," Physical Review, 95(2): 560-561 (1954).
28. Kao, C. K. and J. E. Goell. "Design Process for Fiber-Optic Systems Follows Familiar Rules," Electronics, 49(19): 113-116 (September 1976).
29. Kittel, Charles. Introduction to Solid State Physics (Third Edition). New York: John Wiley and Sons, Inc., 1966.

30. Large, L. N. and H. Hill. "Junction Formation in Germanium by Sb<sup>+</sup> Ion Bombardment," Paper presented at the International Conference on Electron and Ion Beam Science and Technology. New York, April 1966.
31. Lee, Mike, et al., Hughes Aircraft Company, Carlsbad, California 92008; and Helmut Lefevre, Universital Erlangen, D-852 Erlangen, West Germany. "D.L.T.S. Measurements of a Germanium M-I-S Interface," Paper presented at 21st Electronic Materials Conference. Boulder, Colorado: University of Colorado at Boulder, June 27-29, 1979.
32. Logan, R. A. and M. Schwartz. "Restoration of Resistivity and Lifetime in Heat Treated Germanium," Journal of Applied Physics, 26(11): 1287-1289 (November 1955).
33. ----- . "Thermal Effects on Lifetime of Minority Carriers in Germanium," Physical Review, 96(1): 46 (October 1, 1954).
34. Math, Irwin. "For Response to Longer Wavelengths Than Silicon Try Germanium Diodes With Similar Characteristics," Laser Focus, 13(11): 91 (November 1977).
35. McKelvey, John P. Solid State and Semiconductor Physics. New York: Harper and Row, 1966.
36. Melchior, Hans, et al. "Photodetectors for Optical Communication Systems," Proceedings of the IEEE, 58(10): 1466-1486 (October 1970).
37. Melchior, H. "Sensitive High Speed Photodetectors for the Demodulation of Visible and Near Infrared Light," Journal of Luminescence, 7: 390-414 (1973).
38. Midwinter, John E. Optical Fibers for Transmission. New York: John Wiley and Sons, Inc., 1979.
39. Model 99 Double Pass Monochromator. Norwalk, Connecticut: The Perkin-Elmer Corporation, Instrument Division, MPL5602 #10535.
40. Nagai, Haruo. "Passivation of Germanium Devices(I): Preparation of Passivation Films by Chemical Reaction," Review of the Electrical Communication Laboratories, 22(11-12): 1043-1056 (November-December 1974).
41. Nittrouer, Charles A. "Modern Signal Processing Techniques for Overcoming Noise," Technical Notes. Princeton, N.J.: by Milton S. Kiver Publications, Inc. for Princeton Applied Research Corporation, 1968. Reprinted from September and October 1968 issues of Electronic Instrument Digest.
42. Nussbaum, Allen. "Group Theory and the Energy Band Structure of Semiconductors." IRE Proceedings, 50: 1762-1781 (August, 1962).

43. Pell, E. M. "Recombination Rate in Germanium by Observation of Pulsed Reverse Characteristics," Physical Review, 90(2): 278-279 (April 15, 1953).
44. Pierce, Bruce, Capt. "An Introduction to Energy Band Theory." A paper to Professor J. Lubelfeld for EE5.71 Molecular Electronics II.
45. A Practical Guide to Measurement of Weak Signals Buried in Noise. Westboro, Massachusetts: Brower Laboratories, Inc., 1968.
46. Primak, W., et al. "Peroxide Etching of Germanium," Journal of Electrochemical Society, 1(1): 88-91 (January 1967).
47. Prince, M. B. "Drift Mobilities in Semiconductors. I. Germanium," Physical Review, 92(3): 681-687 (November 1, 1953).
48. Progress in Semiconductors, Volume 2, edited by Alan F. Gibson, et al. London: Heywood & Company Ltd., 1957.
49. Raimes, Stanley. The Wave Mechanics of Electrons in Metals. New York: Interscience Publishers, Inc., 1961.
50. Ridgway, Stuart L. "The Use of a Lock-In Amplifier for the Detection and Measurement of Light Signals," Signal Notes, 1(1): 1-6 (November 1967). An aperiodic publication at a moderate dB level to discuss precision instrumentation for research from Princeton Applied Research Corporation, Princeton, N.J.
51. Shibata, Toshitaka, et al. "Passivation of Germanium Devices (III): Fabrication and Performance of Germanium Planar Photodiodes," Review of the Electrical Communication Laboratories, 22(11-12): 1069-1077 (November-December 1974).
52. Slater, J. C. and G. F. Koster. "Simplified LCAO Method for the Periodic Potential Problem." Physical Review, 94(6): 1498-1524 (June 15, 1954).
53. Sze, S. M. Physics of Semiconductor Devices. New York: John Wiley and Sons, Inc., 1969.
54. Takanashi, Hirobumi, et al. "Germanium Avalanche Photodetectors," Fujitsu Scientific & Technical Journal, 10(1): 119-134 (March 1974).
55. Van Roosbroeck, W. and W. Shockley. "Photon-Radiative Recombination of Electrons and Holes in Germanium," Physical Review, 94(6): 1558-1560 (June 15, 1954).
56. Wendland, P. H., et al. "Detectors: Inexpensive P-I-N Photodiodes Match Fiber, Source Characteristics," Electronics, 49(16): 101-102 (August 1976).

57. Yashiro, Takehisa, et al. "Passivation of Germanium Devices (II): The Electrical Properties of Ge-SiO<sub>2</sub> and Ge-Si<sub>3</sub>N<sub>4</sub> Interfaces, "Review of the Electrical Communication Laboratories, 22(11-12): 1057-1068 (November-December 1974).
58. Zwick, U., et al. "Low-loss Fibres for Wavelengths Beyond 1μm," Electronics Letters, 15(5): 159-160 (March 1, 1979).
59. Wang, Shyh. Solid State Electronics. New York: McGraw-Hill Book Company, 1966. (pp.169-177, 177-197).

## APPENDIX A

### Synchronous Detection

A Lock-In Voltmeter is substituted for the amplifier in Figure 30 and a chopper blade is inserted between the source and the photodetector (Ref 6; 26; 41; 50). The chopper blade rotates at constant speed and the detector produces a fluctuating voltage (A) at the input to the Lock-In Voltmeter as shown in Figure 45. In the Lock-In Voltmeter, the DC part of the signal is rejected. The remaining noise and square components are amplified which causes high level push-pull signals to be generated by the transformer, (C) and (D). The chopper blade is operated synchronously with the push-pull signals. The positive half cycles of the push-pull signals are mixed producing a full-wave rectified output (E) upon which a the noise is superimposed. The random noise almost cancels and an RC filter smooths out the DC output, the output of the Lock-In Voltmeter, (F) . The synchronous detector system is almost free from zero error and greater accuracy of measurements is obtained.

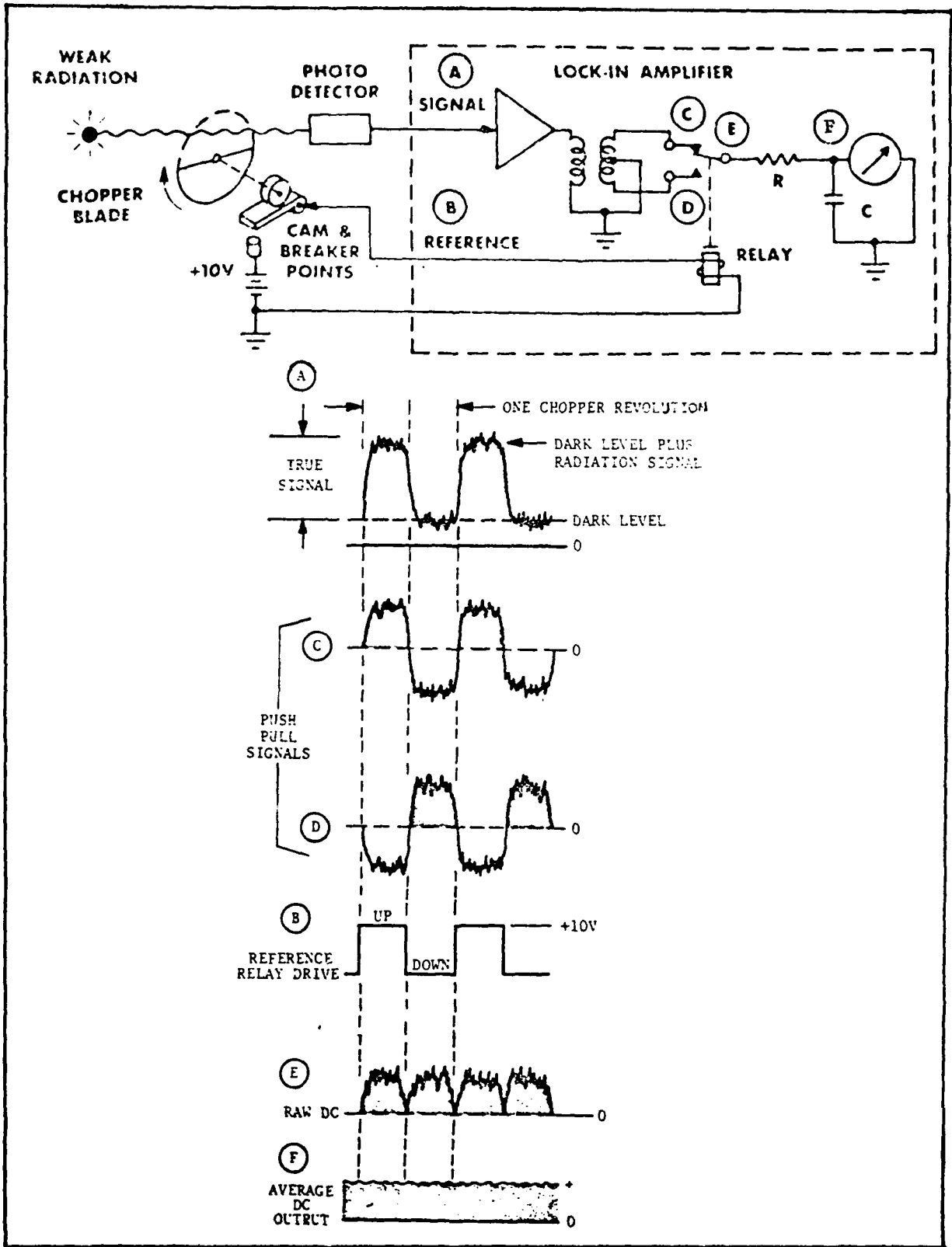


Fig 45. Application and operation of the lock-in-amplifier in a synchronous detection scheme (Ref 6; 26).

## APPENDIX B

### Experimental Procedure

#### Mounting the Chip for Testing

The steps for mounting a chip for testing can be followed using Figure 33 and are described here in more detail. Leads were soldered to the appropriate pins: 6, 9, 20, 23, and 15. The chip was placed vertically on the vacuum header and clamped facing the output slit of the monochromator as shown in Figure 46, i.e. in direct alignment with the light path of the radiant source. The cylindrical vacuum chamber was slipped over the header aligning the silicon glass input window with the window of the monochromator so that the sample could receive incident light. The leads from the chip were pulled through the circular hole in the back of the vacuum chamber as in Figure 47. Each labeled lead was inserted into its matching hole in the 5-pin socket of the connector with external coaxial output pins as shown in Figure 48. The connector was held in place with four screws and the "O" ring on the vacuum chamber formed the seal for the vacuum. The air-intake valve at the base of the vacuum chamber was securely closed and the main valve to the vacuum pump was opened to allow a vacuum to build up inside the chamber. The vacuum allowed the diode to operate in a protective environment without the influence of degrading factors in the ambient, such as dust and humidity. Recall that these diodes were not sealed in any way. Vacuum was allowed to reach  $10^{-4}$  torr ( $0.1 \mu\text{m Hg}$ ).

Once the sample was mounted in the header, a vacuum developed, and the globar warmed up to operating specifications (230 watts) photoresponse

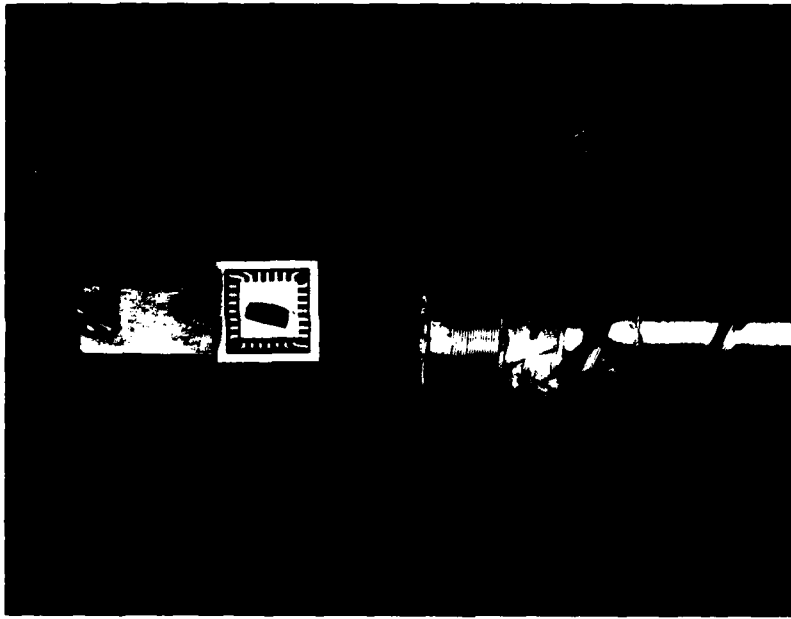


Fig 46. Mounting the sample on the vacuum header.

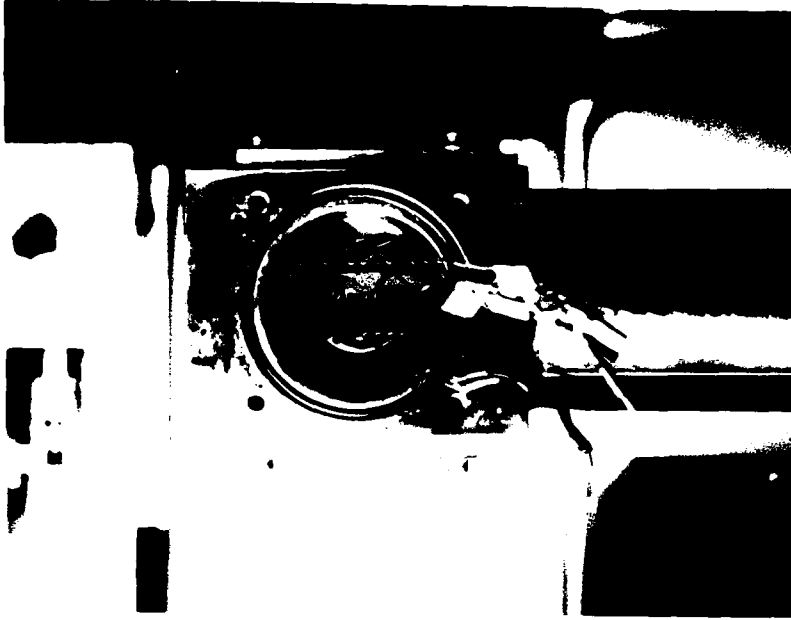


Fig 47. Pulling the leads through the back of the vacuum chamber. Photo shows the back of the header. The diode faces the window of the monochromator.



Fig 48. Photo showing the leads from the diode being inserted into a 5-pin socket of the connector with coaxial output pins.

measurements and diode characteristics could be taken on the device. Coaxial cables were used to connect each diode to a curve tracer to obtain the forward and reverse bias diode characteristics. A black cloth was draped over the header of the vacuum chamber to prevent ambient light from filtering into the chamber and to prevent the source from illuminating the sample during the check for device characteristics. The black cloth and coaxial cables were then removed from the header to perform photo-response measurements.

The cables from the preamplifier were attached to the connector to engage one of the photodiodes into the system(e.g. #23 and #15).

By turning the drum of the monochromator, it was possible to manually drive the optical prisms of the system so that the output radiation of the globar emitted light through a spectrum of wavelengths. These ranged from  $1.0\ \mu\text{m}$  to  $2.03\ \mu\text{m}$ . The silicon window on the vacuum header started to cut off wavelengths below  $1.0\ \mu\text{m}$ , that is, below  $1.0\ \mu\text{m}$  there was not 100% transmission.

#### Equipment Turn-On and Test Sequence

Before doing anything, the cooling water for the globar was turned on. The temperature dial at the top of the rack was set to room temperature,  $290^\circ\text{K}$ . The system has cooling capabilities, but these Ge diodes were meant to operate at room temperature. The globar power was checked to make sure the dial was turned all the way to the left, to zero. The power switch to the globar was turned on, set to 20V, and allowed to warm up slowly in 50-75 watt increments to 230 watts, where the source spectral characteristics are calibrated.

The oscillator and lock-in voltmeter were turned on. The KEPCO bias supply was set to 0 volts before being turned on. The digital voltmeter was used as a check to monitor the bias voltage. The digital recorder was set to standby and turned on. The function of the programmer was to set the speed of the chopper to 139 Hz. This frequency was chosen as the frequency with the lowest susceptibility to noise pick-up. The programmer was also set for the number of openings on the chopper wheel, six in this case.

The x-y staging was adjusted for maximum output. The maximum peak-to-peak output was observed on the oscilloscope and is explained using Figure 49. To synchronize the chopper speed with the lock-in voltmeter,

the latter was set to the calibrate mode. The chopper speed was trimmed to align the scope display to get a picture of a full-rectified wave as in Figure 49. Since the output of the Brower is always 0-10 volts, calibration was required for each scale. For example, if the input signal was between 0 and 25 mV, the maximum reading on the voltmeter would be 4 volts. More simply, the scaling is:

$$0 < \text{input signal} < 25 \text{ mV}$$

$$0 < \text{Brower output} < 10 \text{ V}$$

$$\text{input signal} = \frac{25 \text{ mV}}{10 \text{ V}} \times (\text{Brower output})$$

The gain on the lock-in voltmeter was turned to adjust the Brower output to its maximum and the calibration switch was turned to normal. To find the maximum p-p output, the phasing on the lock-in voltmeter is similar to the adjustment shown in Figure 49.

To take data, the programmer was put on hold and the data recorder on operate. Moving from high to low drum numbers in the back of the monochromator (so that the optics would work properly) as shown in Figure 50, the gate of the programmer was triggered by pushing the remote button to take data when ready. At the end of a run, the 5055 recorder was put on standby and the 3490 programmer was taken off hold to sample voltages at regular intervals.

#### Removing the Sample From the Evacuated Chamber.

After completion of the tests for a particular chip, the valve on the main line to the vacuum pump was closed to isolate the pump from the chamber. Air was admitted into the chamber by a valve at its base.

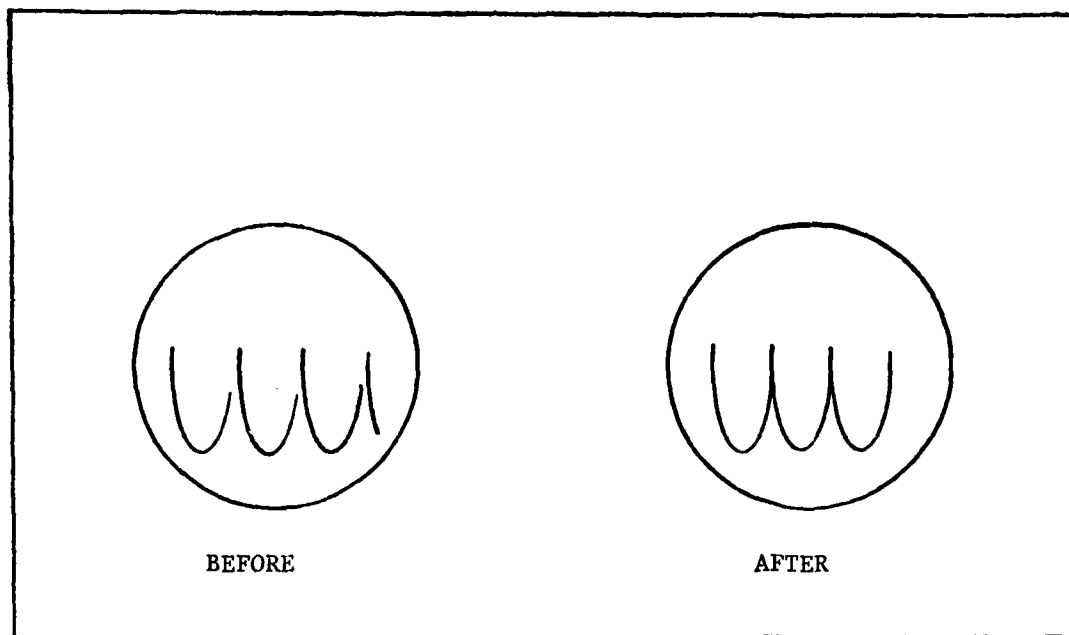


Fig 49. Adjusting trim to obtain display of full-rectified wave.



Fig 50. The rotating drum and remote switch used to scan the spectral output of the globar and trigger the data recorder.

The screws were removed from the measuring head which was carefully removed after separating the leads from the 5-pin socket. The vacuum chamber was removed by pulling straight up and the sample was removed from the holder by unscrewing the clamping screw.

Equipment Turn-Off Procedure.

All bias was removed from the diode after a test was completed; the KEPCO bias supply was turned off and set to zero as a precaution. The lock-in voltmeter, oscillator, and chopper wheel were turned off as well as all voltmeters and the digital recorder. The globar power was turned down slowly in 50 watt increments to prolong the life of the globar. Once the globar power was zero, it was switched off, and the system power turned off. The final step was to close the water valve for cooling the globar.

APPENDIX C

I-V Points Used to Plot the Diode Characteristics of Each Sample

TABLE C-1

Diode Characteristics of G-7-1 #9

Reverse Bias				Forward Bias	
V(V)	I( $\mu$ A)	V(V)	I( $\mu$ A)	V(V)	I( $\mu$ A)
0.05	3.3	2	6.5	0.05	7.5
0.10	4.5	3	7.0	0.10	17.0
0.15	4.8	4	7.5	0.15	30.0
0.20	5.0	5	8.0	0.20	40.0
0.25	5.1	10	10.0	1.0	250.0
0.30	5.2	15	12.0		
0.4	5.3	20	14.0		
0.5	5.4	25	16.0		
1.0	5.8				

TABLE C-2

## Diode Characteristics of G-7-4 #23

Reverse Bias				Forward Bias	
V(V)	I( $\mu$ A)	V(V)	I( $\mu$ A)	V(V)	I( $\mu$ A)
0.05	1.8	1.5	3.1	0.025	4.0
1.10	2.3	2.0	3.3	0.04	8.0
0.15	2.4	2.5	3.4	0.16	20.0
0.2-	2.5	3.0	3.6	0.35	40.0
0.25	2.55	3.5	3.75	0.60	60.0
0.30	2.55	4.0	3.9	0.75	80.0
0.35	2.6	5.0	4.1	0.95	100.0
0.40	2.7	6.0	4.3	1.10	120.0
0.50	2.7	7.0	4.6	1.35	140.0
0.60	2.75	10.0	5.3	1.35	150.0
0.70	2.75	15.0	6.7	1.60	200.0
0.80	2.8	20.0	9.0	1.85	250.0
1.0	3.0			2.00	300.0
1.2	3.0			2.20	350.0
1.4	3.1			2.3	400.0

TABLE C-3

## Diode Characteristics of G-8-1 #23

Reverse Bias				Forward Bias	
V(V)	I( $\mu$ A)	V(V)	I( $\mu$ A)	V(V)	I( $\mu$ A)
0.05	6.2	2.0	17.5	0.05	18.0
0.10	9.0	2.5	18.0	0.06	23.0
0.15	11.0	3.0	18.0	0.07	28.0
0.20	12.0	5.0	19.0	0.08	36.0
0.25	12.5	9.0	20.0	0.09	46.0
0.30	13.0	12.0	21.0	0.10	52.5
0.35	13.5	14.0	21.5	0.15	95.0
0.40	14.0	16.0	22.0	0.20	150.0
0.45	14.5	18.0	22.5	0.25	225.0
0.50	14.5	20.0	24.0	0.30	320.0
1.0	16.0	25.0	28.5	0.35	400.0
1.5	17.0				

TABLE C-4

Diode Characteristics of D-6-1 #6

Reverse Bias				Forward Bias	
V(V)	I( $\mu$ A)	V(V)	I( $\mu$ A)	V(V)	I( $\mu$ A)
0.05	1.17	2.8	1.8	0.02	1.5
0.10	1.5	3.0	1.85	0.04	3.8
0.2	1.6	3.5	1.9	0.05	5.0
0.4	1.65	4.0	2.05	0.06	6.0
0.8	1.65	4.5	2.25	0.08	10.0
1.0	1.65	5.0	2.5	0.10	14.0
1.2	1.7	6.0	2.8	0.12	19.0
1.4	1.7	8.0	4.5	0.14	24.0
1.6	1.7			0.16	30.0
1.8	1.7			0.18	37.0
2.0	1.7			0.2	50.0
				0.4	170.0
				0.6	470.0
				0.8	850.0
				1.0	1350.0

TABLE C-5

## Diode Characteristics of D-6-3 #6

Reverse Bias				Forward Bias	
V(V)	I( $\mu$ A)	V(V)	I( $\mu$ A)	V(V)	I( $\mu$ A)
0.05	2.75	27.5	6.0	0.01	1.0
0.10	3.1	30.0	6.3	0.02	2.0
0.15	4.6	32.5	7.0	0.03	3.6
0.20	5.0	35.0	8.0	0.04	5.6
0.25	5.2	37.5	10.0	0.05	7.5
0.30	5.3	40.0	20.0	0.06	9.5
0.35	5.35			0.07	13.0
0.40	5.4			0.08	18.0
0.45	5.4			0.09	24.0
4.5	5.5			0.10	33.0
20.0	5.6			0.15	135.0
25.0	5.8			0.25	660.0

APPENDIX D

Output Voltages Recorded Across the 100K Resistor for Each Test Run

TABLE D-1

Output Photovoltage of G-7-1 #9 for H\* Calibration Data

$\lambda$ ( $\mu\text{m}$ )	0V Bias V( $\mu\text{V}$ )	5V Bias V( $\mu\text{V}$ )	10V Bias V( $\mu\text{V}$ )
1.04	170	2625	2775
1.11	1256	19450	19950
1.19	3057	48950	51125
1.28	4517	74300	76175
1.37	5794	97150	98425
1.46	7173	123550	125075
1.55	6965	119925	122300
1.65	5388	90100	91325
1.75	4214	68400	69575
1.85	2567	41475	41775
2.03	114	1950	1925

TABLE D-2

Output Photovoltage of G-7-1 #9 for H\*\* Calibration Data

$\lambda$ ( $\mu\text{m}$ )	0V Bias V( $\mu\text{V}$ )	5V Bias V( $\mu\text{V}$ )	10V Bias V( $\mu\text{V}$ )
1.04	188	2825	2950
1.11	1282	20300	20700
1.19	2976	50350	50125
1.28	4296	75950	75025
1.37	5452	98900	97675
1.46	6596	122225	120550
1.55	6342	117150	115725
1.65	6342	86800	86850
1.75	3948	66450	65950
1.85	2622	42600	42000
2.03	134	2000	2150

TABLE D-3

Output Photovoltage of G-7-4 #23 for H\* Calibration Data

$\lambda$ ( $\mu\text{m}$ )	0V Bias V( $\mu\text{V}$ )	5V Bias V( $\mu\text{V}$ )	10V Bias V( $\mu\text{V}$ )
1.04	1185	8350	8175
1.11	6988	54275	54000
1.19	14343	135275	133450
1.28	19570	202250	199925
1.37	23718	260600	260500
1.46	27610	327750	324700
1.55	25853	295600	298450
1.65	19383	192525	197025
1.75	14300	126700	125450
1.85	8063	66625	67300
2.03	318	2725	2775

TABLE D-4

Output Photovoltage of G-7-4 #23 for H\*\* Calibration Data

$\lambda$ ( $\mu\text{m}$ )	0V Bias V( $\mu\text{V}$ )	5V Bias V( $\mu\text{V}$ )	10V Bias V( $\mu\text{V}$ )
1.04	655	11050	11600
1.11	4065	72500	76100
1.19	8950	174500	179800
1.28	12465	261700	270150
1.37	15395	338450	349600
1.46	17948	419250	431100
1.55	16750	379000	387650
1.65	11978	246450	250800
1.75	8273	159450	163650
1.85	4575	81050	82900
2.03	168	2750	2800

TABLE D-5

Output Photovoltage of G-8-1 #23 for H\* Calibration Data

$\lambda$ ( $\mu\text{m}$ )	0V Bias V( $\mu\text{V}$ )	5V Bias V( $\mu\text{V}$ )	10V Bias V( $\mu\text{V}$ )
1.04	216	5300	5575
1.11	1441	36450	38925
1.19	3573	95200	100075
1.28	5500	148725	157850
1.37	7329	203975	212400
1.46	9459	256525	281050
1.55	9838	281525	296500
1.65	8135	228450	239200
1.75	5846	162825	171825
1.85	3531	94800	99125
2.03	195	4975	5025

TABLE D-6

Output Photovoltage of G-8-1 #23 for H\*\* Calibration Data

$\lambda$ ( $\mu\text{m}$ )	0V Bias V( $\mu\text{V}$ )	5V Bias V( $\mu\text{V}$ )	10V Bias V( $\mu\text{V}$ )
1.04	165	3550	4000
1.11	1261	30600	31900
1.19	3205	81250	85750
1.28	4995	130950	137400
1.37	6603	178400	184550
1.46	8396	234100	244650
1.55	8838	249250	258550
1.65	7459	203050	211700
1.75	5544	145900	148700
1.85	3171	80850	83550
2.03	156	3550	3750

TABLE D-7

Output Photovoltage of D-6-1 #6 for H\* Calibration Data

$\lambda$ ( $\mu\text{m}$ )	0V Bias V( $\mu\text{V}$ )	5V Bias V( $\mu\text{V}$ )	10V Bias V( $\mu\text{V}$ )
1.04	830	3525	1425
1.11	5565	26975	22375
1.19	12995	71025	59125
1.28	18515	110850	91550
1.37	23055	148625	122100
1.46	28080	195950	162500
1.55	28205	201025	167650
1.65	22895	152050	126975
1.75	16650	102950	84500
1.85	8895	48400	41550
2.03	360	1650	1725

TABLE D-8

Output Photovoltage of D-6-1 #6 for H\*\* Calibration Data

$\lambda$ ( $\mu\text{m}$ )	0V Bias V( $\mu\text{V}$ )	5V Bias V( $\mu\text{V}$ )	10V Bias V( $\mu\text{V}$ )
1.04	755	5000	4450
1.11	4695	35250	32700
1.19	10470	87800	81450
1.28	14660	131900	723100
1.37	18080	173650	161500
1.46	21375	218950	203750
1.55	21145	221450	206100
1.65	17010	170150	160150
1.75	12370	116750	108200
1.85	7260	62950	58500
2.03	345	2600	2050

TABLE D-9

Output Photovoltage of D-6-3 #6 for H\* Calibration Data

$\lambda$ ( $\mu\text{m}$ )	0V Bias V( $\mu\text{V}$ )	5V Bias V( $\mu\text{V}$ )	10V Bias V( $\mu\text{V}$ )
1.04	1090	10000	10350
1.11	6580	64500	64650
1.19	14407	152200	154400
1.28	20235	227300	229950
1.37	24790	294800	297500
1.46	29217	370450	374050
1.55	28597	365950	368800
1.65	22277	279000	280750
1.75	15997	192800	194850
1.85	8992	99800	102050
2.03	400	4200	4250

TABLE D-10

Output Photovoltage of D-6-3 #6 for H\*\* Calibration Data

$\lambda$ ( $\mu\text{m}$ )	0V Bias V( $\mu\text{V}$ )	5V Bias V( $\mu\text{V}$ )	10V Bias V( $\mu\text{V}$ )
1.04	470	10650	11050
1.11	3203	73350	72700
1.19	7328	176000	175400
1.28	10673	263250	261400
1.37	13340	343400	340400
1.46	15908	424200	414300
1.55	15238	414500	422850
1.65	11125	310900	309200
1.75	7573	214100	214350
1.85	4243	116550	115750
2.03	158	4450	4500

APPENDIX E

Photocurrent, Incident Optical Power, Responsivity, and Quantum Efficiency of Each Sample per Test Run

TABLE E-1

Photocharacteristics of G-7-1 #9 at 0.1mV for H\* Calibration Data

$\lambda$ ( $\mu\text{m}$ )	I ( $\mu\text{A}$ )	H ( $\mu\text{W}$ )	R ( $\mu\text{A}/\mu\text{W}$ )	$\eta$ (%)
1.04	0.00170	0.059	0.029	3.4
1.11	0.01256	0.295	0.043	4.8
1.19	0.03057	0.648	0.047	4.9
1.28	0.04517	0.912	0.050	4.8
1.37	0.05794	1.104	0.052	4.8
1.46	0.07173	1.357	0.053	4.5
1.55	0.06965	1.521	0.046	3.7
1.65	0.05388	1.616	0.033	2.5
1.75	0.04214	1.640	0.026	1.8
1.85	0.02567	1.583	0.162	1.1
2.03	0.00114	1.621	0.001	

TABLE E-2

Photocharacteristics of G-7-1 #9 at 5V for H\* Calibration Data

$\lambda$ ( $\mu\text{m}$ )	I ( $\mu\text{A}$ )	H ( $\mu\text{W}$ )	R ( $\mu\text{A}/\mu$ )	$\eta$ (%)
1.04	0.02625	0.059	0.445	53.0
1.11	0.19450	0.295	0.659	73.7
1.19	0.48950	0.648	0.755	78.7
1.28	0.74300	0.912	0.815	78.9
1.37	0.97150	1.104	0.880	79.6
1.46	1.23550	1.357	0.910	77.3
1.55	1.19925	1.521	0.788	63.1
1.65	0.90100	1.616	0.558	41.9
1.75	0.68400	1.640	0.417	29.6
1.85	0.41475	1.583	0.262	17.6
2.03	0.01950	1.621	0.120	7.3

TABLE E-3

Photocharacteristics of G-7-1 #9 at 10V for H\* Calibration Data

$\lambda$ ( $\mu\text{m}$ )	I ( $\mu\text{A}$ )	H ( $\mu\text{W}$ )	R ( $\mu\text{A}/\mu\text{W}$ )	$\eta$ (%)
1.04	0.02775	0.059	0.470	56.1
1.11	0.19950	0.295	0.676	75.5
1.19	0.51125	0.648	0.789	82.2
1.28	0.76175	0.912	0.835	80.9
1.37	0.98425	1.104	0.892	80.7
1.46	1.25075	1.357	0.922	78.3
1.55	1.22300	1.521	0.804	64.3
1.65	0.91325	1.616	0.565	42.5
1.75	0.69575	1.640	0.424	30.1
1.85	0.41775	1.583	0.264	17.7
2.03	0.01925	1.621	0.012	0.7

TABLE E-4

Photocharacteristics of G-7-1 #9 at 0V for H\*\* Calibration Data

$\lambda$ ( $\mu\text{m}$ )	I ( $\mu\text{A}$ )	H ( $\mu\text{W}$ )	R ( $\mu\text{A}/\mu\text{W}$ )	$\eta$ (%)
1.04	0.00188	0.0464	0.041	4.8
1.11	0.01282	0.2998	0.043	4.8
1.19	0.02976	0.6460	0.046	4.8
1.28	0.04296	0.9225	0.047	4.5
1.37	0.05452	1.0893	0.050	4.5
1.46	0.06596	1.3152	0.050	4.3
1.55	0.06342	1.4671	0.043	3.5
1.65	0.04886	1.5410	0.032	2.4
1.75	0.03948	1.5664	0.025	1.8
1.85	0.02622	1.5057	0.017	1.2
2.03	0.00134	1.5368	0.001	

TABLE E-5

Photocharacteristics of G-7-1 #9 at 5V for H\*\* Calibration Data

$\lambda$ ( $\mu\text{m}$ )	I ( $\mu\text{A}$ )	H ( $\mu\text{W}$ )	R ( $\mu\text{A}/\mu\text{W}$ )	$\eta$ (%)
1.04	0.02825	0.0464	0.615	72.5
1.11	0.20300	0.2998	0.677	75.6
1.19	0.50350	0.6460	0.779	81.2
1.28	0.75950	0.9225	0.823	79.7
1.37	0.98900	1.0893	0.908	82.2
1.46	1.22225	1.3152	0.929	78.9
1.55	1.17150	1.4671	0.799	63.9
1.65	0.86800	1.5410	0.563	42.3
1.75	0.66450	1.5664	0.424	30.0
1.85	0.42600	1.5051	0.283	19.0
2.03	0.02000	1.5368	0.013	.79

TABLE E-6

Photocharacteristics of G-7-1 #9 at 10V for H\*\* Calibration Data

$\lambda$ ( $\mu\text{m}$ )	I ( $\mu\text{A}$ )	H ( $\mu\text{W}$ )	R ( $\mu\text{A}/\mu\text{W}$ )	$\eta$ (%)
1.04	0.02950	0.0464	0.636	75.8
1.11	0.20700	0.2998	0.695	77.1
1.19	0.50125	0.6460	0.776	80.9
1.28	0.75025	0.9225	0.813	78.8
1.37	0.97675	1.0893	0.897	81.2
1.46	1.20550	1.3152	0.917	77.8
1.55	1.15725	1.4671	0.789	63.1
1.65	0.86850	1.5410	0.564	42.4
1.75	0.65950	1.5664	0.438	31.0
1.85	0.42000	1.5051	0.279	18.7
2.03	0.02150	1.5368	0.014	0.9

TABLE E-7

Photocharacteristics of G-7-4 #23 at 0V for H\* Calibration Data

$\lambda$ ( $\mu\text{m}$ )	I ( $\mu\text{A}$ )	H ( $\mu\text{W}$ )	R ( $\mu\text{A}/\mu\text{W}$ )	$\eta$ (%)
1.04	0.00655	0.0285	0.230	27.4
1.11	0.04065	0.1840	0.221	24.7
1.19	0.08950	0.3966	0.226	23.5
1.28	0.12465	0.5664	0.220	21.3
1.37	0.15395	0.6687	0.230	20.8
1.46	0.17948	0.8074	0.222	18.9
1.55	0.16750	0.9007	0.186	14.9
1.65	0.11978	0.9461	0.127	9.5
1.75	0.08273	0.9616	0.086	6.1
1.85	0.04575	0.9241	0.050	3.4
2.03	0.00168	0.9435	0.002	.12

TABLE E-8

Photocharacteristics of G-7-4 #23 at 5V for H\* Calibration Data

$\lambda$ ( $\mu\text{m}$ )	I ( $\mu\text{A}$ )	H ( $\mu\text{W}$ )	R ( $\mu\text{A}/\mu\text{W}$ )	R' ( $\mu\text{A}/\mu\text{W}$ )	$\eta$ (%)	$\eta'$ (%)
1.04	0.11050	0.0285	0.3877	0.7466	46.2	100.0
1.11	0.72500	0.1840	0.3940	0.7587	44.0	95.2
1.19	1.74500	0.3966	0.4400	0.8473	45.8	99.1
1.28	2.61700	0.5664	0.4620	0.8897	44.8	97.0
1.37	3.38450	0.6687	0.5061	0.9746	45.8	99.1
1.46	4.19250	0.8074	0.5193	1.0000	44.1	96.1
1.55	3.79000	0.9007	0.4694	0.9039	39.9	86.4
1.65	2.46450	0.9461	0.2605	0.5016	19.6	42.4
1.75	1.59450	0.9616	0.1658	0.3193	11.7	25.3
1.85	0.81050	0.9241	0.0877	0.1689	5.9	12.8
2.03	0.02750	0.9435	0.029	0.0558	0.2	0.4

TABLE E-9

Photocharacteristics of G-7-4 #23 at 10V for H\* Calibration Data

$\lambda$ ( $\mu\text{m}$ )	I ( $\mu\text{A}$ )	H ( $\mu\text{W}$ )	R ( $\mu\text{A}/\mu\text{W}$ )	R' ( $\mu\text{A}/\mu\text{W}$ )	$\eta$ (%)	$\eta'$ (%)
1.04	0.11600	0.0285	0.4070	0.7623	48.5	100.0
1.11	0.76100	0.1840	0.4136	0.7747	46.2	95.3
1.19	1.79800	0.3966	0.4533	0.8490	47.2	97.3
1.28	2.70150	0.5664	0.4770	0.8934	46.2	95.3
1.37	3.49600	0.6687	0.5228	0.9792	47.3	97.5
1.46	5.31100	0.8074	0.5339	1.0000	45.3	93.4
1.55	3.87650	0.9007	0.4304	0.8061	34.4	70.9
1.65	2.50800	0.9461	0.2651	0.4965	19.9	41.0
1.75	1.63650	0.9616	0.1702	0.3188	12.1	24.9
1.85	0.82900	0.9241	0.0897	0.1680	6.0	12.4
2.03	0.02800	0.9435	0.0030	0.0056	.2	0.4

TABLE E-10

Photocharacteristics of G-7-4 #23 at 0.1mV for H\*\* Calibration Data

$\lambda$ ( $\mu\text{m}$ )	I ( $\mu\text{A}$ )	H ( $\mu\text{W}$ )	R ( $\mu\text{A}/\mu\text{W}$ )	$\eta$ (%)
1.04	0.01185	0.0356	0.332	39.7
1.11	0.06988	0.1778	0.393	43.9
1.19	0.14343	0.3899	0.368	38.3
1.28	0.19570	0.5486	0.357	34.6
1.37	0.23718	0.6642	0.357	32.3
1.46	0.27610	0.8166	0.338	28.7
.55	0.25853	0.9157	0.282	22.6
1.65	0.19383	0.9728	0.199	15.0
1.75	0.14300	0.9868	0.145	10.3
1.85	0.08063	0.9525	0.085	5.7
2.03	0.00318	0.9754	0.003	0.2

TABLE E-11

Photocharacteristics of G-7-4 #23 at 5V for H\*\* Calibration Data

$\lambda$ ( $\mu\text{m}$ )	I ( $\mu\text{A}$ )	H ( $\mu\text{W}$ )	R ( $\mu\text{A}/\mu\text{W}$ )	R' ( $\mu\text{A}/\mu\text{W}$ )	$\eta$ (%)	$\eta'$ (%)
1.04	0.08350	0.0356	2.345	0.584	280	77
1.11	0.54275	0.1778	3.053	0.761	341	94
1.19	1.35275	0.3899	3.469	0.864	362	100
1.28	2.02250	0.5486	3.687	0.919	357	99
1.37	2.60600	0.6642	3.924	0.978	355	98
1.46	3.27750	0.8166	4.014	1.000	341	94
1.55	2.95600	0.9157	3.228	0.804	258	71
1.65	1.92525	0.9728	1.979	0.493	149	41
1.75	1.26700	0.9868	1.284	0.320	90	25
1.85	0.66625	0.9525	0.699	0.174	47	13
2.03	0.02725	0.9754	0.028	0.007	2	1

TABLE E-12

Photocharacteristics of G-7-4 #23 at 10V for H\*\* Calibration Data

$\lambda$ ( $\mu\text{m}$ )	I ( $\mu\text{A}$ )	H ( $\mu\text{W}$ )	R ( $\mu\text{A}/\mu\text{W}$ )	R' ( $\mu\text{A}/\mu\text{W}$ )	$\eta$ (%)	$\eta'$ (%)
1.04	0.08175	0.0356	2.296	0.577	274	77
1.11	0.54000	0.1778	3.037	0.764	339	95
1.19	1.33450	0.3899	3.423	0.861	357	100
1.28	1.99925	0.5486	3.644	0.916	353	99
1.37	2.60500	0.6642	3.922	0.986	355	99
1.46	3.24700	0.8166	3.976	1.000	338	95
1.55	2.98450	0.9157	3.259	0.820	261	73
1.65	1.97025	0.9728	2.025	0.509	152	43
1.75	1.25450	0.9868	1.271	0.320	90	25
1.85	0.67300	0.9525	0.707	0.118	47	13
2.03	0.02775	0.9754	0.028	0.007	2	1

TABLE E-13

Photocharacteristics of G-8-1 #23 at 0V for H\* Calibration Data

$\lambda$ ( $\mu\text{m}$ )	I ( $\mu\text{A}$ )	H ( $\mu\text{W}$ )	R ( $\mu\text{A}/\mu\text{W}$ )	$\eta$ (%)
1.04	0.00216	0.181	0.012	1.4
1.11	0.01441	0.907	0.016	1.8
1.19	0.03573	1.989	0.018	1.9
1.28	0.05500	2.799	0.020	1.9
1.37	0.07329	3.389	0.022	2.0
1.46	0.09459	4.167	0.023	1.9
1.55	0.09838	4.672	0.021	1.7
1.65	0.08135	4.964	0.016	1.2
1.75	0.05846	5.035	0.012	0.8
1.85	0.03531	4.860	0.007	0.5
2.03	0.00195	4.977		

TABLE E-14

Photocharacteristics of G-8-1 #23 at 5V for H\* Calibration Data

$\lambda$ ( $\mu\text{m}$ )	I ( $\mu\text{A}$ )	H ( $\mu\text{W}$ )	R ( $\mu\text{A}/\mu\text{W}$ )	$\eta$ (%)
1.04	0.05300	0.181	0.293	34.9
1.11	0.36450	0.907	0.402	44.9
1.19	0.95200	1.989	0.479	49.9
1.28	1.48725	2.799	0.531	51.5
1.37	2.03975	3.389	0.602	54.5
1.46	2.56525	4.167	0.616	52.3
1.55	2.81525	4.672	0.603	48.2
1.65	2.28450	4.964	0.460	34.6
1.75	1.62825	5.035	0.323	22.9
1.85	0.94800	4.860	0.195	13.1
2.03	0.04975	4.977	0.010	0.6

TABLE E-15

Photocharacteristics of G-8-1 #23 at 10V for H\* Calibration Data

$\lambda$ ( $\mu\text{m}$ )	I ( $\mu\text{A}$ )	H ( $\mu\text{W}$ )	R ( $\mu\text{A}/\mu\text{W}$ )	$\eta$ (%)
1.04	0.05575	0.181	0.308	36.7
1.11	0.38925	0.907	0.429	47.9
1.19	1.00075	1.989	0.503	52.4
1.28	1.57850	2.799	0.564	54.6
1.37	2.12400	3.389	0.627	56.7
1.46	2.81050	4.167	0.674	57.3
1.55	2.96500	4.672	0.635	50.8
1.65	2.39200	4.964	0.482	36.2
1.75	1.71825	5.035	0.341	24.2
1.85	0.99125	4.860	0.204	13.7
2.03	0.05025	4.977	0.001	0.1

TABLE E-16

Photocharacteristics of G-8-1 #23 at 0V for H\*\* Calibration Data

$\lambda$ ( $\mu\text{m}$ )	I ( $\mu\text{A}$ )	H ( $\mu\text{W}$ )	R ( $\mu\text{A}/\mu\text{W}$ )	$\eta$ (%)
1.04	0.00165	0.1426	0.012	1.4
1.11	0.01261	0.9206	0.014	1.5
1.19	0.03205	1.9838	0.016	1.7
1.28	0.04995	2.8331	0.018	1.7
1.37	0.06603	3.3452	0.020	1.8
1.46	0.08396	4.0389	0.021	1.8
1.55	0.08838	4.5057	0.020	1.6
1.65	0.07459	4.7326	0.016	1.2
1.75	0.05544	4.8104	0.012	0.8
1.85	0.03171	4.6224	0.007	0.5
2.03	0.00156	4.7196		

TABLE E-17

Photocharacteristics of G-8-1 #23 at 5V for H\*\* Calibration Data

$\lambda$ ( $\mu\text{m}$ )	I ( $\mu\text{A}$ )	H ( $\mu\text{W}$ )	R ( $\mu\text{A}/\mu\text{W}$ )	$\eta$ (%)
1.04	0.03550	0.1426	0.249	29.7
1.11	0.30600	0.9206	0.332	37.1
1.19	0.81250	1.9838	0.410	42.7
1.28	1.30950	2.8331	0.462	44.8
1.37	1.78400	3.3452	0.533	48.3
1.46	2.34100	4.0389	0.570	49.2
1.55	2.49250	4.5057	0.553	44.3
1.65	2.03050	4.7326	0.429	32.2
1.75	1.45900	4.8104	0.303	21.5
1.85	0.80850	4.6224	0.175	11.7
2.03	0.03550	4.7196	0.008	0.5

TABLE E-18

Photocharacteristics of G-8-1 #23 at 10V for H\*\* Calibration Data

$\lambda$ ( $\mu\text{m}$ )	I ( $\mu\text{A}$ )	H ( $\mu\text{W}$ )	R ( $\mu\text{A}/\mu\text{W}$ )	$\eta$ (%)
1.04	0.04000	0.1426	0.281	33.5
1.11	0.31900	0.9206	0.347	38.7
1.19	0.85750	1.9838	0.432	45.0
1.28	1.37400	2.8331	0.485	47.0
1.37	1.84550	3.3452	0.552	50.0
1.46	2.44650	4.0389	0.606	51.4
1.55	2.58550	4.5057	0.574	46.0
1.65	2.11700	4.7326	0.447	33.6
1.75	1.48700	4.8104	0.309	21.9
1.85	0.83550	4.6224	0.177	11.9
2.03	0.03750	4.7196	0.008	0.5

TABLE E-19

Photocharacteristics of D-6-1 #6 at 0V for H\* Calibration Data

$\lambda$ ( $\mu\text{m}$ )	I ( $\mu\text{A}$ )	H ( $\mu\text{W}$ )	R ( $\mu\text{A}/\mu\text{W}$ )	$\eta$ (%)
1.04	0.00083	0.052	0.0160	1.9
1.11	0.05565	0.258	0.2157	24.1
1.19	0.12995	0.565	0.2300	24.0
1.28	0.18515	0.795	0.2329	22.6
1.37	0.23055	0.962	0.2397	21.7
1.46	0.28080	1.183	0.2374	20.2
1.55	0.28205	1.327	0.2125	17.0
1.65	0.22895	1.409	0.1625	12.2
1.75	0.16650	1.430	0.1164	8.3
1.85	0.08895	1.380	0.0645	4.3
2.03	0.00360	1.413	0.0025	0.2

TABLE E-20

Photocharacteristics of D-7-1 #6 at 5V for H\* Calibration Data

$\lambda$ ( $\mu\text{m}$ )	I ( $\mu\text{A}$ )	H ( $\mu\text{W}$ )	R ( $\mu\text{A}/\mu\text{W}$ )	R' ( $\mu\text{A}/\mu\text{W}$ )	$\eta$ (%)	$\eta'$ (%)
1.04	0.03525	0.052	0.6779	0.409	81	57
1.11	0.26975	0.258	1.046	0.632	117	83
1.19	0.71025	0.565	1.257	0.759	131	93
1.28	1.10850	0.795	1.394	0.842	135	99
1.37	1.48625	0.962	1.545	0.933	140	100
1.46	1.95950	1.183	1.656	1.000	141	86
1.55	2.01025	1.327	1.515	0.915	121	57
1.65	1.52050	1.409	1.079	0.652	81	36
1.75	1.02950	1.430	0.720	0.435	51	17
1.85	0.48400	1.380	0.357	0.212	24	5
2.03	0.01650	1.413	0.012	0.007	7	

TABLE E-21

Photocharacteristics of D-6-1 #6 at 10V for H\* Calibration Data

$\lambda$ ( $\mu\text{m}$ )	I ( $\mu\text{A}$ )	H ( $\mu\text{W}$ )	R ( $\mu\text{A}/\mu\text{W}$ )	R' ( $\mu\text{A}/\mu\text{W}$ )	$\eta$ (%)	$\eta'$ (%)
1.04	0.01425	0.052	0.274	0.199	33	28
1.11	0.22375	0.258	0.867	0.631	97	83
1.19	0.59125	0.565	1.046	0.761	109	93
1.28	0.91550	0.795	1.152	0.838	112	96
1.37	1.22100	0.962	1.269	0.924	115	98
1.46	1.62500	1.183	1.374	1.000	117	100
1.55	1.67650	1.327	1.263	0.919	101	86
1.65	1.26975	1.409	0.901	0.656	68	58
1.75	0.84500	1.430	0.591	0.430	42	36
1.85	0.41550	1.380	0.301	0.219	20	17
2.03	0.01725	1.413	0.012	0.009	1	1

TABLE E-22

Photocharacteristics of D-6-1 #6 at 0V for H\*\* Calibration Data

$\lambda$ ( $\mu\text{m}$ )	I ( $\mu\text{A}$ )	H ( $\mu\text{W}$ )	R ( $\mu\text{A}/\mu\text{W}$ )	$\eta$ (%)
1.04	0.00755	0.0405	0.1864	14.5
1.11	0.04695	0.2613	0.1798	20.1
1.19	0.10470	0.5630	0.1860	19.4
1.28	0.14660	0.8041	0.1823	17.7
1.37	0.18080	0.9494	0.1904	17.2
1.46	0.21375	1.1463	0.1865	15.8
1.55	0.21145	1.2788	0.1653	13.2
1.65	0.17010	1.3432	0.1266	9.5
1.75	0.12370	1.3653	0.0906	6.4
1.85	0.07260	1.3119	0.0553	3.7
2.03	0.00345	1.3395	0.0026	0.2

TABLE E-23

Photocharacteristics of D-6-1 #6 at 5V for H\*\* Calibration Data

$\lambda$ ( $\mu\text{m}$ )	I ( $\mu\text{A}$ )	H ( $\mu\text{W}$ )	R ( $\mu\text{A}/\mu\text{W}$ )	R' ( $\mu\text{A}/\mu\text{W}$ )	$\eta$ (%)	$\eta'$ (%)
1.04	0.05000	0.0405	1.2346	0.6464	147	89
1.11	0.35250	0.2613	1.3490	0.7062	151	91
1.19	0.87800	0.5630	1.5600	0.8167	163	98
1.28	1.31900	0.8041	1.6403	0.8588	159	96
1.37	1.73650	0.9494	1.8290	0.9575	166	100
1.46	2.18950	1.1463	1.9101	1.0000	162	98
1.55	2.21450	1.2788	1.7317	0.9066	139	84
1.65	1.70150	1.3432	1.2668	0.6632	95	57
1.75	1.16750	1.3653	0.8551	0.4477	61	37
1.85	0.62950	1.3119	0.4798	0.2512	32	19
2.03	0.02600	1.3395	0.0194	0.0102	1	1

TABLE E-24

Photocharacteristics of D-6-1 #6 at 10V for H\*\* Calibration Data

$\lambda$ ( $\mu\text{m}$ )	I ( $\mu\text{A}$ )	H ( $\mu\text{W}$ )	R ( $\mu\text{A}/\mu\text{W}$ )	R' ( $\mu\text{A}/\mu\text{W}$ )	$\eta$ (%)	$\eta'$ (%)
1.04	0.04450	0.0405	1.0988	0.6182	131	85
1.11	0.32700	0.2613	1.2514	0.7040	140	91
1.19	0.81450	0.5630	1.4467	0.8139	151	98
1.28	1.23100	0.8041	1.5309	0.8613	148	96
1.37	1.61500	0.9464	1.7011	0.9570	154	100
1.46	2.03750	1.1463	1.7775	1.0000	151	90
1.55	2.06100	1.2788	1.6117	0.9067	129	84
1.65	1.60150	1.3432	1.1923	0.6708	90	58
1.75	1.08200	1.3653	0.7925	0.4459	56	36
1.85	0.58500	1.3119	0.4459	0.2509	30	19
2.03	0.02050	1.3395	0.0153	0.0086	1	1

TABLE E-25

Photocharacteristics of D-6-3 #6 at 0V for H\* Calibration Data

$\lambda$ ( $\mu\text{m}$ )	I ( $\mu\text{A}$ )	H ( $\mu\text{W}$ )	R ( $\mu\text{A}/\mu\text{W}$ )	$\eta$ (%)
1.04	0.01090	0.052	0.2096	25.0
1.11	0.06580	0.258	0.2550	28.5
1.19	0.14407	0.565	0.2550	26.6
1.28	0.20235	0.795	0.2545	24.7
1.37	0.24790	0.962	0.2577	23.3
1.46	0.29217	1.183	0.2470	21.0
1.55	0.28597	1.327	0.2155	17.2
1.65	0.22277	1.409	0.1581	11.9
1.75	0.15997	1.430	0.1119	6.4
1.85	0.08992	1.380	0.0652	4.4
2.03	0.00400	1.413	0.0028	0.2

TABLE E-26

Photocharacteristics of D-6-3 #6 at 5V for H\* Calibration Data

$\lambda$ ( $\mu\text{m}$ )	I ( $\mu\text{A}$ )	H ( $\mu\text{W}$ )	R ( $\mu\text{A}/\mu\text{W}$ )	R' ( $\mu\text{A}/\mu\text{W}$ )	$\eta$ (%)	$\eta'$ (%)
1.04	0.10000	0.052	1.923	0.614	229	81
1.11	0.64500	0.258	2.500	0.798	279	99
1.19	1.52200	0.565	2.694	0.860	281	100
1.28	2.27300	0.795	2.859	0.913	277	98
1.37	2.94800	0.962	3.064	0.979	277	98
1.46	3.70450	1.183	3.131	1.000	266	95
1.55	3.65950	1.327	2.758	0.881	221	79
1.65	2.79000	1.409	1.980	0.632	149	53
1.75	1.92800	1.403	1.374	0.439	97	35
1.85	0.99800	1.380	0.723	0.231	48	17
2.03	0.04200	1.413	0.030	0.010	2	1

TABLE E-27

Photocharacteristics of D-6-3 #6 at 10V for H\* Calibration Data

$\lambda$ ( $\mu\text{m}$ )	I ( $\mu\text{A}$ )	H ( $\mu\text{W}$ )	R ( $\mu\text{A}/\mu\text{W}$ )	R' ( $\mu\text{A}/\mu\text{W}$ )	$\eta$ (%)	$\eta'$ (%)
1.04	0.10350	0.052	1.990	0.629	237	83
1.11	0.64650	0.258	2.506	0.793	280	98
1.19	1.54400	0.565	2.733	0.864	285	100
1.28	2.29950	0.795	2.892	0.915	280	98
1.37	2.97500	0.962	3.093	0.978	280	98
1.46	3.74050	1.183	3.162	1.000	269	94
1.55	3.68800	1.327	2.779	0.879	222	78
1.65	2.80750	1.409	1.993	0.630	150	53
1.75	1.94850	1.430	1.363	0.431	97	34
1.85	1.02050	1.380	0.739	0.234	50	18
2.03	0.04250	1.413	0.030	0.009	2	1

TABLE E-28

Photocharacteristics of D-6-3 #6 at 0V for H\*\* Calibration Data

$\lambda$ ( $\mu\text{m}$ )	I ( $\mu\text{A}$ )	H ( $\mu\text{W}$ )	R ( $\mu\text{A}/\mu\text{W}$ )	$\eta$ (%)
1.04	0.00470	0.0405	0.1160	13.8
1.11	0.03203	0.2613	0.1226	13.7
1.19	0.07328	0.5630	0.1302	13.6
1.28	0.10673	0.8041	0.1327	12.9
1.37	0.13340	0.9494	0.1405	12.7
1.46	0.15908	1.1463	0.1388	11.8
1.55	0.15238	1.2788	0.1192	9.5
1.65	0.11125	1.3432	0.0828	6.2
1.75	0.07573	1.3653	0.0555	3.9
1.85	0.04243	1.3119	0.0323	2.2
2.03	0.00158	1.3395	0.0012	

TABLE E-29

Photocharacteristics of D-6-3 #6 at 5V for H\*\* Calibration Data

$\lambda$ ( $\mu\text{m}$ )	I ( $\mu\text{A}$ )	H ( $\mu\text{W}$ )	R ( $\mu\text{A}/\mu\text{W}$ )	R' ( $\mu\text{A}/\mu\text{W}$ )	$\eta$ (%)	$\eta'$ (%)
1.04	0.10650	0.0405	2.6296	0.7106	313	96
1.11	0.73350	0.2613	2.8071	0.7586	314	96
1.19	1.76000	0.5630	3.1261	0.8448	326	99
1.28	2.63250	0.8041	3.2738	0.8847	317	97
1.37	3.43400	0.9494	3.6170	0.9747	327	100
1.46	4.24200	1.1463	3.7006	1.0000	314	96
1.55	4.14500	1.2788	3.2413	0.8759	259	79
1.65	3.10900	1.3432	2.3146	0.6255	174	53
1.75	2.14100	1.3653	1.5682	0.4238	111	34
1.85	1.16550	1.3119	0.8884	0.2401	60	18
2.03	0.04450	1.3395	0.3322	0.0898	2	1

TABLE E-30

Photocharacteristics of D-6-3 #6 at 10V for H\*\* Calibration Data

$\lambda$ ( $\mu\text{m}$ )	I ( $\mu\text{A}$ )	H ( $\mu\text{W}$ )	R ( $\mu\text{A}/\mu\text{W}$ )	R' ( $\mu\text{A}/\mu\text{W}$ )	$\eta$ (%)	$\eta'$ (%)
1.04	0.11050	0.0405	2.728	0.7548	325	100
1.11	0.72700	0.2613	2.782	0.7698	311	96
1.19	1.75400	0.5630	3.115	0.8619	325	100
1.28	2.61400	0.8041	3.251	0.8996	315	97
1.37	3.40400	0.9494	3.585	0.9920	325	100
1.46	4.14300	1.1463	3.614	1.0000	307	95
1.55	4.22850	1.2788	3.307	0.9157	265	82
1.65	3.09200	1.3432	2.302	0.6370	173	53
1.75	2.14350	1.3653	1.570	0.4344	111	34
1.85	1.15750	1.3119	0.882	0.2441	59	18
2.03	0.04500	1.3395	0.336	0.0930	2	1

VITA

[PII Redacted]

Irene Marie Nadeau Mills [REDACTED] [REDACTED] [REDACTED]

[REDACTED] She graduated from high school in Somersworth, New Hampshire in 1974 and entered Norwich University, in Northfield, Vermont, from which she received a Bachelor of Science degree in May 1978. Upon graduation, she was commissioned in the USAF through the ROTC program. Upon entering active duty in June 1978 she served as a student at the Air force Institute of Technology, School of Engineering during which time she married Orrin Richard Mills, 2d Lt USA.

[PII Redacted]

Permanent address: [REDACTED]  
[REDACTED]

REPORT DOCUMENTATION PAGE		READ INSTRUCTIONS BEFORE COMPLETING FORM
1. REPORT NUMBER AFIT/GE/EE/79D-25	2. GOVT ACCESSION NO.	3. RECIPIENT'S CATALOG NUMBER
4. TITLE (and Subtitle) Properties of Ion-Implanted and Diffused Photodetectors of Germanium and Germanium-Silicon Alloys		5. TYPE OF REPORT & PERIOD COVERED MS Thesis
		6. PERFORMING ORG. REPORT NUMBER
7. AUTHOR(s) Irene M. Nadeau Mills 2d Lt USAF		8. CONTRACT OR GRANT NUMBER(s)
9. PERFORMING ORGANIZATION NAME AND ADDRESS Air Force Institute of Technology (AFIT/EN) Wright-Patterson AFB, Ohio 45433		10. PROGRAM ELEMENT, PROJECT, TASK AREA & WORK UNIT NUMBERS
11. CONTROLLING OFFICE NAME AND ADDRESS RADC/ESO Hanscom AFB, Massachusetts		12. REPORT DATE Dec 1979
		13. NUMBER OF PAGES 168
14. MONITORING AGENCY NAME & ADDRESS (if different from Controlling Office)		15. SECURITY CLASS. (of this report) UNCLAS
		15a. DECLASSIFICATION/DOWNGRADING SCHEDULE
16. DISTRIBUTION STATEMENT (of this Report)  Approved for public release; distribution unlimited.		
17. DISTRIBUTION STATEMENT (of the abstract entered in Block 20, if different from Report)		
18. SUPPLEMENTARY NOTES  Approved for public release; IAW AFR 190-17  JOSEPH P. HIPPS, Maj, USAF Director of Public Affairs		
19. KEY WORDS (Continue on reverse side if necessary and identify by block number)		
20. ABSTRACT (Continue on reverse side if necessary and identify by block number)  The response of planar shallow-junction Ge photodiodes displayed peak performance at the expected 1.46 $\mu\text{m}$ wavelength. Responsivity and quantum efficiency were measured at $\sim 0.9 \mu\text{A}/\mu\text{W}$ and $\sim 80\%$ , respectively, with leakage currents of $\sim 6 \mu\text{A}$ , typical for Ge photodiodes. Leakage currents were notably decreased in diffused diodes. The high values for responsivity and quantum efficiency could be attributed to the shallow junction ( $\sim 1 \mu\text{m}$ ) designed to increase the amount of photogenerated current which could be		

20 cont.

collected by the p-n junction. The reason for the interest in photodetectors lies in fiber-optic applications. Minimum fiber attenuation and dispersion occurs near  $1.27 \mu\text{m}$ . Photodetectors at this wavelength require tailoring of the bandgap energy of Ge by adding about 10% Si. A quantum mechanical analysis of the energy band structure of the Ge-Si alloy is included with suggestions to obtain energy gap and effective mass values experimentally. Ge-Si photodetectors fabricated as shallow-junction photodiodes should exhibit high photoresponse and quantum efficiency near  $1.27 \mu\text{m}$ .

UNCLASSIFIED

SECURITY CLASSIFICATION OF THIS PAGE(When Data Entered)